Liquid Crystal Phase Transitions of Monodisperse and Bidisperse Suspensions of Rodlike Colloidal Virus

A Dissertation

Presented to

The Faculty of the Graduate School of Arts and Sicences

Brandeis University

Department of Physics

Dr. Seth Fraden, Advisor

In Partial Fulfillment
of the Requirement for the Degree
Doctor of Philosophy

by

Kirstin Rachael Purdy

August 2004

The signed version of this signature page is on file at the Graduate School of Arts and Sciences at Brandeis University.

This dissertation, directed and approved by Kirstin Rachael Purdy's Committee, has been accepted and approved by the Faculty of Brandeis University in partial fulfillment of the requirement for the degree of:

DOCTOR OF PHILOSOPHY

Adam B. Jaffe, Dean of Arts and Sciences

Dissertation Committee:

Dr. Seth Fraden,Chair

Dr. Robert B. Meyer

Dr. Robert Pelcovits, Dept. of Physics, Brown University

Dr. Nolan Flynn, Dept. of Chemistry, Wellesley College

ACKNOWLEDGEMENTS

There are many people I would like to acknowledge, for without them I would not be where I am today. First and foremost is my thesis advisor Prof. Seth Fraden. His direction and knowledge were an invaluable part of this process. I admire his keen ability to direct me along the correct path in under five minutes, and his candor about my strengths and weaknesses.

I would also like to thank my current and former lab-mates. Most notable is Zvonimir Dogic, who first introduced me to the biology of *fd* virus and has since taught me so much as an invaluable collaborator. Ujitha Dassanayake who never let the lab become dull and was a source of much enthusiasm. Emmanuel Belamie and Eric Grelet, who taught me much, and who kindly read my long rambling papers before they are publishable. Slava Berejnov, Joshua Bloustine, Jung uk Shim, Phil Huang, and Chris Young for teaching me about their research projects, helping me with mine, and in general making the lab an enjoyable place to be.

I sincerely thank my thesis committee Prof. Robert Meyer, Prof. Robert Pelcovits, and Prof. Nolan Flynn. I would also like to thank the many collaborators I have had, particularly Dr. Szabolcs Varga, Prof. Amparo Galino, Prof. Simon Mochrie, Prof. Lawrence Lurio, Dr. Adrian Rühm and Prof. Rene van Roij.

I most importantly thank those closest to me. I thank my family for being my personal cheering squad, and I thank Patrick Drew for everything. They have always supported me, even when I myself was frustrated, stressed and in doubt. I hope they will continue to always be there for me.

ABSTRACT

Liquid Crystal Phase Transitions of Monodisperse and Bidisperse Suspensions of Rodlike Colloidal Virus

A dissertation presented to the Faculty of the
Graduate School of Arts and Sciences of Brandeis
University, Waltham, Massachusetts

by Kirstin Rachael Purdy

We experimentally study the role of steric and electrostatic interparticle interactions in monodisperse and bidisperse suspensions of rodlike colloids. For our model system we used aqueous suspensions of the charged semiflexible filamentous bacteriophages *fd* and M13. In solution, these particles undergo entropically driven liquid crystal phase transitions from isotropic to cholesteric (or chiral-nematic) to smectic phases with increasing concentration. For the monodisperse suspensions, we present as a function of ionic strength, measurements of the role of flexibility and surface charge on the transitions between these phases. We also present the evolution of the helical pitch of the cholesteric phase with concentration as a function of solution ionic strength and particle surface charge in order to understand the coupling between ionic strength and surface charge in the expression of chirality in the nematic phase. Unwinding and aligning the chiral-nematic phase in a magnetic field allowed us to measure the nematic ordering of *fd* as a function of rod concentration and solution ionic strength. The nematic orientational distribution function was measured using x-ray diffraction and birefringence techniques. Results were compared with available theoretical predictions for charged flexible rods. Measurements of the phase behavior consistently show unexpected behavior at low ionic strengths, where electrostatic repulsion is poorly screened, and good agreement with theoretical predictions at high ionic strength, where electrostatic interactions are well screened. For the bidisperse suspensions we measured the phase behavior mixtures of *fd* and *fd* coated with poly(ethylene-glycol): two particles of identical length and different diameter. When the diameters differ significantly these mixtures exhibit isotropic-cholesteric, cholesteric-cholesteric and isotropic-cholesteric-cholesteric coexistence. Measured phase diagrams were compared to predictions for binary rod phase behavior.

This thesis is partially based on the following publications:

- K.R. Purdy, Z. Dogic, S. Fraden, A. Rhm, L. Lurio, and S.G.J. Mochrie. Measuring the Nematic order of Colloidal fd Virus by X-ray Diffraction and Optical Birefringence. Physical Review E **67** 031708 (2003). - Chapter 5.

- K.R. Purdy and S. Fraden. The isotropic-cholesteric phase transition of filamentous virus suspensions as a function of rod length and charge. Submitted. - Chapter 2.

- K.R. Purdy and S. Fraden. The influence of charge and flexibility on smectic phase formation in filamentous virus suspensions. In preparation. - Chapter 3.

- K.R. Purdy, S. Varga, A. Galindo, J. Jackson, and S. Fraden. Nematic phase transitions of mixtures of thin and thick colloidal rods. In preparation. - Chapter 6.

- Z. Dogic, K.R. Purdy, E. Grelet, M. Adams, and S. Fraden. Isotropic-nematic phase transition in suspensions of filamentous virus and the neutral polymer Dextran. Physical Review E **69** 031708 (2004).

Contents

List of Tables

List of Figures

Chapter 1

Introduction

1.1 Overview

In this thesis we experimentally study the role of steric and electrostatic interparticle interactions in phase transitions of monodisperse and bidisperse suspensions of rodlike colloids. Knowing the interactions between particles allows us to predict the phase behavior of these particles. The most simple interaction between two particles is a hard-core interaction, where the particles only feel each other when they are in contact with one another. In a hard particle fluid the energy E of the system is proportional to Nk_BT, and thus the free energy, $F = E - TS$, is proportional to the entropy S by $F = T(Nk_B - S)$. The equilibrium phase behavior of the hard particle system is athermal, or independent of the temperature T, because it depends only on the maximization of the entropy, as both S and Nk_B are independent of temperature.

Historically, the first step towards understanding the ordering of hard particles was taken in 1949 when Onsager wrote his seminal paper on the phase behavior of hard rods [1]. He showed that hard-core repulsion between highly anisotropic particles is sufficient to produce a stable nematic phase. A nematic phase is defined as a system of rodlike particles which have a long range orientational order and short range positional order (Fig. 1.1). Charged particles will similarly produce a nematic phase as the interparticle interactions are strictly repulsive [1]. Later, it was shown through theory and computer simulations that hard rods could also exist in a stable smectic phase [2, 3]. A smectic phase is defined as having quasi-long range one dimensional periodic order in the direction of the alignment of the particles and short-ranged liquid like order in the other two dimensions. Parallel to the development of hard-rod phase behavior was the equally important development of theory and simulations which showed that hard spheres can also undergo a disorder-order transition from a liquid to a crystal [4, 5]. It is now well accepted that repulsive interactions are sufficient to form nematic and smectic phases in anisotropic systems and a crystal phase in spherical systems.

Furthermore, the hard-rod theory developed by Onsager can be extended for studies of multi-component hard-particle suspensions. The most simple version of a multi-component system is a binary system. For a binary mixture of hard rods, hard-core repulsion has been shown to produce an isotropic to nematic transition in both theory and simulation [6, 7, 8, 9], as in the monodisperse case, but also, if the particles are dissimilar enough, isotropic-isotropic or nematic-nematic phase separation where the two different particles partition themselves into the coexisting phases different compositions [10]. As in the monodisperse case, the phase transitions are driven entirely by the hard-core repulsion between like and unlike rods. In this thesis we limit our experiments to measurements of monodisperse and bidisperse mixtures of purely repulsive rods using a colloidal rod system. Onsager's hard-rod theory, however is not limited to only monodisperse and bidisperse rod systems, as it has also been used in the prediction of the phase behavior of tridisperse [11] and polydisperse suspensions [12].

Spherical and anisotropic colloids are the only known experimental systems to exhibit the phase behavior predicted for hard-particle systems and thus they have

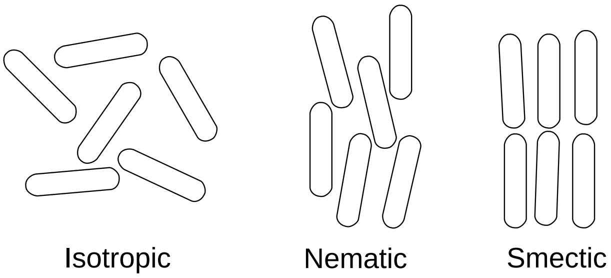

Figure 1.1: Isotropic, nematic and smectic phases schematically drawn for hard spherocylinders. With increasing concentration a suspension of hard spherocylinders will undergo a phase transition from higher to lower symmetry to maximize the entropy of the system.

become very useful in experimentally studying hard-particle thermodynamics [13, 14]. Using colloids to study the liquid to crystal transition of hard spheres is very economical and simple as techniques have been developed for chemically synthesizing highly monodisperse polymeric spheres which have interactions which approximate a hard-sphere potential. However, creating monodisperse suspensions of anisotropic particles is much more difficult chemically and is a topic of continuing investigation. Fortunately, the rod-like viruses including *fd*, M13, Pf1 and TMV are created biologically to be highly monodisperse and thus are ideal particles for studying anisotropic hard-particle phase behavior. In this thesis we specifically use suspensions of the viruses *fd* and M13 which have been shown to exhibit liquid crystal behavior which agrees with model hard-rod predictions at low concentrations. These particles are unique in that the very nature of their structure lends itself to relatively simple chemical and genetic modification allowing for the creation of a wide variety modified viral particles which also behave as model hard-rods. Modifying the particle structure can change its physical properties (length, diameter, flexibility) as well as its interaction potential (electrostatic, steric hard-core). In this thesis we use these modified colloidal rods to experimentally measure how changes in repulsive interactions and/or particle shape change the liquid crystal phase transitions of monodisperse and bidisperse suspensions from that predicted for hard-rods.

In the following sections we describe the basic theoretical and experimental foundations of this thesis. In section 1.2 we introduce Onsager's theory for the isotropic-nematic phase transition of hard-rods and present extensions of this theory with include the effects of charge and flexibility. We also introduce a scaled particle theory for rods which are not well described by Onsager's theory. Throughout this thesis we will use these theories for comparison with experiments. In section 1.3 we introduce in more detail our experimental system of filamentous bacteriophages, *fd* and M13. We show that these viruses are a highly versatile model system which forms liquid crystal phases often well described by Onsager's theory, and which can easily be manipulated by genetic or chemical means to vary significant variables which effect phase behavior. Section 1.4 is dedicated to an outline of this thesis.

1.2 Theoretical background

1.2.1 Onsager's theory for an entropy driven phase transition in a system of hard rods

To describe the phase behavior of hard spherocylinders Onsager developed a theory based on the second virial expansion of the free energy [1]. The free energy of hard rods in a solvent expanded to the second virial coefficient is:

$$\frac{\Delta F}{Nk_BT} = \frac{\mu^0}{k_BT} - 1 + \log c + \sigma - c\frac{1}{2}\int\int \beta f(\mathbf{\Omega})f(\mathbf{\Omega}')d\mathbf{\Omega}'d\mathbf{\Omega} \tag{1.1}$$

where μ^0 is the chemical potential of the solvent, k_B is the Boltzmann constant, T is the temperature, and c is the rod concentration N/V. The single rod orientational distribution function $f(\mathbf{\Omega})$, is normalized by integrating over the solid angle $\mathbf{\Omega}$,

$$\int f(\mathbf{\Omega})d\mathbf{\Omega} = 1 \tag{1.2}$$

The orientational entropy term σ is equal to:

$$\int f(\mathbf{\Omega}) \log(4\pi f(\mathbf{\Omega}) d\mathbf{\Omega} \tag{1.3}$$

The second integral contains the excluded volume interactions, with $\beta = \frac{1}{V} \int \int \Phi_{12} d\mathbf{r_1} d\mathbf{r_2}$ equal to the integral over of the Mayer-Mayer function, Φ_{12}, which is equal to -1 if two particles intersect and zero otherwise. The Mayer-Mayer function is related to the hard-particle interaction potential w by

$$e^{-w/k_B T} = 1 + \sum_{i<j} \Phi_{ij} + \sum \Phi_{ij} \Phi_{i'j'} + ... \tag{1.4}$$

Note that by limiting the free energy expansion to the second virial coefficient we include only two-body interactions and curtail this expression to the first two terms; this severely limits the accuracy of this approximation at high particle concentrations where three or more particle interactions are common. For long thin rods of length L and diameter D, β simplifies to

$$\beta = -2L^2 D |\sin \gamma| \tag{1.5}$$

where $\gamma(\mathbf{\Omega}, \mathbf{\Omega'})$ is the angle between adjacent rods. In the isotropic phase, $<< \ \sin(\gamma) >>= \pi/4$ and b is the second virial coefficient in the isotropic phase $B_2^i = b = L^2 D\pi/4$.

If we define

$$\rho = \frac{4}{\pi} \int \int |\sin(\gamma)| f(\mathbf{\Omega}) f(\mathbf{\Omega'}) d\mathbf{\Omega'} d\mathbf{\Omega} \tag{1.6}$$

then the free energy can be written simply as

$$\frac{\Delta F}{N k_B T} = \text{constant} + \log(c) + \sigma(f) + bc\rho \tag{1.7}$$

To find the isotropic-nematic phase boundaries, the free energy is first minimized with respect the orientational distribution function as a function of concentration. The equilibrium concentrations for the coexisting isotropic and nematic phases can then be found by setting the osmotic pressure (Π) and chemical potential (μ) of the isotropic phase ($f(\theta) = 1/4\pi$) equal to the osmotic pressure and chemical potential of the nematic phase, respectively. The osmotic pressure and chemical potential are defined as

$$\begin{aligned} \Pi &= \phi^2 \frac{\partial F(\phi)}{\partial \phi} \\ \mu &= F(\phi) + \phi \frac{\partial F(\phi)}{\partial \phi} \end{aligned} \tag{1.8}$$

where ϕ is the volume fraction of spherocylinders. The equations for equal osmotic pressure and chemical potential are

$$\begin{aligned} (c_i + c_i^2) &= (c_n + c_n^2 \rho_n) \\ \log(c_i) + 2c_i &= \log(c_n) + 2c_n\rho_n + \sigma_n \end{aligned} \tag{1.9}$$

To solve for the equilibrium coexistence concentrations for hard and charged rigid rods, Onsager used a trial orientational distribution function of

$$f(\theta) = \frac{\alpha}{4\pi \sinh \alpha} \cosh \alpha \cos \theta \tag{1.10}$$

where θ is the angle between the nematic director and a test rod and α is the minimization parameter. Because the rods are cylindrically symmetric, the orientational distribution function is independent of azimuthal rotations. Using the Onsager trial function, ρ simplifies to

$$\rho(\alpha) = \frac{2I_2(2\alpha)}{\sinh^2(\alpha)} \tag{1.11}$$

where I_2 is a modified Bessel function, and $\sigma(\alpha)$ simplifies to

$$\sigma(\alpha) = \log(\alpha \coth(\alpha)) - 1 + (\sinh \alpha)^{-1} \tan(\sinh \alpha)^{-1} \tag{1.12}$$

The isotropic and nematic coexistence concentrations can be determined using Eq. 1.8. The resulting values are [1]

$$bc_i = 3.340 \quad \text{and} \quad bc_n = 4.486. \tag{1.13}$$

Numerical calculations have also been done to solve for the exact form of the orientational distribution function [7, 15]. Using the exact form of the orientational distribution, function the coexistence concentrations obtained were:

$$bc_i = 3.289 \quad \text{and} \quad bc_n = 4.191 \tag{1.14}$$

as determined by Herzfeld, Lekkerkerker and Chen [15, 7].

The nematic order parameter can also be calculated once the orientational distribution function is known:

$$S = 2\pi \int_0^{\pi} \left(\frac{3}{2} \cos(\theta) - \frac{1}{2} \right) f(\theta) \sin(\theta) d\theta \tag{1.15}$$

Similarly, the nematic order parameter as calculated using Onsager's trial orientational distribution function is $S = 0.847$, whereas the coexisting nematic order parameter calculated numerically from the exact orientational distribution function is $S =$0.7922 [15, 7]. We observe that the coexistence concentrations and order parameter determined numerically differ from those predicted using Onsager's trial function.

1.2.2 Effect of charge in a hard rod system

If the hard rods described previously are now charged, an additional electrostatic interaction energy can be incorporated into Onsager's theory. The electrostatic interaction between two rods is approximately [1, 16]:

$$\frac{w_{el}(x)}{kT} = \frac{Ae^{-\kappa(x-D)}}{\sin(\gamma)} \tag{1.16}$$

where x is the closest distance of approach between two charged rods, γ is the angle between adjacent rods, A is the proportionality constant obtained from solving the Poisson-Boltzmann equation, and κ^{-1} is the Debye screening length. This additional interaction changes the second virial coefficient:

$$\beta(\gamma) = -2L^2 \sin(\gamma)(D + \int_0^\infty (e^{-\frac{w_{el}(x)}{kT}} - 1)dx) \tag{1.17}$$

This integral equation adds a term to the diameter of the hard-rod creating an effective diameter:

$$D_{\text{eff}} = D(1 + \frac{1}{\kappa D}(\ln A' + C_E - \log(\sin(\gamma))) \tag{1.18}$$

where $C_E = 0.577215665$ is Euler's constant, and $A' = Ae^{-\kappa D}$ as described in [16]. In the isotropic phase D_{eff} simplifies to

$$D_{\text{eff}} = D(1 + (\log A' + C_E + \log 2 - 1/2)/\kappa D). \tag{1.19}$$

The phase behavior of charged rods in the Onsager limit can thus be described by Onsager's theory for hard rods with an effective diameter larger than their bare diameter. The D_{eff} for the isotropic phase of *fd* virus rods is shown in Fig. 1.2 for three experimentally obtainable surface charges. The value for A' is determined by

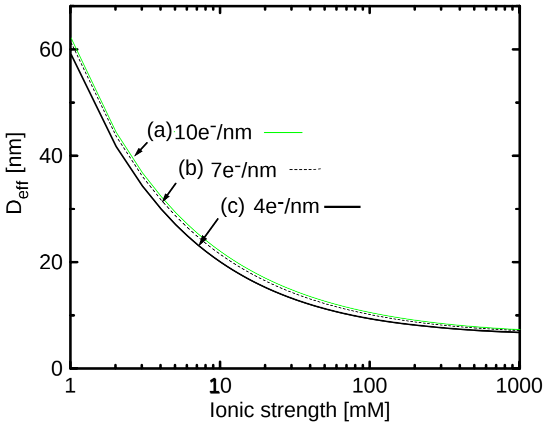

Figure 1.2: Effective diameter as a function of ionic strength and surface charge. With increasing ionic strength D_{eff} approaches the bare diameter of *fd* (M13) $D = 6.6$ nm. The effective diameter is plotted for surface charges of (a) 10 e^-/nm, (b) 7 e^-/nm and (c)4 e^-/nm. These surface charge densities are equal to the surface charge of *fd* at pH 8.2, *fd* at pH 5.2 and M13 at pH 8.2, and M13 at pH 5.2, respectively. At these surface charge densities D_{eff} is insensitive to variation in charge.

numerically solving the Poisson-Boltzmann equation using the routine developed by Philip and Wooding [17]. Due to the nonlinearity of the Poisson-Boltzmann equation, changing the surface charge has only a minimal effect on the effective diameter. Fig. 1.2 shows that increasing ionic strength decreases the effective diameter.

In a nematic phase the electrostatic repulsion will depend on the angle between two interacting rods. Charged particles will tend to misalign as they have a lower energy when perpendicular to each other than when they are parallel. This effect is known as twist, and is characterized by the parameter $h = \kappa^{-1}/D_{\text{eff}}$, where κ^{-1} is the Debye screening length. Twist is manifested by an increase in the effective diameter in the nematic phase. For charged polymers, twist acts to destabilize the nematic phase. For highly charged polymers (similar to the bacteriophage used in our experiments) h is small, and has little effect on D_{eff} [14]. The specific effect of electrostatic interactions on the isotropic and nematic phases of suspensions of M13 and *fd* bacteriophage is the subject of much investigation in Chapters 2 and 3.

1.2.3 Flexible hard rods in Onsager's theory

The persistence length (P) of a polymer describes the length over which two tangent vectors along that polymer are correlated. It is also equal to one half the Kuhn length of the polymer [18]. The ratio which describes the flexibility of a polymer is the ratio of the polymer contour length to its persistence length, or L/P. If $L << P$, the polymer is considered rigid, whereas if this ratio is large, $L >> P$, the polymer is flexible. The term in the free energy which accounts for the rotational entropy of the rods and the entropy associated with the loss of configurations due to confinement of the bending modes of the semi-flexible rods in the nematic phase is Eq.1.21. The effect of flexibility on the isotropic-nematic phase transition was theoretically investigated by Khoklov and Semenov [19]. Semiflexibility modifies σ by:

$$\sigma(f) = \frac{L}{2P}\frac{1}{4\pi}\int \frac{(\nabla f)^2}{4f} d\Omega \tag{1.20}$$

In the limit of very flexible $L/P >> 1$ and very rigid $L/P << 1$ rods the equilibrium properties of the I-N phase transition have been calculated explicitly using Eq. 1.20 [19]. For Onsager's distribution function, σ has been derived in the semiflexible limit $L \sim P$ by extrapolating between the hard rod and the flexible chain limits [20, 21, 22]. The expression for σ obtained by Hentschke is given by

$$\sigma(\alpha, \frac{L}{P}) = \ln(\alpha) - 1 + \pi e^{-\alpha} + \frac{L}{6P}(\alpha - 1) + \frac{5}{12}\ln\left(\cosh\left(\frac{L}{P}\frac{\alpha - 1}{5}\right)\right) \tag{1.21}$$

To determine the effects of flexibility in the limit where $P \sim L$ Chen numerically minimized the free energy using σ as defined in Eq. 1.20, and subsequently calculated the properties of the isotropic-nematic phase transition. Flexibility acts to increase the packing entropy needed to enter the nematic phase, which is shown by an increase in the concentration of rods needed to cross the phase boundary from the isotropic to the nematic phase. Increased flexibility also lowers the nematic order parameter and narrows the isotropic-nematic coexistence region. In Fig. 1.3 we show the evolution of the predicted coexistence concentrations and nematic order parameter with increasing flexibility as determined by Chen [23].

1.2.4 A scaled particle theory for hard rods

In this thesis we experimentally measure the phase transitions of colloidal rodlike particles. Previous measurements have shown that the experimental phase behavior of bacteriophage suspensions is qualitatively described by Onsager's theory for charged-semi-flexible rods, however, for more quantitative comparison to theoretical predictions it is often necessary to go beyond Onsager's second virial expansion. Specifically, because the free energy is truncated at the second term in the virial expansions it is not appropriate for describing the behavior of suspensions where third and higher virial coefficients, which describe multiple particle interactions, become significant. By expanding the free energy to include second and third virial coefficients it has been shown that Onsager's theory is exact for the isotropic-nematic transition of rods with $L/D > 100$ [26]. However, when studying phase behavior above the isotropic-nematic phase transition, or in the limit where the aspect ratio of the particles is small ($L/D < 100$) we often turn to a scaled particle theory, which incorporates all virial coefficients of the free energy in an approximate way.

The scaled particle theory for hard spherocylinders was originally developed by Cotter [27]. Scaled particle theory has the desired features of equaling Onsager's theory in the $L/D \rightarrow \infty$ limit, and equaling the scaled particle hard sphere theory in the $L \rightarrow 0$ limit. Additionally, the coexistence concentrations for the I-N transition predicted by the scaled particle theory are in very close agreement with the results from computer simulations for rods of various aspect ratio [24, 25], even for $L/D < 100$

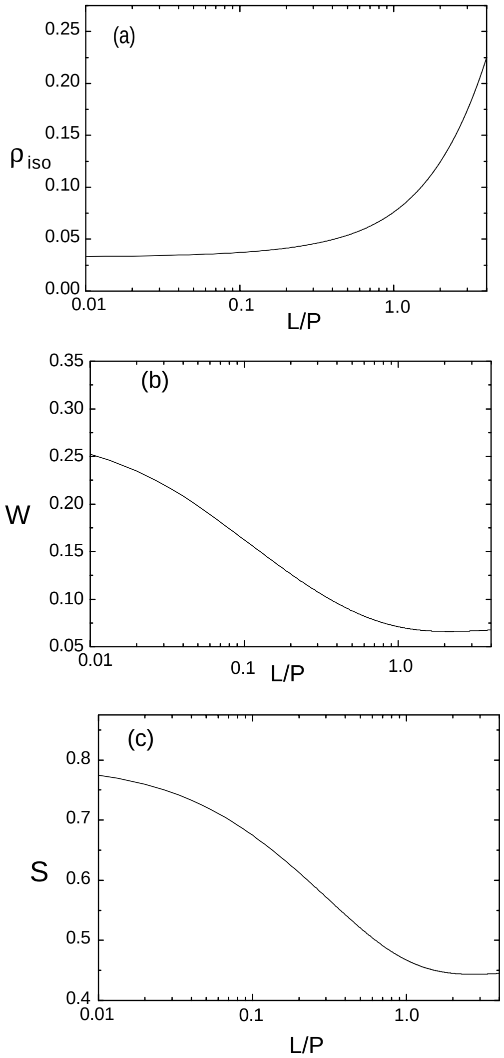

Figure 1.3: Isotropic concentration ($\rho_{iso} = (4/\pi)L^2D(N/V)$), number density difference between isotropic and nematic phase ($W = C_n/C_i - 1$) and order parameter (S) of the nematic phase co-existing with isotropic phase as a function of the flexibility of the particle L/P as calculated by Chen [23]. The theoretical curves are the exact numerical results within the second virial approximation.

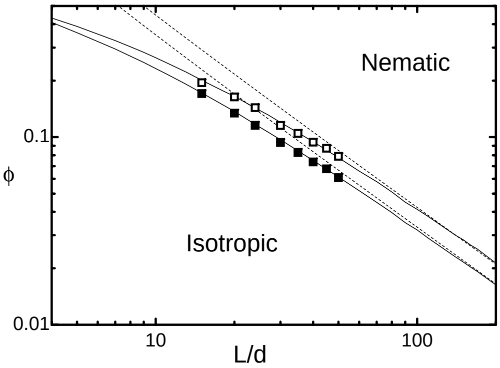

Figure 1.4: The isotropic-nematic phase transition for hard spherocylinders as predicted by Onsager's theory (dotted line) and scaled particle theory (solid line) [24]. Squares are simulation results of Bolhuis and Frenkel [25]. Open squares are the coexisting nematic phase and solid squares are the coexisting isotropic phase. The volume fraction presented is for spherocylinders $\phi = (N/V)(\pi LD^2/4 + \pi D^3/6)$, where N/V is the number density of particles , but the true aspect ratio of the spherocylinder is $(L + D)/D$.

where Onsager's theory no longer accurately predicts the simulation results. These results are presented in Fig. 1.4. This comparison has been previously published [24]. This agreement between scaled particle theory and simulations indicates that the scaled particles theory provides a good approximation for third and higher virial coefficients. Here we present the calculation of the isotropic-nematic phase diagram using scaled particle theory [27, 28]. The expression for the free energy of a pure hard spherocylinder colloidal suspension is given by:

$$\begin{aligned}\frac{F(\delta,\phi,\alpha)}{Nk_bT} = \quad & \ln(\phi) - \ln(1-\phi) + \sigma(\alpha, L/P) + \Pi_2(\delta,\alpha)\frac{\phi}{1-\phi} \\ & + \frac{1}{2}\Pi_3(\delta,\alpha)\left(\frac{\phi}{1-\phi}\right)^2 \end{aligned} \tag{1.22}$$

where ϕ is the volume fraction of spherocylinders

$$\phi = \frac{N_{\mathrm{rods}}}{V}\left(\frac{\pi}{6}D^3 + \frac{\pi}{4}D^2 L\right). \tag{1.23}$$

The coefficients Π_2 and Π_3 are given by the following expressions

$$\Pi_2(\delta, \alpha) = 3 + \frac{3(\delta - 1)^2}{(3\delta - 1)}\xi(\alpha), \tag{1.24}$$

$$\Pi_3(\delta, \alpha) = \frac{12\delta(2\delta - 1)}{(3\delta - 1)^2} + \frac{12\delta(\delta - 1)^2}{(3\delta - 1)^2}\xi(\alpha) \tag{1.25}$$

and the parameter δ is the overall length to diameter ratio of the spherocylinder $\delta = \frac{L+D}{D}$. The function $\sigma(\alpha, L/P)$ is an expression that accounts for the rotational entropy of the rods and the entropy associated with the loss of configurations due to confinement of the bending modes of the semiflexible rods in the nematic phase has been derived by extrapolating between the hard rod and the flexible chain limits [20, 21, 22]. In this paper the expression for σ obtained by Hentschke is used for numerical calculations and is given by

$$\sigma(\alpha, \frac{L}{P}) = \ln(\alpha) - 1 + \pi e^{-\alpha} + \frac{L}{6P}(\alpha - 1) + \frac{5}{12}\ln\left(\cosh\left(\frac{L}{P}\frac{\alpha - 1}{5}\right)\right) \tag{1.26}$$

The function $\xi(\alpha)$ that describes the interactions between rods at the level of the second virial coefficient is given by:

$$\xi(\alpha) \;\; = \;\; \frac{2I_2(2\alpha)}{\sinh^2(\alpha)} \tag{1.27}$$

For this calculation we assume the Onsager ansatz for the orientational distribution function given by :

$$f(\alpha, \cos(\theta)) = \frac{\alpha \cosh(\alpha\cos(\theta))}{4\pi \sinh(\alpha)}. \tag{1.28}$$

After the expression for the scaled particle free energy (Eq. 1.22) is obtained, we minimize the scaled particle free energy with respect to the parameter α to find the order parameter, S, of the nematic phase at that rod concentrations. Use of the Onsager approximation for the orientational distribution function is appropriate as we will show in Chapter 5 that it accurately describes the measured distribution of rod orientations.

To find the concentrations of rods in the coexisting isotropic and nematic phases we solve the conditions for the equality of the osmotic pressure and chemical potential as in Eq. 1.8. In Fig. 1.5 we present the phase behavior predicted by scaled particle theory for hard rods as a function of rod flexibility. The scaled particle results are shown for $L/D = 100$ and $L/D = 20$. For comparison we include the results computed at the second virial limit [23]. First we observe that the scaled particle theory for long rods agrees very well with Onsager's prediction for the isotropic coexistence concentration. However, the nematic order parameter and the coexistence width predicted by scaled particle theory both differ significantly from the second virial prediction. This is partially due to the use of Onsager's orientational distribution function in the scaled particle theory. It has been shown previously that using different distribution functions can have a significant effect on the properties of the coexisting nematic phase [29]. The increased sensitivity of the nematic order parameter to the form of the orientational distribution function as compared to the coexistence concentrations indicates that measuring the nematic order parameter is a much more sensitive test of the accuracy of Onsager's theory. This is discussed in detail in Chapter 5. Second, we observe that there is a significant change in the predicted coexistence concentrations with decreasing particle length in the scaled particle theory. The change in phase transition properties with decreasing L/D indicates an increasing influence of higher virial coefficients on the isotropic-nematic phase transition.

To take into account the fact the experimental rods are charged, instead of using the hard core diameter D in our calculations we use the effective diameter D_{eff}

[30]. Strictly speaking this re-scaling procedure by D_{eff} is valid only for densities at which the system is described by the second virial approximation, therefore our theoretical prediction has an uncontrolled approximation. Despite this fact the agreement between the theory and the experiments is quite satisfactory, particularly in the limit of high ionic strength, as we will show in the following chapters. We note that there has been recent effort to extend the validity of the scaled particle theory to include electrostatic interactions, but this theory was not included in our calculations [31, 32].

1.3 The versatility of *fd* and M13 virus as a colloidal particle

Throughout this thesis we study the liquid crystal phase transitions of suspensions of the charged and semiflexible bacteriophages *fd* and M13. Both M13 and *fd* are charged semiflexible rodlike virus with a contour length L of 0.88 μm, diameter D of 6.6 nm and persistence length P of 2.2 μm[14]. The ratio of the persistence length to contour length $P/L = 2.5$ indicates that these rods should behave as semi-flexible particles. The molecular weight of the phages is 1.64 $\times 10^7$ g/mol. Above pH 4, these particles are negatively charged and interact via a combination of electrostatic repulsion and hard-core interactions.

The viral rods are composed of a single stranded DNA about which 2700 copies of its major coat protein are helicoidally wrapped. This virus structure is illustrated in Fig. 1.6. The composition of the major coat protein (p8) on M13 differs from that of *fd* by only one amino acid; the negatively charged aspartate (asp$_{12}$) in *fd* is substituted for the neutral asparagine (asn$_{12}$) in M13 [33]. This has a minimal effect on the virus structure, as determined by x-ray diffraction, but indeed has a significant effect on surface charge. The *fd* virus p8 protein has 5 negatively ionizable amino

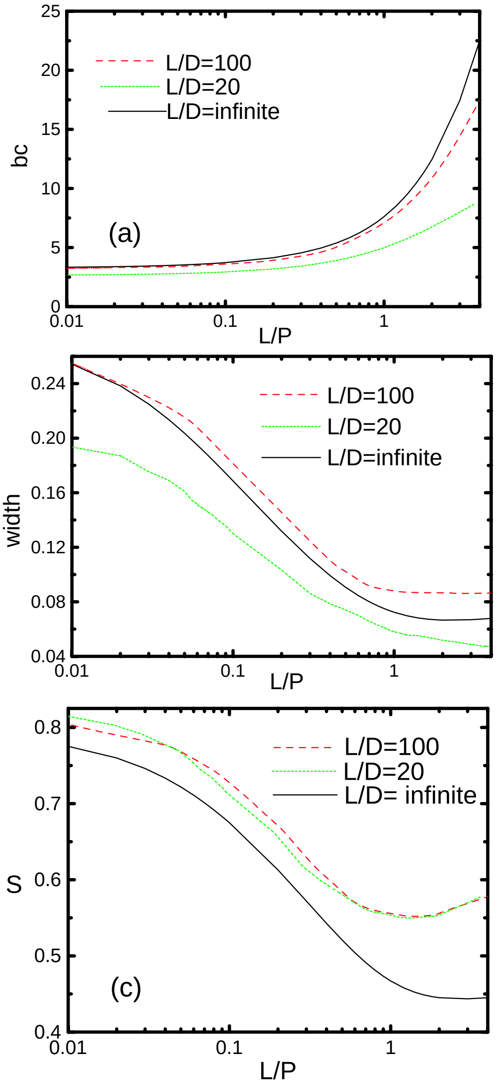

Figure 1.5: Isotropic concentration ($bc = (4/\pi)L^2D(N/V)$), number density difference between isotropic and nematic phase ($W = C_n/C_i - 1$) and order parameter (S) of the nematic phase co-existing with isotropic phase as a function of the flexibility of the particle L/P. Solid lines are calculated from Onsager's theory [23], dashed and dotted lines are the scaled particle theory results for $L/D = 100$ and $L/D = 20$, respectively.

acids and one positively ionizable amino acid which are exposed to the virus surface. These amino acids and the terminal amine, which contributes approximately 1/2 e^+ at neutral pH are responsible for determining the net viral surface charge, approximately 3.5e^-/protein subunit at pH 7.2 [34]. M13 p8 proteins are identical accept for the aforementioned switch in the 12$^{\text{th}}$ amino acid, which results in a net charge per p8 of about 2.5e^- at neutral pH. This results in a total charge difference between fd and M13 of approximately 30%. The net surface charge of both virus particles can then be increased or decreased by increasing or decreasing the solution pH, respectively. In Fig. 1.7 we present a schematic diagram of the charge configuration along the length of the virus. The effect of this surface charge difference in the interparticle interactions, and thus phase behavior is a topic which is studied in Chapters 2-4.

In solution *fd* and M13 have been shown to exhibit isotropic, cholesteric and smectic phases with increasing concentration [30, 35]. An isotropic phase is a dilute solution of rods in which the rods are randomly oriented. Between crossed polarizers this phase appears dark. A cholesteric phase is a nematic phase which has a helical superstructure. In a cholesteric phase the rods orient locally about a nematic director which twists 360^o over a finite length. This length is referred to as the cholesteric pitch. Experimentally the cholesteric phase is characterized by its birefringence pattern observed between crossed polarizers. As the local alignment of the rods twists, the length of the cholesteric pitch spans two bright and two dark lines between polarizers. These are regions where the rods are parallel, or perpendicular to the plane of observation, respectively.

The smectic phase is also birefringent, but is most easily characterized by its strong Bragg scattering of visible light from the periodic layering of the rods. The smectic layers spacing is about 1% larger than the length of the rods within the layers. For rods with a length of about 1μm, the scattered light is in the visible range $\lambda \sim L$.

In Fig. 1.8 we present the phase diagram of *fd* virus suspensions as a function

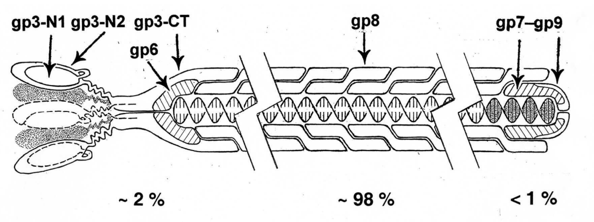

Figure 1.6: Schematic of the structure of M13 (*fd*) virus. Each of the coat proteins which encase the single stranded viral DNA are labeled. There are a few copies, approximately five, of each of the minor coat proteins (p3, p6, p7, p9), and 2700 copies of the major coat protein (p8).

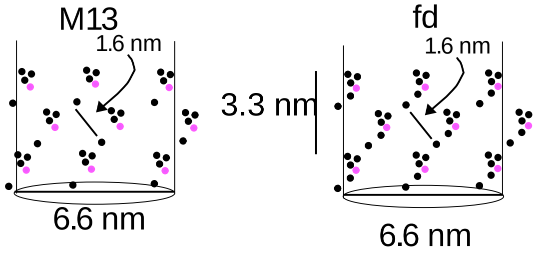

Figure 1.7: Schematic diagram of the surface charge configuration of M13 and *fd* virus. Coat-protein repeat is 5 fold about the viral axis with 3 visible in this 2D representation. Two more coat proteins in each row are not shown and are on the opposite face of the cylinder. The circumferential separation between coat proteins at the same height is $\pi D/5 = 4.2$ nm. Black represents acidic amino acids (negative at high pH), and pink (grey) represents basic (positive at high pH) amino acids. Known distances are labeled [33].

of ionic strength. The details of the isotropic-cholesteric and cholesteric-nematic transitions for *fd* and M13 are discussed in detail in the following chapters. We do plot the theoretically predicted isotropic coexisting concentrations, as determined by Chen for semiflexible rods [23] with an electrostatic effective diameter D_{eff} to show that *fd* suspensions indeed are well described by Onsager's theory for charged semiflexible rods, particularly at high ionic strength where L/D_{eff} is large and the second virial approximation is valid.

To produce these virus, a strain of *E. Coli*, JM101, is grown and infected with either M13 or *fd*. The protocol for the growth and purification of the virus is described extensively in the Appendix and in [36]. For one liter of bacterial growth media (LB

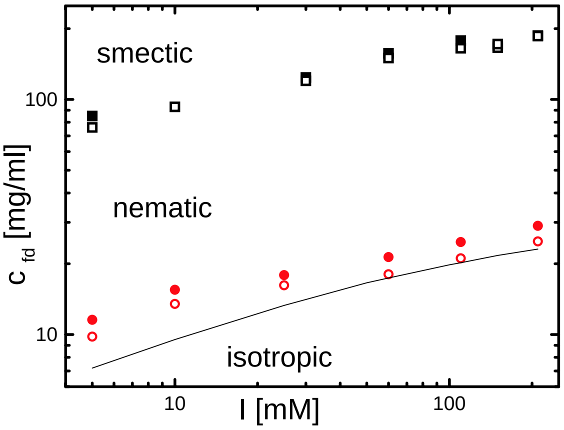

Figure 1.8: Phase transitions for suspensions of *fd* as a function of ionic strength. The isotropic-cholesteric transition is indicated by the circles, with the open circles the coexisting isotropic phase. The cholesteric- smectic transition is indicated by the squares with the open symbols the highest measurable nematic phase concentration. The phase behavior was measured at pH 8.15 in 20 mM Tris buffer with NaCl added to change the ionic strength. The solid line is the second virial theoretical prediction for coexisting isotropic phase for charged semiflexible rods with $L/P = 0.4$ [23].

media) we obtain between 10 and 50 mg of purified virus. We can alter the contour length of the *fd* particles by changing the length of the DNA packaged within the viral coat proteins. Experiments indicate that the viral length is proportional to the length of the encapsulated DNA. Using the phagemid method, well documented in molecular biology, a plasmid DNA sequence which contains the M13 origin of replication, but not necessarily all of the DNA needed to encode viral proteins, is grown in a slowly reproducing *E. Coli* bacteria, Xl1-Blue. The origin of replication contains a DNA sequence which begins the replication of viral DNA. An M13 helper phage, M13K07, which has a damaged packaging gene, but a complete protein encoding sequence, is then allowed to infect the bacteria. The viral proteins are translated from the helper phage by the bacteria, but the plasmid DNA sequence is preferentially packaged into the proteins as the helper phage DNA is damaged at the site where the viral proteins are bound (packaging gene), but the plasmid DNA is not. The resulting suspension is predominantly protein coated plasmid DNA, or phagemid, with a small percentage of helper phage. The protocol for this procedure is described in detail in the Appendix. We have grown virus and phagemid with a range of lengths (1.2 μm, 0.88 μm, 0.66 μm, and 0.4 μm).

In addition to modifying the virus particles biologically, they can also be modified chemically after growth is completed. The diameter of the virus rods can be altered by coating the surface with irreversibly bound polymers. The terminal amine of each of the coat proteins are ideal reaction sites for chemical modification of the virus particles. The type of polymer used to coat the virus depends on the specific properties required. If the neutral polymer poly(ethylene glycol) (PEG) is used to coat the surface of the virus and the molecular weight is large enough (5,000 -20,000 g/mol) the polymer coating acts to sterically stabilize the rods, allowing them to interact in a charge independent matter [37, 38].

Specific genetically modified M13 virus, which are typically used in phage-display technology, are available commercially with a modified p3 protein. Phage display libraries are available in which a random library of unique peptides 7-12 amino acids in length are incorporated into the p3 protein. One of the unique peptide sequences can be selected by binding it to the target of choice (typically an antigen) and then amplifying the phage. By selecting peptide sequences containing unique chemistry (for example the sulfur containing cysteine), functionalized polymers (PEG, DNA, etc) can also be bound to this site allowing for the creation of asymmetric colloidal particles.

The unmodified colloidal virus rods are an ideal experimental system for studying hard-rod phase behavior as their high degree of monodispersity makes them the only particles known to accurately follow the predicted phase progression for hard-rods (isotropic, nematic, smectic)[14, 25]. The isotropic-nematic phase behavior of *fd* quantitatively agrees with Onsager's theory for charged, semi-flexible rods[30]. The ability to synthesize a wide range of colloidal particle sizes and shapes allows for thorough exploration of the entropy driven phase behavior of a wide range of particle shapes and interparticle interaction potentials (sterically stabilized or electrostatically repulsive). By modifying the length, diameter and surface charge of these rods we have the ability to study the fundamental theories of liquid crystal ordering and demixing in monodisperse and bidisperse mixtures.

1.4 An outline of this thesis

The goal of this thesis is to enhance the understanding of the relationship between interparticle interactions and the properties of bulk colloidal liquid crystal phases through experimental measurement of the liquid crystal phase transitions of suspensions of the rodlike M13 and *fd* viruses. Before this thesis the basic phase behavior of suspensions of *fd* virus was known. The *fd* suspensions were known to exhibit isotropic-cholesteric and cholesteric-smectic phase behavior which qualitatively agreed with theoretical predictions for charged-flexible rods. In this thesis we expand the study of the phase behavior of virus suspensions to further measure the equilibrium phase behavior of monodisperse and bidisperse suspensions of colloidal rodlike particles. Due to the complex interactions between the colloidal particles we find that certain aspects of the liquid crystal phase behavior are very sensitive to subtle changes in interaction parameters (surface charge, particle length, etc.), while others remain insensitive.

Chapters 2 and 3 describe how surface charge and flexibility influence the isotropic-cholesteric (Chapter 2) and cholesteric-smectic (Chapter 3) phase transitions. By varying the contour length of the bacteriophages while maintaining local structure the competition between flexibility and rigidity within the semiflexible limit is measured and theoretical predictions are tested. Furthermore by varying the surface charge of the virus particles (either M13 or *fd*) the efficacy of current approximations of electrostatic interactions for use in comparison of our charged-rod results with hard-rod theories is tested. Both M13 and *fd* form a cholesteric phase in suspension, however the free energy difference between the cholesteric phase and the nematic phase is small [39], thus Onsager's theory will describe the isotropic-cholesteric (I-Ch) transition as well as the isotropic-nematic (I-N) transition. Although we study the I-Ch transition in this thesis, we expect our results to apply to the I-N transition as well and thus we will use I-Ch and I-N interchangeably.

Chapter 4 continues the investigation of the effect of surface charge, now on the cholesteric phase. The evolution of the pitch with concentration depends strongly on the interparticle electrostatic interactions which depend on both surface charge and solution characteristics (pH and ionic strength). Changing the pH alters the number of ionizable amino acids on the surface of the virus particles and thus changes their bare charge in solution. Additionally, the coupling between the helicity of the enclosed viral DNA and the macroscopic chiral structure (the cholesteric pitch) is investigated by adding silver ions to the virus suspension. These ions intercalate between the DNA base pairs altering the structure of the viral DNA and subsequently the cholesteric pitch, suggesting a correlation between viral DNA/protein interactions and the macroscopic expression of chirality.

In Chapter 5 the functional form of the angular distribution of the nematic phase is determined as a function of *fd* concentration. Measuring the angular distribution function is the most direct test of the accuracy of Onsager's free energy. Typically *fd* virus forms a cholesteric phase, but when placed in a magnetic field the cholesteric pitch unwinds and the virus suspension forms a mono-domain nematic phase. The orientational distribution of the rods was imaged in Fourier space via small angle x-ray diffraction. These images were then deconvolved using computer analysis to extract the real space orientational distribution of the particles. The nematic ordering was also measured from the birefringence of the nematic samples allowing for an accurate measurement of the intrinsic birefringence of the *fd* rods.

Chapter 6 returns to the study of the isotropic-nematic phase transition but this time for bidisperse mixtures of rods of different diameters and different lengths. The phase behavior of mixtures of *fd* and *fd* coated with poly(ethylene-glycol), two particles of identical length and different diameter, was measured. Bidisperse rod mixtures can exhibit isotropic-cholesteric (isotropic-nematic), isotropic-cholesteric-cholesteric (isotropic-nematic-nematic) and cholesteric-cholesteric (nematic-nematic) coexistence with increasing concentration, depending on the relative aspect ratio of the two rod types. The stability and evolution of the nematic-nematic coexistence region is studied in detail. Theoretical phase diagrams corresponding to the experimental conditions are also presented and compared with the measured results.

In Chapter 7, we investigate the nematic-smectic phase transition of monodisperse colloidal rod-sphere copolymers. In analogy to the familiar case of block copolymers and amphiphiles (surfactants, lipids, etc.), microphase separation of these colloidal copolymers is expected to occur due to entropic interactions. In this chapter we calculate the stability of a smectic phase of these copolymers in a parallel geometry. We additionally present a description of the experimental bio-chemical synthesis of these particles using M13 virus as our rod and a polymer (DNA or poly(ethylene glycol) as our sphere. We verify the feasibility of this M13/polymer complex and describe the future direction of these experiments.

An appendix describing the detailed biological protocols for the production of the bacteriophage used in the above experiments is also included in this thesis.

Chapter 2

The isotropic-cholesteric phase transition of filamentous virus suspensions as a function of rod length and charge

The viruses studied are genetically engineered, charged, semiflexible filamentous bacteriophages that are structurally identical to M13 virus, but differ either in contour length or surface charge. While varying contour length (L) we assume the persistence length (P) remains constant, and thus we alter the rod flexibility (L/P). Surface charge is altered both by changing solution pH and by comparing two viruses, *fd* and M13, which differ only by the substitution of one charged for one neutral amino acid per virus coat protein. We measure both the isotropic and cholesteric coexistence concentrations as well as the nematic order parameter after unwinding the cholesteric phase in a magnetic field as a function of rod surface charge, rod length, solution ionic strength and solution pH. The isotropic-cholesteric transition experimental results agree semi-quantitatively with theoretical predictions for semiflexible, charged rods.

2.1 Introduction

For a suspension of rigid rodlike particles, Onsager determined that hard-core interactions alone are sufficient for inducing an entropy driven phase transition from an isotropic phase, in which the particles are randomly oriented, to a nematic phase, in which the orientation of the particles is distributed about a preferred direction[1]. When the rodlike particles are semiflexible and/or charged, like many biopolymers such as DNA and F-Actin, the properties of the phase transition can differ significantly from those predicted for hard, rigid rods. Small amounts of flexibility are predicted [19] and observed [30, 40] to increase the stability of the isotropic phase and lead to a less ordered nematic phase. In this Chapter, we study the effects of flexibility on the isotropic-nematic (I-N) transition using suspensions of the rodlike charged, semiflexible M13 virus and M13 virus length-mutants. By varying the contour length (L) of our experimental charged rods while maintaining a constant persistence length (P) we change the rod flexibility (L/P). The persistence length is defined as the length over which tangent vectors along a polymer are correlated [18]. In our experiments the flexibility of the rods remains within the semiflexible limit, where $P \sim L$. The effect of surface charge on the I-N transition of charged rods is also investigated. Surface charge is varied by modifying both the surface chemistry of the rods and the solution chemistry, by changing pH.

While Onsager developed the original theory for the isotropic-nematic transition of hard and charged rigid rodlike particles, Khokhlov and Semenov were responsible for incorporating flexibility into this theory [19]. They extended Onsager's theory to include systems of semiflexible rods with a large length (L) to diameter (D) aspect ratio (L/D) and arbitrary persistence length. They explicitly calculated the equilibrium properties of the I-N phase transition in the limit of very flexible $L/P >> 1$ and very rigid $L/P << 1$ rods and interpolated between the two limits to find the properties of semiflexible rod phase behavior. Shortly afterwards, Chen numerically calculated the concentrations of the coexisting isotropic and nematic phases as well as the order parameter of the coexisting nematic phase for arbitrary flexibility using Khokhlov-Semenov theory[23]. For rigid rods, the limit of stability of the isotropic phase is predicted to be $c_i = 4/b$, where c_i is the number density and $b = \pi L^2 D/4$, the average excluded volume in the isotropic phase [41]. For flexible rods, Khokhlov-Semenov theory predicts that slight semiflexibility will increase the stability of the isotropic phase by increasing bc_i, and will narrow the I-N coexistence region. Flexibility is also predicted to significantly lower the nematic order parameter at coexistence. The nematic order parameter S is the second moment of the orientational distribution function of the rods, $f(\theta)$, or $S = 2\pi \int P_2(\cos(\theta)) f(\theta) d\theta$, where P_2 is the second Legendre polynomial. For a completely aligned nematic $S = 1$, whereas for an isotropic phase $S = 0$. For rigid rods the predicted nematic order parameter at coexistence is $S = 0.79$ [15]. The predictions from the Khokhlov-Semenov theory show quantitative agreement with the measured I-N transition for suspensions of charged semiflexible virus *fd*, charged polymer xanthan, and neutral polymer PBLG [30, 40].

Electrostatic interactions are incorporated into the Onsager model by rescaling the bare rod diameter D to a larger effective diameter D_{eff} which depends on the ionic properties of the particle and the solution [1, 16]. D_{eff} is calculated from the second virial coefficient of Onsager's free energy equation for charged rigid rods. In Fig. 2.1 we plot D_{eff} as described by Stroobants *et al.* [16] as functions of ionic strength and rod surface charge. The non-linear Poisson-Boltzmann equation used in Stroobants description of D_{eff} was solved numerically using the approximations developed by Philip and Wooding [17]. With increasing ionic strength D_{eff} decreases approaching the bare rod diameter. Past experiments have shown that D_{eff} accurately describes the

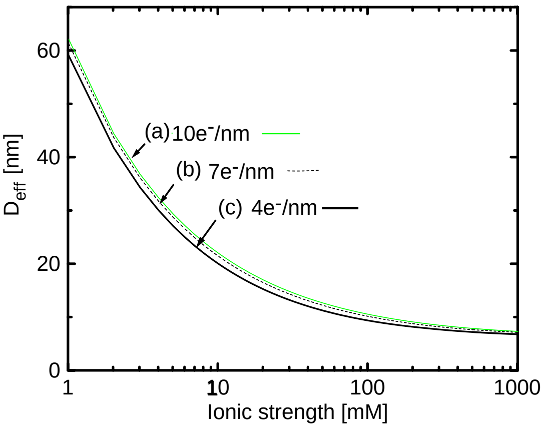

Figure 2.1: (Color Online) Effective diameter as a function of ionic strength and surface charge. With increasing ionic strength D_{eff} approaches the bare diameter of *fd* (M13) $D = 6.6$ nm. The effective diameter is plotted for surface charges of 10 e^{-}/nm, 7 e^{-}/nm and 4 e^{-}/nm. These surface charge densities are the same as those measured for (a) *fd* at pH 8.2, (b) M13 at pH 8.2 or *fd* at pH 5.2, and (c) M13 at pH 5.2. At these surface charge densities D_{eff} is insensitive to variation in charge.

ionic strength dependence of the I-N transition of *fd* virus suspensions [30]. For highly charged rods, the effect of surface charge on D_{eff} is small as the non-linear nature of the Poisson-Boltzmann equation leads to counterion condensation near the colloid surface which renormalizes the bare surface charge to a lesser effective charge, which is nearly independent of the bare surface charge. In the nematic phase, the effective diameter increases due to an added effect called “twist” which is characterized by the parameter $h = \kappa^{-1}/D_{\mathrm{eff}}$, where κ^{-1} is the Debye screening length. The effect of twist on D_{eff}, however, is predicted to be small for *fd* [30], and we neglect it here. Studying the influence of ionic strength and surface charge on the I-N phase behavior tests if D_{eff} can be accurately used to map charged rod phase behavior to hard-rod theories.

Onsager’s theory is based on an expansion of the free energy truncated at the second virial level, so that only two-particle interactions are considered. This assumption has been shown to be accurate in the limit of very long rods, where $L/D > 100$ [26], or for very dilute suspensions. In our experimental system, however, decreasing the ionic strength rapidly decreases our effective aspect ratio to values far below the $L/D = 100$ limit. In order to accurately predict the phase behavior of rods with an effectively small aspect ratio, the theoretical free energy needs to incorporate third and higher virial coefficients. Scaled particle theory (SPT), which incorporates all higher virial coefficients in an approximate way is one theory which accomplishes this[27]. A scaled particle theory for hard rigid rods was originally developed by Cotter [27]. More recently we have expanded this theory to include charge and semiflexibility [42, 28]. In conjunction with the Khokhlov-Semenov second virial theory we use this scaled particle theory to interpret our experimental results.

In this Chapter we present experimental measurements of the isotropic-nematic phase transition of semiflexible charged colloidal rods as a function of rod length, surface composition, solution pH, and solution ionic strength. We measure both the coexistence concentrations and the nematic order parameter and compare our results to both Onsager's theory, by way of Chen's numerical calculation[23], and scaled particle theory. For our model rods we use monodisperse suspensions of charged semiflexible rodlike *fd* virus, wild type M13 virus, and mutants of M13 virus which differ from the wild type only by their contour length. In solution, these particles exhibit isotropic, cholesteric (or chiral nematic), and smectic phases [43, 30, 35, 37]. Suspensions of *fd* have been previously shown to exhibit an I-N transition which agrees with theoretical predictions for semiflexible rods with an effective diameter D_{eff} [30]. M13 virus is structurally identical to *fd* virus, differing only in surface charge, making these two particles an ideal system for studying the influence of bare surface charge on the isotropic-nematic transition. Additionally, by comparing the I-N phase behavior of each of the M13 mutants, which except for length are structurally identical, and therefore by assumption have the same persistence length, we measure the influence of flexibility, defined as the ratio L/P on this transition. Though *fd* and M13 exhibit a cholesteric phase, the free energy difference between the cholesteric and the nematic phase is much smaller than the difference between the isotropic and nematic phases [39]. This allows us to compare our results to theoretical predictions for the isotropic-nematic (I-N) transition. We refer to the cholesteric phase as the nematic phase henceforth.

Motivation for these length and surface charge dependent measurements of the I-N transition arose because new measurements of the nematic-smectic (N-S) transition in this same system [44] exhibit measurable surface charge dependence and ionic strength dependence which can not be accounted for by treating the virus as a hard rod with a diameter D_{eff}, in contrast to our previous measurements, which were limited in range of ionic strength [35]. The new N-S measurements inspired a closer look at the ability of D_{eff} to describe the effects of surface charge on the I-N transition. New measurements of the N-S transition as a function of length also indicate that semiflexibility has no measurable effect on the N-S transition for the limited range studied, which is as predicted, but which is in sharp contrast to the large predicted effect of flexibility on the I-N transition for the same range. The measurements presented here of the I-N transition as a function of charge and flexibility will contribute to the understanding of the relative importance of these variables in the evolution of the liquid crystalline ordering of charged semiflexible rodlike particles with concentration.

2.2 Materials and Methods

Properties of *fd* and wild type M13 include length L =0.88 μm, diameter D = 6.6 nm, persistence length P =2.2 μm and molecular weight $M = 1.64 \times 10^7$ g/mol[14]. Each virus consists of approximately 2700 coat proteins helicoidally wrapped around single stranded DNA. The two viruses differ only by one amino acid per coat protein. In *fd* this amino acid is the negatively charged aspartate (asp$_{12}$), and in M13 it is the neutral asparagine (asn$_{12}$)[33]. Thus at near neutral pH *fd* has one more negative charge per coat protein (3.4 ± 0.1 e$^-$/protein) than M13 (2.3 ± 0.1 e$^-$/protein), which results in a net charge difference of approximately 30% [34]. X-ray diffraction studies are unable to clearly discern any structural differences between M13 and *fd* [45]. The M13 length-mutants share the same properties as wild type M13, varying only in length and molecular weight, which scales linearly with length. The M13 mutant have lengths of 1.2μm, 0.64μm, and 0.39μm. Wild type M13, *fd*, and M13K07 (the 1.2μm mutant phage) were grown using standard techniques [36]. The other two mutant phages were grown using the phagemid method, which produces bidisperse solutions of the phagemid and the M13K07 helper phage [36]. We chose two plasmid DNA sequences, PGTN28 (4665bp) and LITMUS38 (2820bp) (New England Biolabs, Cambridge MA) to form our phagemids of length 0.64μm and 0.39μm, respectively. Sample polydispersity was checked using gel electrophoresis on the intact virus, and on the viral DNA. Except for the phagemid solutions, which contained approximately 20% by mass helper phage M13K07, the virus solutions were highly monodisperse as indicated by sharp electrophoresis bands.

In a bidisperse system of long and short rods it is predicted that when isotropic and nematic phases are in coexistence, the longer rods will strongly partition into the nematic phase [7, 46]. Using this fractionation effect we attempted to purify the bidisperse suspensions of the phagemid and M13K07 helper phage. We observed partitioning of the long rods into the nematic phase by DNA agarose gel electrophoresis (2-3 fold more long rods in the cholesteric phase than in the isotropic phase in qualitative agreement with Lekkerkerker *et al.* [7]), but were unable to successfully measure a difference in long rod concentrations in the isotropic phase after successive iterations of fractionation. The effect of fractionation on the coexistence concentrations was assayed by comparing the isotropic and nematic concentrations of coexisting samples (about 50% of each phase in one sample) with the highest concentrations for which the samples remained completely isotropic and the lowest concentrations for which the samples remained completely nematic, respectively. The only difference we ob-

	A	B	C	D	E	F
pH	*fd* e$^-$/subunit	M13 e$^-$/subunit (charge of *fd* minus 1)	mobility ratio m_{M13}/m_{fd}	M13 e$^-$/subunit (electrophoresis)	*fd* e$^-$/nm	M13 e$^-$/nm
8.2	3.4± 0.1	2.4± 0.1	0.67	2.3± 0.05	10	7
5.2	2.3± 0.1	1.3± 0.1	0.5	1.2± 0.05	7	3.6

Table 2.1: Surface charge of *fd* and M13 at pH 8.2 and 5.2. (A) The charge of *fd* obtained by titration experiments [34]. (B) M13 has one less negative amino acid per coat protein than *fd*, thus the surface charge of M13 can be approximated by subtracting one charge per protein subunit from the *fd* surface charge values. (C) Ratio of electrophoretic mobility (m), determined from Fig. 2.2, of M13 to *fd*. (D) By multiplying the known *fd* charge by m, the linear surface charge density of M13 can be calculated. (E),(F) *fd* and M13 surface charge per unit length, respectively.

served was that the nematic concentration measured in coexistence with the isotropic phase was consistently about 5-10% lower than the nematic concentration measured when the sample was 100% nematic. The lower concentrations in the coexisting nematic phases are due to the partitioned long rods undergoing the I-N phase transition at lower mass concentrations. Because the effect of bidispersity is small, we report the phase behavior for the 0.39μm and 0.64 μm rods at the limits of the coexistence region with the understanding that the samples contain about ~20% (by mass) 1.2 μm rods.

All samples were dialyzed against a 20mM Tris-HCl buffer at pH 8.2 or 20mM Sodium Acetate buffer adjusted with Acetic Acid to pH 5.2. To vary ionic strength, NaCl was added to the buffering solution. The values for surface charge of *fd* and M13 at pH 8.2 and pH 5.2 are presented in Table 2.1. The surface charge of *fd* was determined by titration experiments [34], and the surface charge of M13 was calculated in two ways, both starting from the known *fd* surface charge. One way is to compare the molecular composition of *fd* and M13, and the second is to use the fact that because M13 and *fd* are identical except for their surface charge, their the electrophoretic mobilities are proportional to net surface charge [47]. In Fig. 2.2, we show using agarose gel electrophoresis of intact virus that *fd* migrates 200% faster than M13 at pH 5.2 and 150% faster at pH 8.2. Note in Table 2.1 we show that the

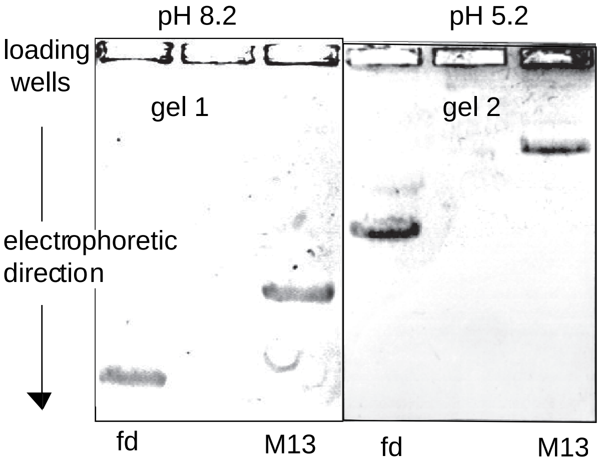

Figure 2.2: Agarose gel electrophoresis of *fd* and M13 virus at pH 8.2 (gel 1) and pH 5.2 (gel 2). At pH 5.2 the buffer was 40 mM Sodium Acetate, and at pH 8.2 the buffer was 40 mM Tris-Acetate-EDTA (TAE). Gels were run at ~1.0% agarose concentration and ~3.5 V/cm for 4 hours. Samples were placed in loading wells at a concentration of approximately 0.3 mg/ml. M13 and *fd* have the same length ($L = 0.88\mu$m) and diameter ($D = 6.6$nm), and differ only in surface charge. The ratio of electrophoretic migration distances between M13 and *fd* within each gel is therefore equal to the ratio of the surface charge. The electrophoresis bands for *fd* at pH 5.2 and M13 at pH 8.2 are not at the same migration distance, because the absolute migration distance is also a function of the buffer ions.

surface charge of M13 at pH 8.2 is the same as the surface charge of *fd* at pH 5.2.

All measurements were done at room temperature. The virus concentrations were measured by absorption spectrophotometry with the optical density (A) of the virus being $A_{269\mathrm{nm}}^{1\mathrm{mg/ml}} = 3.84$ for a path length of 1 cm. The nematic order parameter was obtained by unwinding and aligning the cholesteric phase in a 2T permanent magnet (SAM-2 Hummingbird Instruments, Arlington, MA 02474)[48] and measuring the sample birefringence. At 2T, the magnetic field has a negligible effect on nematic ordering[49, 50]. The nematic order parameters were calculated from the optical birefringence measurements obtained with a Berek compensator using the equation $\Delta n_{\mathrm{sat}} S = \Delta n$, where Δn_{sat} is the saturation birefringence. The value for $\Delta n_{\mathrm{sat}}/\rho = 3.8 \times 10^{-5}$[ml/mg], where ρ is the concentration of virus in [mg/ml], as determined for *fd* via x-ray diffraction [42].

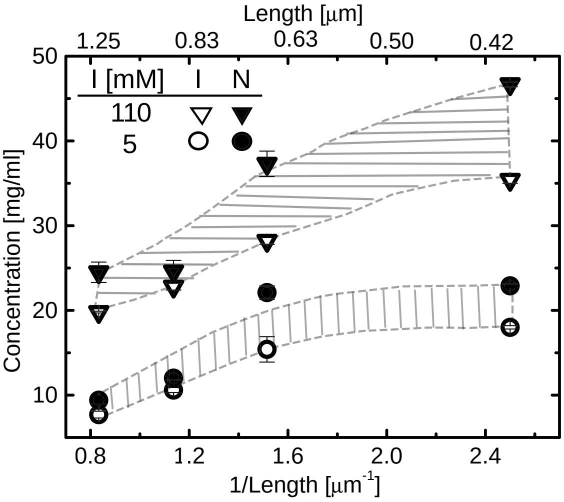

Figure 2.3: Isotropic-nematic coexistence concentrations as a function of M13 mutant contour length at 5 mM and 110 mM ionic strengths at pH 8.2. Open symbols represent the coexisting isotropic phase and solid symbols the nematic phase. Shaded areas are a guide to the eye indicating the coexistence regions. For rigid rods the coexistence concentrations $\rho_i \propto 1/L$ at a constant ionic strength (constant D_{eff}). Deviations from this relationship are most likely due to rod flexibility.

2.3 Results

2.3.1 Effect of length and flexibility on the isotropic-nematic transition

Figure 2.3 presents the length dependence of the I-N coexistence concentrations at high (110 mM) and low (5 mM) ionic strength. For rigid rods $b_{\text{eff}}c_i$, the dimensionless concentration of the isotropic phase in coexistence with the nematic phase, is predicted to be a constant, $b_{\text{eff}}c_i = 3.29$ [24], where $b_{\text{eff}} = \frac{\pi}{4}L^2 D_{\text{eff}}$ and $c_i = \rho_i N_A/M$. In c_i, ρ_i is the isotropic mass density, N_A is Avogadro's number, and M is the molecular weight. Because the molecular weight is proportional to viral length, $M = M_{wt}L/L_{wt}$, with M_{wt} and L_{wt} equal to the molecular weight and length of wild type M13. Thus $b_{\text{eff}}c_i = \rho_i L D_{\text{eff}}(\frac{\pi}{4}L_{wt}N_A/M) = 25\rho_i[\text{mg/ml}]L[\mu\text{m}]D_{\text{eff}}[\mu\text{ m}]$. Therefore, for rigid rods, $\rho_i = \text{const}/L/D_{\text{eff}}$, and at constant ionic strength (constant D_{eff}) ρ_i should be proportional to $1/L$. However, we observe that at a given ionic strength, the slope of ρ_i

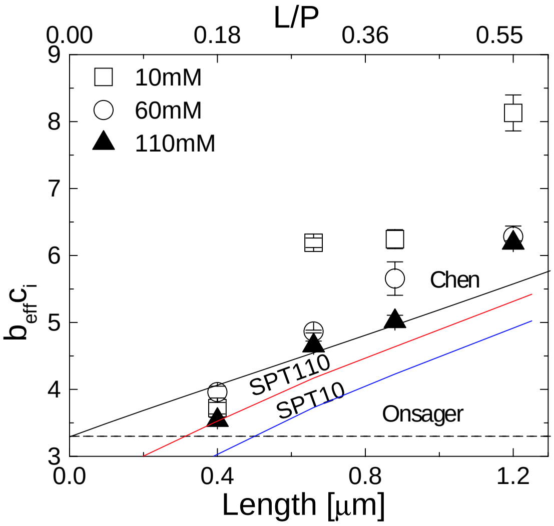

Figure 2.4: Dimensionless concentration of the isotropic phase in coexistence with the nematic phase as a function of M13 mutant contour length for three ionic strengths at pH 8.2. The concentration is defined as $b_{\text{eff}}c_i = \frac{\pi}{4}D_{\text{eff}}L^2N_i/V = 25.4\rho_i[\text{mg/ml}]L[\mu\text{m}]D_{\text{eff}}[\mu\text{m}]$. Scale on the top of the graph identifies the flexibility in terms of L/P with $P = 2.2\mu$m. If the rods are rigid the phase behavior is predicted to be independent of length (Onsager) (dashed line). Semi-flexible rods show increasing $b_{\text{eff}}c_i$ with increasing flexibility as predicted by Khokhlov-Semenov theory calculated by Chen (solid line). Scaled particle theory at 100 mM ionic strength (SPT110) and at 10 mM ionic strength (SPT10) indicate that $b_{\text{eff}}c_i$ depends on L/D_{eff}.

vs $1/L$ is not linear in Fig. 2.3, but instead increases with rod length, corresponding to an increase in $b_{\text{eff}}c_i$. This is shown more clearly in Fig. 2.4, where $b_{\text{eff}}c_i$ is plotted as a function of length. The increase in $b_{\text{eff}}c_i$ with length is in agreement with predictions for rods of increasing flexibility (L/P), as shown by the theoretical curves from Khokhlov-Semenov theory and from SPT for semiflexible rods with a persistence length of $P = 2.2\mu$m. At high ionic strength (I > 60 mM) we see good agreement with Khokhlov-Semenov theory calculated numerically by Chen (solid line) [23]. However with decreasing ionic strength, we measure an increase in the flexibility dependence of $b_{\text{eff}}c_i$. Subsequently, Khokhlov-Semenov theory only qualitatively describes the experimental results at low ionic strength. Agreement of the hard-rod Khokhlov-Semenov theory with our data is better at high ionic strength than at low ionic strength because the range of electrostatic interactions is weaker and L/D_{eff} is large, making the second virial approximation valid.

To interpret the observed increase in flexibility dependence of the phase transition with decreasing ionic strength, we turn to the scaled particle theory. The method for determining the scaled particle theoretical coexistence concentrations and nematic order parameters is described elsewhere [28]. In Fig. 2.4 we present the predicted SPT isotropic coexistence concentrations for rods with a diameter of 10.4 nm, (110 mM ionic strength), and 29.4 nm (10 mM ionic strength). At high ionic strength, SPT shows fair agreement with experimental results, and the theoretical curve for $b_{\text{eff}}c_i$ is close to that predicted by Chen for the infinitely long rod limit. Additionally, we observe in Fig. 2.4 that SPT indeed predicts a small dependence of $b_{\text{eff}}c_i$ on L/D_{eff}, in contrast to the L/D_{eff} independent second virial theory. This suggests that effective aspect ratio of the rods, which decreases with ionic strength, has a small effect on the I-N transition concentration. However, the L/D_{eff} dependence predicted by SPT is opposite the trend experimentally observed; increasing D_{eff}, by lowering ionic strength, increases the measured $b_{\text{eff}}c_i$ but lowers the scaled particle theory $b_{\text{eff}}c_i$. We argue that this discrepancy between scaled particle theory and experimental results at low ionic strength is due to the approximate treatment of electrostatics in D_{eff}, which is used not only as the theoretical hard rod diameter in SPT but also scales the experimental coexistence concentrations from ρ_i to $b_{\text{eff}}c_i$. D_{eff} is determined from using the second virial coefficient, and therefore is not necessarily accurate beyond that limit, ie. at low ionic strength. We note that the rescaled experimental coexistence concentrations, $b_{\text{eff}}c_i$, are extremely sensitive to the value of D_{eff} used to rescale the measured coexistence concentrations, ρ_i. Differences in D_{eff} are translated linearly to changes in the experimental $b_{\text{eff}}c_i$ by $b_{\text{eff}}c_i = 25\rho_i[\text{mg/ml}]L[\mu\text{m}]D_{\text{eff}}[\mu\text{m}]$. However, the predicted effect of changing L/D_{eff} on $b_{\text{eff}}c_i$, as shown by the SPT curves in Fig. 2.4, is much smaller than the measured change in $b_{\text{eff}}c_i$ with ionic strength. Agreement between SPT and our experimental results improves if the effective diameter at low ionic strength is smaller than predicted at the second virial limit.

The width of the coexistence region, $(\rho_n - \rho_i)/\rho_i$, was also measured and is presented in Fig. 2.5. At low ionic strength, the coexistence width qualitatively follows the decrease expected for increasing flexibility shown by the solid line due to Chen [23]. For most rod lengths the value for the coexistence width is larger than predicted by both Khokhlov-Semenov theory and by scaled particle theory. At short rod lengths this discrepancy is most likely due to the intrinsic bidispersity of the suspensions, which acts to widen the coexistence region [7]. A slow increase in the coexistence concentrations with time (possibly due to bacterial growth) [50] contributes to the large error bars, making comparison to predictions difficult. Above 10 mM ionic strength, where we see strong agreement between measurements of the coexistence concentrations and theoretical predictions, it is not apparent that there is any flexibility or ionic strength dependence in the width measurements.

The nematic order parameter obtained from measurements of the birefringence of the magnetically unwound and aligned cholesteric phase in coexistence with the

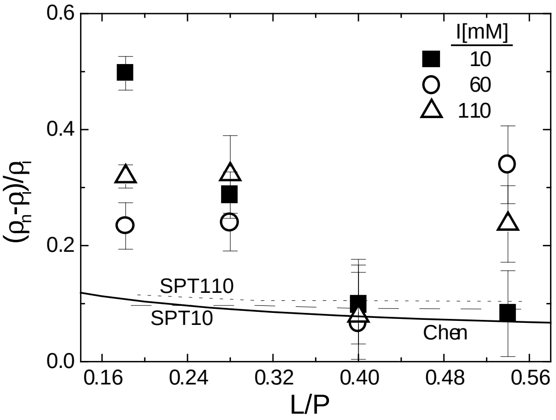

Figure 2.5: Width, $(\rho_n - \rho_i)/\rho_i$, of the coexistence region as a function of rod flexibility L/P. Results are plotted for three ionic strengths (10 mM, 60 mM, and 110 mM). Solid line is due to Chen for rods with $P = 2.2\mu$m [23]. Dotted and dashed lines are due to scaled particle theory for M13 rods (q=7e/nm) with a hard diameter D_{eff} at 110 mM (SPT110) and 10 mM (SPT10) ionic strength, respectively. For rigid rods, the Onsager prediction for the I-N coexistence width is 0.29 [1, 15]. The width of the coexistence region should decrease with increasing flexibility.

isotropic phase is presented in Fig. 2.6. We observe that at high ionic strengths, the nematic order parameter decreases with increasing length (increasing flexibility) in qualitative agreement with Khokhlov-Semenov theory calculated by Chen [23]. With decreasing ionic strength, however, the measured nematic order parameter increases, approaching Onsager's rigid-rod predictions, due to increasing the range of electrostatic interactions. This has also been observed for *fd* virus suspensions [42]. Furthermore, at very low ionic strength (5 mM ionic strength) the nematic order parameter becomes independent of rod length and equal to the predicted rigid rod value of $S = 0.8$. Scaled particle theory, as illustrated in Fig. 2.6, predicts that the nematic order parameter is largely independent of ionic strength. This suggests that the effective aspect ratio of the rods, which decreases with ionic strength, does not effect the nematic ordering. In addition, SPT agrees with the experimental measurements at high ionic strength better than Khokhlov-Semenov theory.

Another possible explanation for an increase in nematic order parameter with decreasing ionic strength is electrostatic stiffening. If the interparticle interactions are dominated by electrostatics, the flexibility of the rods might be screened. This effective "electrostatic persistence length" P_{el}, which makes a charged polymer more rigid when in solution, is a dominant effect in determining the flexibility of charged flexible polymers with $L/P \gg 1$. However, for the semiflexible M13 and *fd*, P_{el} is predicted to be less than one percent larger than the bare persistence length [51]. Additionally, the results for the coexistence concentrations presented in Fig. 2.4 indicate that with decreasing ionic strength the measured coexistence concentrations deviate further from Onsager's rigid-rod predictions. Thus the measured coexistence concentrations and nematic order parameters exhibit contradictory trends, away from Onsager's rigid rod prediction versus towards Onsager's rigid rod prediction, respectively, with decreasing ionic strength. Therefore, electrostatic stiffening of the polymer cannot account for the observed high values of the order parameter at low ionic strength. Neither scaled particle theory, nor variation in the electrostatic persistence length satisfactorily explain the low ionic strength data.

2.3.2 Effect of viral surface charge on the isotropic-nematic transition

In this section we compare the phase behavior of M13 virus to that of *fd* virus as a function of surface charge and ionic strength. Recall that these particles have the same length $L = 0.88\mu$m and persistence length $P = 2.2\mu$m. In Fig. 2.7 we present measurements of the isotropic coexistence concentrations as a function of viral surface charge at high and low ionic strength. The theoretical curve is from scaled particle theory for charged, semiflexible rods with $L/P = 0.4$. We only present the theoretical results from scaled particle theory in this section as this theory should more accurately describe the finite-length rod phase behavior than the second virial theory. In Fig. 2.7 we confirm that the charge dependence of the I-N coexistence concentrations

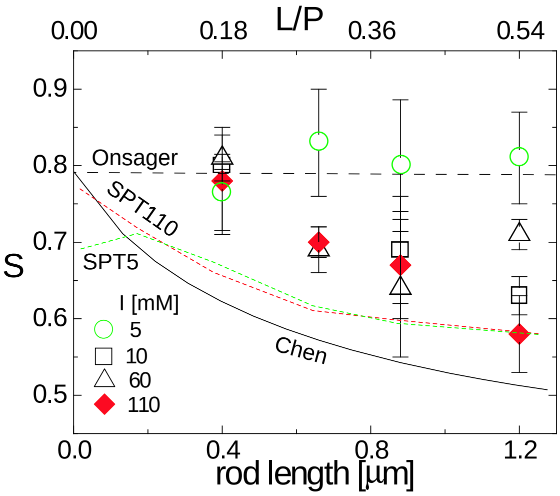

Figure 2.6: (Color online) Nematic order parameter at coexistence as a function of rod length for four different ionic strengths. Solid black line represents the theoretical calculation by Chen [23] for the order parameter as a function of flexibility (L/P) indicated by the scale on the top of the graph. The dashed line is the theoretical nematic order parameter for rigid rods, $S = 0.79$[1, 15]. The scaled particle curves (dotted lines) are calculated as in [42] for virus rods at 110 mM (SPT110) and 5 mM (SPT5) ionic strength. Theoretical curves were calculated for rods with a persistence length of 2.2μm. The measured order parameter decreases with increasing particle length at high ionic strength, but remains constant at low ionic strength.

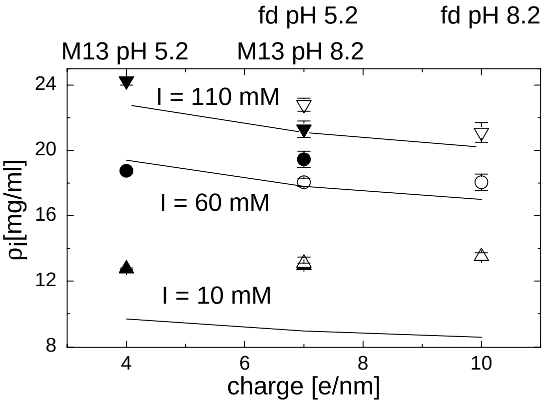

Figure 2.7: Coexisting isotropic phase concentrations ρ_i as a function of particle surface charge for three ionic strengths, 10 mM, 60 mM, and 110 mM. Solid symbols are wild type M13 and open symbols are *fd* suspensions. Suspension pH is labeled above the graph for M13 and *fd* samples. Solid line is from scaled particle theory for semiflexible hard rods with a diameter D_{eff} and $L/P = 0.4$. The charge dependence of the phase transition is well described by theory for ionic strengths of 60 mM and 110 mM.

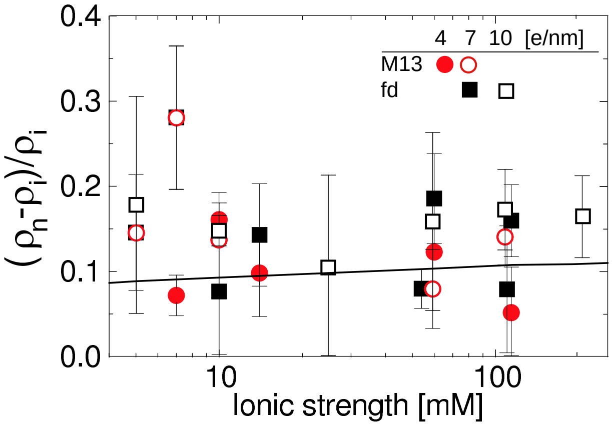

Figure 2.8: (Color online) Width of the isotropic-nematic coexistence region for wild type M13 and *fd* rods at three different surface charges as a function of ionic strength. Both M13 and *fd* have a length of $L = 0.88\mu$m. Solid symbols are at pH 5.2 and open symbols are at pH 8.2 for M13 (circles) and *fd* (squares) suspensions. Solid line is from scaled particle theory for hard semiflexible rods with $L/P = 0.4$ and is independent of rod surface charge. The Onsager prediction for the I-N coexistence width in dimensionless units of bc for hard rigid rods is $(4.19 - 3.29)/3.29 = 0.29$ [1, 15]. The coexistence width does not clearly show any charge dependence.

is accurately described by scaled particle theory at high ionic strengths. However, the efficacy of D_{eff} as a means for incorporating all electrostatic interactions again diminishes at low ionic strength (I<60 mM), as seen previously in Fig. 2.4 and in Fig. 2.6.

Fig. 2.8 presents the width of the coexistence region as a function of charge and ionic strength. The width of the coexistence region is independent of the surface charge of the rods and agrees (within large error bars) with scaled particle theory predictions. Both the measured coexistence concentrations and coexistence widths show that the effect of surface charge on the electrostatic interactions which drive the I-N phase transition are weak, which is consistent with the idea of charge renormalization incorporated into the calculations of D_{eff}.

Nematic order parameters obtained from measurements of the birefringence of magnetically unwound and aligned cholesteric samples of M13 at pH 8.2 are compared to previous measurements of *fd* suspension nematic order parameters, measured via x-ray diffraction techniques, also at pH 8.2 [42], in Fig. 2.9. Recall that the nematic order parameter of *fd* is known to be proportional to the birefringence of the suspension by the relationship $S = \Delta n/\Delta n_{\text{sat}}$ where $\Delta n_{\text{sat}} = 3.8 \times 10^{-5}$ml/mg [42]. The order parameter of M13 was measured at I-N coexistence as a function of ionic strength, and deep within the nematic phase for high (110 mM) and low (10 mM) ionic strength. Theoretical predictions from scaled particle theory for the nematic order parameter of hard semiflexible rods with $L/P = 0.4$ are also shown in Fig. 2.9. The order parameters of M13 and *fd* were found to be equal as a function of ionic strength and concentration, indicating that the surface charge difference of 30% between the two particles does not affect nematic ordering. The insensitivity of the nematic order parameter to surface charge is consistent with the surface charge renormalization incorporated into D_{eff} calculations (Fig. 2.1) [30]. The strong agreement of M13 and *fd* order parameters also indicates that these two different virus particles have the same birefringence per particle, $\Delta n_{\text{sat}} = 3.8 \times 10^{-5}$ml/mg [42]. Additionally, we again observe that the scaled particle theory fits the measured order parameter best for high ionic strength data.

2.4 Conclusion

At high ionic strengths, where the range of electrostatic interactions are small and L/D_{eff} is large, the isotropic-nematic transition of the experimental system of charged semiflexible bacteriophages is well described by Khokhlov-Semenov theory for semiflexible charged rods. Increasing flexibility increases the coexistence concentrations $b_{\text{eff}}c_i$ (Fig. 2.4) and lowers the nematic order parameter (Fig. 2.6). In the region of high ionic strength, D_{eff} accurately describes both the charge dependence and ionic strength dependence of the isotropic-nematic phase transition (Fig. 2.7). At

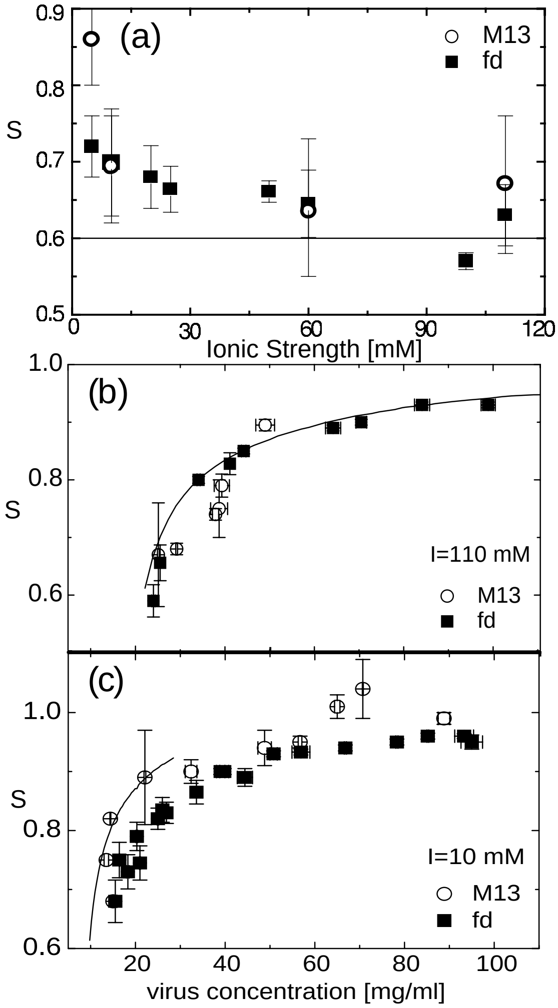

Figure 2.9: Order parameter of the nematic phase (a) coexisting with the isotropic phase as a function of ionic strength (b)as a function of concentration at 110 mM ionic strength and (c) as a function of concentration at 10 mM ionic strength pH 8.2. Values for M13 were obtained by birefringence measurements and values for *fd* were obtained previously by x-ray diffraction [42]. Solid lines are scaled particle theory for semiflexible hard rods of diameter D_{eff} and $L/P = 0.4$. The order parameters for M13 agree with those measured for *fd* independent of concentration and ionic strength.

low ionic strength, however, we find that the I-N coexistence concentrations and the nematic order parameter do not agree with theoretical predictions from either Onsager's second virial theory, or scaled particle theory. At low ionic strength, the flexibility dependence of the nematic order parameter is much weaker than expected (Fig. 2.6), but the flexibility dependence of the coexistence concentrations is much stronger than expected (Fig. 2.4). Because of these contradictory results we suggest that the disagreement between theoretical predictions and experimental data at low ionic strength is due to the approximate incorporation of the electrostatic interactions into the theoretical free energy via D_{eff}.

Chapter 3

The influence of charge and flexibility on smectic phase formation in virus rod suspensions

We present experimental measurements of the cholesteric-smectic phase transitions of suspensions of charged semiflexible rods as a function of rod flexibility and surface charge. The rod particles are structurally identical to M13 virus but vary in either contour length, and therefore ratio of persistence length to contour length, or surface charge. Surface charge is altered by changing solution pH and by comparing M13 to *fd* virus, which differ only by the substitution of a single charged amino acid for a neutral one per viral coat protein. Phase diagrams are measured as a function of particle length, particle charge and ionic strength. The experimental results are compared with existing theoretical predictions for the phase behavior of flexible rods and charged rods. In contrast to the isotropic-cholesteric transition, where theory and experiment agree, the nematic-smectic transition exhibits complex charge and ionic strength dependence not predicted by theory. Possible explanations for these unexpected electrostatic interactions are discussed.

3.1 Introduction

In a suspension of hard or charged rods, purely repulsive entropic interactions are sufficient to induce liquid crystal ordering. Theoretically, hard rods exhibit isotropic, nematic and smectic phases with increasing concentration [1, 25, 52]. Unfortunately, although theoretically simple objects, production of hard, rigid monodisperse rods is very difficult. Rigid and flexible polyelectrolyte rods, however, are abundant, especially in biological systems, which by nature lend themselves to mass-production. Viruses, such as *fd*, M13 and Tobacco Mosaic Virus (TMV) are a unique choice for use in studying liquid crystal phase behavior, in that they are biologically produced to be monodisperse and are easily modified by genetic engineering and post-expression chemical modification. These virus particles are also, to our knowledge, the only colloidal systems known to exhibit the predicted hard-rod phase progression (isotropic-nematic-smectic) [53, 14]. Suspensions of charged β-FeOOH rods [54] are the only other system known to form a stable smectic phase. Accurately describing the nematic-smectic (N-S) transition for charged and/or flexible rods is important because it elucidates the nature of interparticle interactions. Even though qualitative theories have been developed to describe the effects of electrostatics *or* flexibility on the N-S phase boundary [32, 35, 55], many challenges remain to correctly describe this transition for charged *and* flexible particles. Near the N-S transition, the particles are at very high concentrations, and as we will show, dilute-limit approximations of interparticle interactions which are appropriate at the isotropic-nematic transition cannot be used. Additionally, our results add insight into the ordering of other important rodlike polyelectrolytes including biopolymers like DNA and F-actin.

In this Chapter we will test the limits of current theoretical predictions for the nematic-smectic phase transition in two ways. First, we measure the ionic strength dependence of the phase transition for filamentous virus of identical structure and varied length. By changing the rod length and leaving local particle structure constant, the rod flexibility is altered as defined by the ratio of persistence length P, or half the Kuhn length, to contour length L, or P/L. In our experiments the flexibility of the particles remains within the semiflexible limit, meaning $P \sim L$. Altering the particle flexibility probes the competition between rigid and flexible rod phase behavior in the semiflexible limit. It also allows us to probe the efficacy of current methods for incorporating electrostatic repulsion into hard-particle theories through measurements of a large number of values of ionic strength and particle size. Second, we measure the nematic-smectic phase transition for filamentous virus of different charge. Altering the surface charge by two independent techniques, solution chemistry and surface chemistry, probes the importance of the details of the surface charge distribution in determining long range interparticle interactions. By varying these three independent variables, length, charge and solution ionic strength, we systematically determine how electrostatic interactions and flexibility experimentally effect the nematic-smectic phase boundary.

As in Chapters 2 and 3 we use the rodlike semiflexible bacteriophages *fd* and M13 for our colloidal system. M13 and *fd* differ from one another by only one amino acid per coat protein; the negatively charged aspartate (asp_{12}) in *fd* is substituted for the neutral asparagine (asn_{12}) in M13 [33], and thus are ideal for use in studying charge dependence of phase behavior. Changes in the surface charge of the particles were also achieved by varying the pH of the solution [34]. By varying the length of the M13 DNA we created M13 mutants which differ only in contour length. The M13 mutants have the same local structure, and thus we assume persistence length, as M13. These mutant M13 viruses were used to measure the flexibility dependence of the nematic-smectic phase transition.

3.2 Materials and Methods

Properties of *fd* and M13 include length $L = 0.88\mu$m, diameter $D = 6.6$nm, and persistence length $P = 2.2\mu$m [14]. The M13 mutants have lengths of 1.2μm, 0.64μm, and 0.39μm[37]. Virus production is explained in the Appendix. Two of the length-mutants (0.64μm and 0.39μm) were grown using the phagemid method [36, 37] which produces bidisperse solutions of the phagemid and the 1.2 μm helper phage. Sample polydispersity was checked using gel electrophoresis on the intact virus, and on the viral DNA. Excepting the phagemid solutions which were 20% by mass 1.2μm helper phage, virus solutions were highly monodisperse as indicated by sharp electrophoresis bands. A characteristic of a high degree of monodispersity is the ability of these virus to all form well defined smectic phases, as shown in Fig. 3.1. The bidispersity in the phagemid solution does not suppress smectic phase formation [37].

All samples were dialyzed against a 20mM Tris-HCl buffer at pH 8.2 or 20mM Sodium Acetate buffer adjusted with Acetic Acid to pH 5.2. To vary ionic strength, NaCl was added to the buffering solution. The linear surface charge density of *fd* is approximately $10e^-$/nm at pH 8.2 and $7e^-$/nm at pH 5.2 [34]. M13 surface charge was calculated from the known *fd* surface charge by comparing both molecular composition and electrophoretic mobilities[56]. As M13 and *fd* identical accept for their surface charge, electrophoretic mobility is proportional to net surface charge [47]. By multiplying the known *fd* charge by the ratio of M13 and *fd* electrophoretic migration (*fd* migrates 200% faster than M13 at pH 5.2 and 150% faster at pH 8.2), we find that the linear surface charge density of M13 is approximately $7e^-$/nm at pH 8.2 and $3.6e^-$/nm at pH 5.2, in agreement with calculations from molecular composition.

Since knowing the surface charge of the virus is critical to our analysis of the N-S transition, we experimentally measured the pH of the virus solutions at concentrations in the nematic phase just below the N-S transition. We found that for an initial buffer solution at pH 8.2 (Tris-HCl buffer pKa= 8.2), the pH of virus

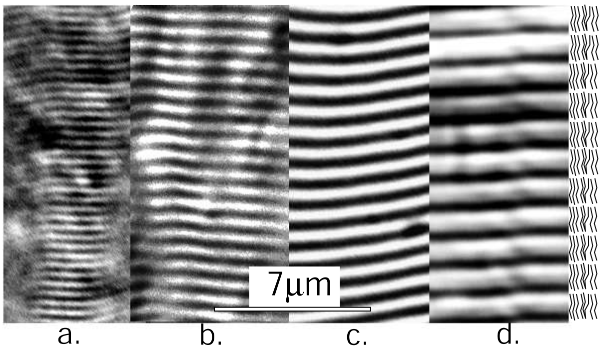

Figure 3.1: Differential interference microscopy (DIC) image of smectic layer lines of M13 virus mutants of four different lengths.(a) Litmus phagemid $L = 0.39\mu$m. (b) PGTN28 phagemid $L = 0.66\mu$m. (c) Wild type *fd* virus $L = 0.88\mu$m. (d) M13K07 helper phage $L = 1.2\mu$m.

suspensions near the smectic phase is slightly lower, but still well within the buffering pH range (pH=pKa±1). The surface charge does not change significantly over this range [34]. At pH 5.2 (Acetic acid buffer pKa= 4.76) the measured pH of the virus suspensions near the N-S transition was slightly higher than 5.2. This shift further away from the pKa may effect the buffering ability of the solution and subsequently the phase behavior. Additionally, the shift in pH becomes stronger with decreasing ionic strength, most likely due to the relative concentration of buffer ions (20 mM) to virus counterions (50-100 mM). The implications of these measurements are discussed further in the Results section.

All measurements were done at room temperature. The concentration of the phases was measured by absorption spectrophotometry with the optical density (A) of the virus being $A^{\mathrm{1mg/ml}}_{\mathrm{269nm}} = 3.84$ for a path length of 1 cm.

3.3 Electrostatic Interactions

The total rod-rod interparticle interaction includes a combination of hard core repulsion and long ranged electrostatic repulsion. We present two possible ways to incorporate the electrostatic repulsion into hard-rod theories. First, it is possible to define an effective hard core diameter (D_{eff}) larger than the bare diameter D, which is calculated from the second virial coefficient of the free energy for charged rods [1, 57]. Increasing ionic strength decreases D_{eff}, but for highly charged colloids, like M13 and *fd*, the effect of surface charge on D_{eff} is small as the non-linear nature of the Poisson-Boltzmann equation leads to counterion condensation near the colloid surface which renormalizes the bare surface charge to a lesser effective charge, which is nearly independent of the bare surface charge [30, 58]. It has been experimentally verified that this effective diameter accurately describes the electrostatic repulsion between virus particles at the isotropic- nematic (I-N) transition in the limit of large L/D_{eff} [30, 56]. Previously, we showed that a D_{eff} independent of virus concentration could describe the electrostatic interactions of virus suspensions at the nematic-smectic transition [35]. However, we note that the use of D_{eff} beyond the regime where the second virial coefficient quantitatively describes the system (above the isotropic-nematic transition) is not necessarily justified. We show in this Chapter that this crude treatment of the electrostatic interactions neglects significant features better described by the scaled particle theory described in the following paragraph.

An alternative effective diameter was developed by Kramer and Herzfeld. They calculate an "avoidance diameter" D_{a} which minimizes the scaled particle expression for the free energy of charged parallel spherocylinders as a function of concentration[32]. With respect to ionic strength, D_{a} exhibits the same trend as D_{eff}, but is defined to be independent of charge within the "highly charged" colloid regime. Specifically, the renormalized surface charge of the colloidal rods in Kramer and Herzfeld's theory is defined to be 1 $e^-/7.1$Åfor any colloidal rod (including *fd* and M13) with a surface charge greater than or equal to 1 $e^-/7.1$ Å[32]. The advantage of this theory over Onsager's effective diameter is its use of scaled particle theory. By using the scaled particle theory, third and higher virial coefficients are accounted for in an approximate way [59, 27], making this "avoidance diameter" more appropriate for incorporating electrostatic interactions at the nematic-smectic transition. The disadvantage is that the free energy expression developed by Kramer [32] does not reduce to Onsager's theory in the absence of no electrostatic interactions. Kramer's calculations [32] qualitatively reproduce previously published data for the N-S transition of *fd* virus, but the limited range of data previously available did not include some of the interesting features described in this theory, which we are now able to test. Having an appropriate way to describe the electrostatic interactions between rods is essential for separating the effects of charge, ionic strength and flexibility on the N-S phase behavior we now present.

3.4 Results

The location of the N-S transition was determined by measuring the highest nematic concentration (ϕ^{N}) and the lowest smectic concentrations (ϕ^{S}) observed, with $\phi = \pi L D^2 c/4$ and c equal to the nematic or smectic rod number density respectively. Because of the high viscosity of the suspensions near the N-S transition, bulk separation of the nematic and smectic phases is not observed, however, smectic or nematic domains can be observed using differential interference contrast microscopy (DIC) in coexistence with predominantly nematic and smectic bulk phases, respectively. Typically coexistence is observed as ribbons of smectic phase reaching into a nematic region.

Measurements of ϕ^S are presented in Fig. 3.2 as a function of the M13-mutant particle length, and therefore virus flexibility by L/P, for multiple ionic strengths. The influence of flexibility on the nematic-smectic transition of hard-rods has been well studied theoretically [60, 55]. Adding a small amount of flexibility is expected to drive the smectic phase to higher concentrations, from the predicted hard-rigid-rod concentration of ϕ^S=0.47 [25], to approximately $0.75 \lesssim \phi^S \lesssim 0.8$ within the semi-

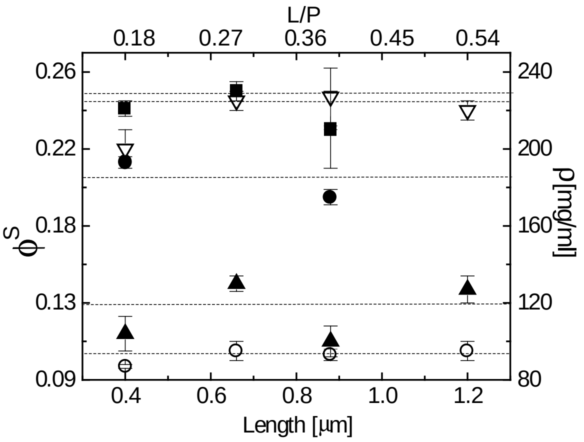

Figure 3.2: Smectic phase concentration ϕ^S at the N-S transition for multiple ionic strengths at pH 8.2 as a function of rod length L and flexibility L/P. Legend for ionic strengths is as follows: ○ 5 mM, ▲ 10 mM, ● 60 mM, ▽ 110 mM, ■ 150 mM. With increasing ionic strength ϕ^S increases due to increasing electrostatic screening. Dashed lines are a guide to the eye at constant ionic strength. Within experimental accuracy the smectic phase transition is independent of flexibility within the range $0.18 < L/P < 0.54$.

flexible limit[55]. Once within the semiflexible limit, however, ϕ^S is essentially independent of flexibility. At a constant ionic strength Fig. 3.2 shows that within experimental accuracy ϕ^S is independent of virus length, and thus independent of changing flexibility in the range of $0.18 < L/P < 0.24$, as predicted. This is in striking contrast to the significant flexibility dependence measured at isotropic-nematic transition for this same system of semiflexible M13 mutants which is described in [56]. At the isotropic-nematic transition the dimensionless concentration $bc = \phi^{\text{I-N}}L/D$ increases with increasing flexibility in agreement with theoretical predictions by Khokhlov and Semenov [19, 23], especially at high ionic strength where L/D_{eff} is large.

As seen in Fig. 3.2, ionic strength plays an important role in determining the phase boundaries by screening electrostatic interactions. To compare our charged-flexible-rod results with predictions for the N-S phase transition of hard rods, we graph in Fig. 3.3 ϕ^N_{eff} as a function of rod length. We define $\phi^N_{\text{eff}} = \phi^N(D^{\text{N}}_{\text{eff}})^2/D^2$. Because crossed charged rods have a lower energy than parallel rods $D^{\text{N}}_{\text{eff}}$ increases with particle alignment reaching a maximum possible value of $D^{\text{N}}_{\text{eff}} = 1.12D^{\text{iso}}_{\text{eff}}$, with $D^{\text{iso}}_{\text{eff}}$ equal to

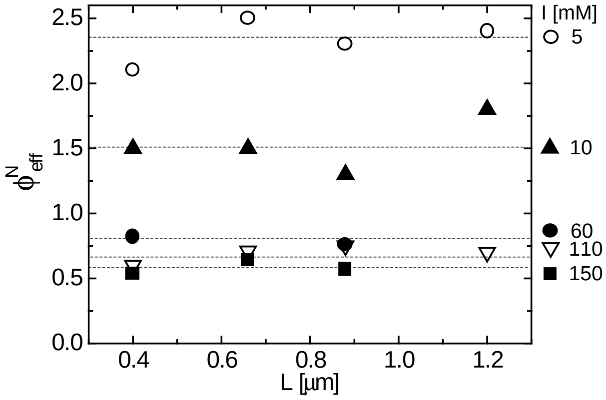

Figure 3.3: Nematic phase effective volume fraction ϕ^N_{eff} at the N-S transition for multiple ionic strengths at pH 8.2 as a function of L. Legend for symbols is to the right of the figure. Dashed lines drawn are a guide to the eye and are at constant ionic strength. Because ϕ^N_{eff} strongly depends on ionic strength, we conclude that $D^{\text{N}}_{\text{eff}}$ does not describe the electrostatic interactions at high virus concentrations.

the isotropic effective diameter, just below the smectic phase [57, 35]. The effective volume fraction ϕ^N_{eff} should be equivalent to the hard-flexible rod concentration and be independent of ionic strength if D^N_{eff} accurately models the interparticle electrostatic interactions. However, ϕ^N_{eff} depends quite strongly on ionic strength in Fig. 3.3. Previously, we observed $\phi^N_{\text{eff}} = 0.75$ independent of ionic strength for suspensions of *fd* virus [35]. Though our data agrees semi-quantitatively with this near I=60 mM, by expanding our measurements to include larger values ionic strength as well as multiple particle lengths, we clearly measure an ionic strength dependence in ϕ^N_{eff} with ϕ^N_{eff} ranging from 2.5 to 0.5. This large ionic strength dependence of ϕ^N_{eff} indicates that $D^{\text{N}}_{\text{eff}}$ is not sufficient for describing the electrostatic interactions at the N-S transition. This is not entirely surprising due to the fact that D_{eff} is strictly defined to be accurate at low concentrations where two-particle interactions are dominant.

We show in Fig. 3.4 the volume fraction of the nematic-smectic transition, ϕ^{N} and ϕ^{S} averaged over results from all particle lengths as a function of ionic strength. With increasing ionic strength the electrostatic repulsion between rods decreases approaching hard-rod phase behavior in the limit of very high ionic strength. We observe

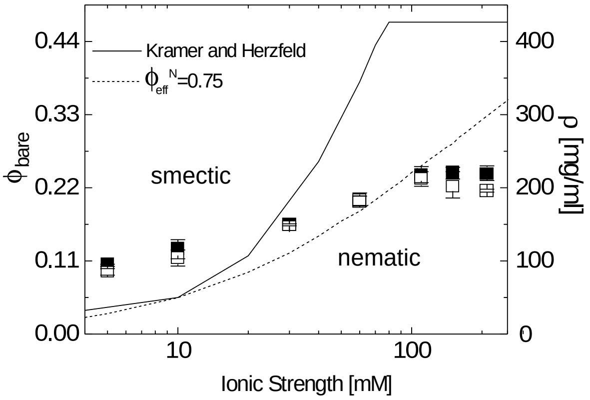

Figure 3.4: Average concentration of the nematic (open) and smectic (solid) phases at the N-S transition as a function of ionic strength at pH 8.2. Average is over the four M13 length mutants. Solid line is taken from simulations by Kramer and Herzfeld [32] for particles the same size as *fd* and with a renormalized surface charge of 1e$^-$/7.1 Å. Dashed line is $\phi_{\text{bare}} = \phi_{\text{eff}}^{\text{N}} * D^2/(D_{\text{eff}}^{\text{N}})^2$ with $\phi_{\text{eff}}^{\text{N}} = 0.75$.

that above approximately I=100 mM, ϕ^S becomes independent ionic strength due to a effective "close packing" of the rods in the smectic phase. This saturation at high ionic strength is consistent with the phase behavior predicted by Kramer for parallel charged spherocylinders with a concentration dependent avoidance diameter D_{a}, as mentioned previously [32]. However, Kramer's theory predicts a saturation concentration of $\phi_{\text{sat}}^S = 0.47$, or the theoretical hard-spherocylinder (I→ ∞) limit [32, 25], which is much higher than our experimental saturation value of $\phi_{\text{sat}}^{\text{S}} = 0.24$. This discrepancy is most likely due to the role of electrostatics being much stronger than predicted by D_{a}, as flexibility, our other independent variable, is predicted to increase the N-S transition concentration. Contrastingly, simply scaling ϕ^N by D_{eff}^2, does not capture this sudden saturation, as shown by the dashed curve for $\phi_{\text{eff}}^N = 0.75$, in Fig. 3.4. Both approximations for the electrostatic interactions qualitatively reproduce some features of the N-S transition yet they both differ significantly from the experimentally observed behavior.

In addition to measuring the effect of ionic strength on the phase behavior, we also measured the effect rod surface charge. We measure the phase behavior of *fd* and M13 at pH 5.2 and pH 8.2. Fig. 3.5 presents the ionic strength and pH dependence

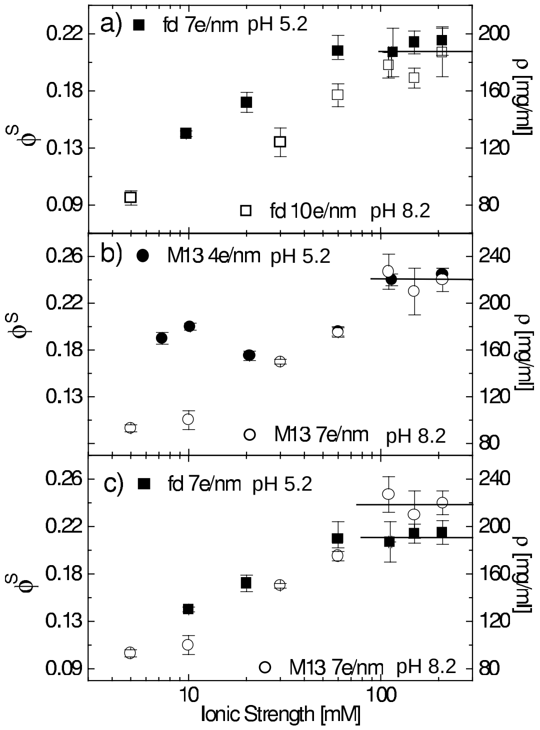

Figure 3.5: Nematic-smectic phase transition concentration as function of ionic strength for suspensions of a) *fd* and b) M13 at pH 5.2 (solid) and pH 8.2 (open). Figure c) shows M13 (pH 8.2) and *fd* (pH 5.2) at 7e/nm surface charge. Solid lines highlight the ionic strength independence at high ionic strength.

of the N-S phase transition for *fd* (a) and M13 (b). Similar to the trend in Fig. 3.4, increasing ionic strength increases the N-S transition concentration, until about 100 mM ionic strength, above which ϕ^S is independent of ionic strength. Above about 100 mM, the *fd* phase boundary saturates around $\phi^S_{\text{sat}} \sim 0.21$, independent of pH, and the M13 phase boundary saturates around $\phi^S_{\text{sat}} = 0.24$, also independent of pH. Surprisingly, at these high ionic strengths, where the surface charge should be well screened, *fd* suspensions have a phase boundary at lower concentrations than the M13 suspensions, independent of pH.

At low ionic strength, below about 100 mM, the pH dependence of the N-S transition is stronger than at high ionic strength, as shown in Fig. 3.5a,b. Suspensions at higher pH (higher surface charge) consistently enter a smectic phase at lower concentrations. This is surprising because at the isotropic-nematic transition, where the charge dependence is well described by D_{eff}, the surface charge dependence of the phase transition is very small [56]. Additionally, the non-linearity of the Poisson-Boltzmann equation predicts that the long-range electrostatic potential between rods is insensitive to surface charge changes and thus pH changes [1, 57]. The high sensitivity of the N-S transition to changes in pH indicates that the charge independent nature of both D_{eff} and D_a does not correctly characterize the electrostatic interactions at the N-S transition.

It is also unexpected that M13 and *fd* would have different phase behavior even when both virus have the same predicted surface charge of 7e$^-$/nm, as shown in Fig. 3.4c. At low ionic strength the phase behavior is similar, but *fd* suspensions consistently enter the smectic phase at a slightly higher concentration. At high ionic strength, the reverse is true; *fd* has a lower phase transition concentration than M13 suspensions, as mentioned above. At low ionic strength, the slight difference in phase transition concentrations between M13 at pH 8.2 and *fd* at pH 5.2 could be due the measured increase in pH at low ionic strength and low pH. Shifts in the pH, particularly near the viral pKa ($\mathrm{pKa}_{fd} = 4$), i.e. at pH 5.2, can shift the viral surface charge. Because the measured pH is higher than the original buffer, the actual surface charge of the *fd* particles at pH 5.2 may have increased slightly. A small increase in the surface charge of the *fd* samples would account for the disagreement with the M13 measurements. We stress however, that this high sensitivity of the N-S transition to surface charge differences, is not predicted by either D_{eff} or D_a.

The difference between M13 and *fd* saturation concentrations at high ionic strength and equal surface charge (Fig. 3.5c), however, is not well explained by this argument. At high ionic strength, the measured pH of the concentrated virus solutions is not significantly different from the initial buffer pH, as mentioned in the Materials and Methods. However, at high ionic strength (I>110 mM) adjacent virus surfaces are separated by distances smaller than the virus diameter (6.6 nm) [42], which is on the order of the spacing between viral coat-proteins (1.6 nm) and the Debye screening length $\kappa = 3.0$ Å$/\sqrt{(I)} = 0.9$ nm. Because the rods are separated by distances on the order of the Debye screening length, the actual surface charge configuration of the viral rods can no longer be approximated as a continuous charge distribution as is done in the effective diameter calculation. Furthermore, it has been shown theoretically that discretization of the surface charges can change the predicted counterion condensation when compared to the non-linear Poisson Boltzmann equation [61]. Perhaps it is because we are in the regime where the surface charge configuration can no longer be neglected that we observe charge-configuration-dependent saturation of the nematic-smectic phase transition. Theoretical models or simulations of the electrostatic interactions of a dense, rod-like polyelectrolyte system, which include the detail of the surface charge configuration may shed light on the experimental differences between M13 and *fd* nematic-smectic transitions at high ionic strength.

3.5 Conclusion

In summary, we have presented the nematic-smectic phase diagram as a function of length, surface charge and ionic strength. We observed that in the semiflexible-rod limit the N-S phase boundary is independent of rod flexibility in contrast to the strong flexibility dependence seen at the isotropic-nematic transition. By studying the ionic strength dependance of this transition we observed that renormalizing ϕ^S by Onsager's effective diameter does not produce an ionic-strength independent phase transition concentration, which would be necessary to compare the flexible-rod phase behavior to hard-particle theories. Scaled particle theory and Kramer and Herzfeld's avoidance diameter qualitatively reproduce the observed N-S phase behavior, but more theoretical work is needed to find a way to compare the charged-flexible rod results to the hard-flexible rod theories available. Furthermore, significant differences were measured between M13 and *fd* N-S phase behavior, even when they shared the same surface charge. In Chapter 4 we similarly measure a difference in the cholesteric pitch in M13 *fd* suspensions when they also had equal surface charge. These results indicate that the electrostatic interactions between these rods are much more complicated than can be accounted for by calculating the interparticle potential assuming a uniform renormalized surface charge. We hypothesize that the electrostatic interactions between rods could be influenced by the configuration of the charged amino acids on the rod surface. Experimental confirmation of this could be found by measuring M13 and *fd* equations of state (pressure vs density), and thus the particle-particle interactions, as a function of solution salt and pH, as in techniques developed for DNA [62].

Chapter 4

Searching for the origin of chirality in the cholesteric phase of virus suspensions by varying viral charge and DNA/protein interactions

In this Chapter we present measurements of the cholesteric pitch of suspensions of chiral rodlike *fd* and M13 virus as a function of changing electrostatic interactions between virus particles and changing interactions between DNA base pairs within the virus particles. The electrostatic interactions are changed by changing the solution ionic strength and/or viral surface charge. Surface charge is altered both by changing solution pH and by comparing the two viruses, *fd* and M13, which differ only by the substitution of one charged for one neutral amino acid per virus coat protein, respectively. The inter-base-pair interactions are altered by the addition of silver ions, which complexes with the DNA, into the solution. With these measurements we hope to better understand the relationship between the intrinsic chirality of the virus particles and the macroscopic chiral nematic phase. We present evidence that both electrostatic and viral DNA/coat protein interactions directly affect the cholesteric phase. Future directions for experiments to probe the correlations between DNA/protien interactions and the cholesteric phase are also discussed.

4.1 Introduction

The charged semiflexible rodlike viruses *fd* and M13 are formed by a single stranded DNA around which 2700 coat proteins are helicoidally wrapped. They are therefore chiral rods exhibiting a helical charge distribution. They are also structurally identical accept for the substitution of a single neutral amino acid in M13 for a charged one in *fd* on each of the 2700 coat proteins. In solution, both viruses exhibit a cholesteric phase, where the rods orient locally about a nematic director which twists 360^o over a finite length. This length is referred to as the cholesteric pitch. Molecular chirality, however, does not guarantee a macroscopic chiral structure such as a cholesteric phase [63]. Other chiral viruses such as Tobacco Mosaic Virus (TMV) [64], and Pf1 [65], a virus with a helical structure extremely similar to *fd* and M13, exhibit only a nematic phase. Pf1 and fd, however have distinctly different DNA structures within the protein coat [66]. In this Chapter we propose that altering the DNA structure within the virus may influence the presence (or absence) of a cholesteric phase by altering the helicity of the whole virus via the viral DNA/protein interactions. We test this hypothesis by measuring the cholesteric pitch as a function of added silver ions, which intercalate into the enclosed viral DNA and have been shown to alter the microscopic helical properties of the enclosed DNA [67, 68]. Additionally, previous measurements have shown that ionic strength is one of the major physical parameters controlling the macroscopic chirality of colloidal liquid crystalline suspensions [65, 38]. In hopes of further understanding the role of electrostatic interactions between charged helical rods and the observed macroscopic chiral properties, we directly probe the effect of virus surface charge on the bulk chirality of the cholesteric phase by modifying both the surface chemistry of the rods and the solution chemistry, by changing pH.

Previously, M13 and *fd* virus rods have been shown to undergo a liquid crystal phase transition from the isotropic phase to the cholesteric phase with increasing concentration. This phase transition has been studied in detail for suspensions of both M13 and *fd* virus as a function of ionic strength and pH (see Chapter 2) and has been compared in detail to Onsager's theoretical predictions for the isotropic-nematic phase transition for charged semiflexible rods [1, 23]. The electrostatic interactions between the rods in the isotropic phase are typically incorporated into hard-rod theories by rescaling the bare rod diameter D to a larger effective diameter D_{eff} which depends on the ionic properties of the particle and the solution [1, 16]. This effective diameter depends only weakly on the bare surface charge of the rods (Fig. 2.1), due to counterion condensation near the colloid surface which renormalizes the bare surface charge to a lesser effective charge nearly independent of the bare surface charge. Correspondingly, the properties of the isotropic-cholesteric phase transition, which is predicted to occur at a volume fraction of $\phi = 4D_{\text{eff}}/L$ [1, 41] for long rigid rods, are expected to depend only weakly on the viral surface charge [30]. In Chapter 2, this was confirmed.

In the nematic (cholesteric) phase, there is an added effect called "electrostatic twisting" which acts to misalign adjacent charged rods. Electrostatic twisting is characterized by the parameter $h = \kappa^{-1}/D_{\text{eff}}$, where κ^{-1} is the Debye screening length [16]. Twist manifests itself by increasing the effective diameter. Electrostatic twist is also nearly independent of surface charge. Measurements in Chapter 2 of the nematic order parameter of the unwound cholesteric phase confirm that the nematic ordering of the viral suspensions is insensitive to any differences surface charge between M13 and *fd* virus particles. In this Chapter, however, we test the sensitivity of the cholesteric pitch to surface charge changes and find that it is indeed sensitive to the surface charge of the virus particles.

Theoretically, the transmission of microscopic helicity to macroscopic helicity is thought to be through direct chiral electrostatic interactions [69, 70]. In one of the most advanced theories of cholesteric assemblies of charged rods, proposed by Kornyshev for DNA, the specific details of the helical symmetry of a macromolecules surface charge pattern are suggested to be responsible for macroscopic twist [69]. However, recent results obtained on virus sterically stabilized with neutral polymer indicate that these theories probably do not capture all the essential elements of the connection between microscopic and macroscopic chirality in colloidal liquid crystals. Specifically, a system of *fd* virus sterically stabilized with neutral polymer has been shown to exhibit ionic strength *dependent* cholesteric properties [38], even though the rods have ionic-strength *independent* phase behavior [37]. In this system macroscopic chirality exists without direct electrostatic interactions. The helicity which drives the existence of the cholesteric phase is then somehow transmitted through the polymer layer. It has been proposed that, because *fd* is slightly flexible it may have helical superstructure (curl) associated with it [38]. This would allow for the helical information to be transferred through the polymer layer. Previous studies have shown that similar phages (phage X) indeed have a visible curl [71]. In Fig. 4.1 we present electron micrograph images comparing the curliness of X to that of *fd*. We hope that by changing the interactions within the virus we can learn more about the factors which contribute to the existence of a macroscopic cholesteric pitch and perhaps a macromolecular curl.

In this Chapter we present evidence that suggests that the details of both the internal and external virus structure contribute to the manifestation of the macroscopic cholesteric phase. We first present measurements of the cholesteric pitch of virus suspensions at different ionic strengths as a function of solution pH and viral surface charge configuration. By changing the pH of the solution we change the sur-

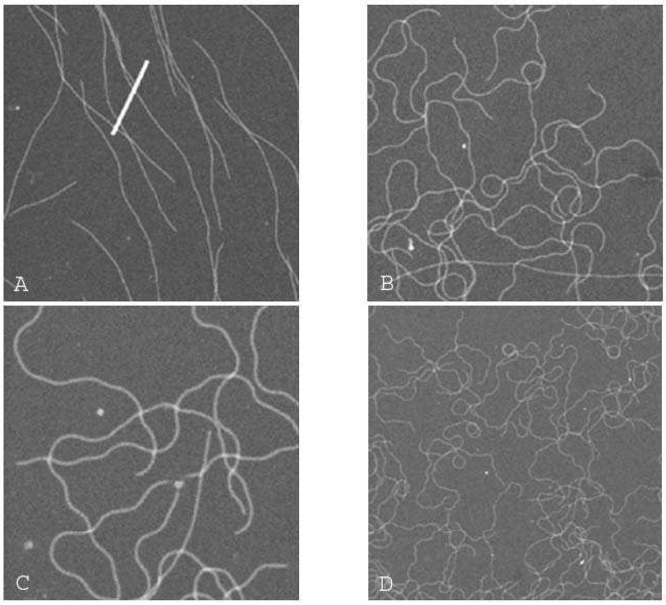

Figure 4.1: Scanning transmission electron micrographs of (A) semiflexible M13 and a single particle of tobacco mosaic virus (TMV), which is a rigid rod 300 nm in length and 18 nm in diameter. (B-D) show the curly X phage. Magnification in (B) is the same as in (A), whereas (C) is 2x higher and (D) is 2x lower than in (A). (Figures courtesy of L. Day and are from a collaboration of L. Day and J. Wall.)

face charge of either it fd or M13 virus. Similarly, by comparing the pitch of M13 and *fd* virus at constant pH and ionic strength we change the surface charge configuration of the virus by changing the virus type. Measurements of the cholesteric pitch using these two different techniques for changing the rod surface charge underline the role of surface charge on the macroscopic expression of chirality. Doping the viral DNA with silver ions, which bind strongly to the base pairs [67, 68], on the other hand, may be able to probe for the proposed macroscopic helicity. Additionally, the DNA and viral coat proteins have been shown to be rigidly linked [72], subsequently, changes in DNA configuration could be translated to changes in the whole virus structure. By measuring the cholesteric pitch as a function of the addition of silver ions into the viral DNA we test the sensitivity of the macroscopic chiral structure to changes in the microscopic structure of the viral DNA.

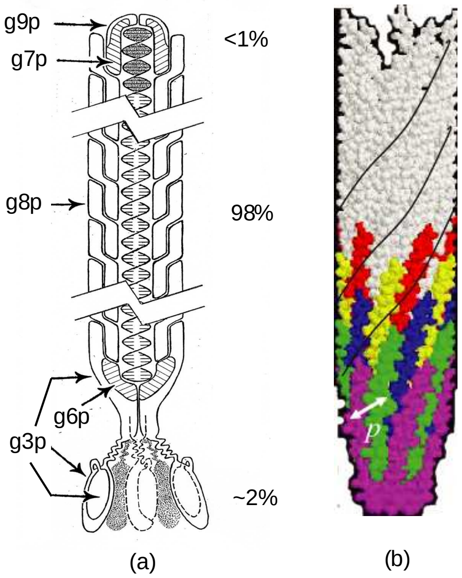

Figure 4.2: (a)Schematic of *fd* structure showing relative positions of the different viral coat proteins surrounding the single stranded viral DNA. (b) Schematic of the helical positioning of the p8 proteins about the viral DNA. The p8 proteins are arranged in two alternating layers of five-fold symmetry. The distance between adjacent subunits $p = 16$ Å. The black lines in (b) indicate the 160 Åhelical pitch of the coat proteins about the DNA. Image in (b) from [73].

4.2 Properties of the virus structure

The physical properties of M13 and *fd* are known [14] and include their length $L = 0.88$ μm diameter $D = 6.6$ nm, persistence length 2.2μm, and molecular weight 1.64×10^7 g/mol. The details of the helical protein structure, however, are of most interest in this Chapter. As mentioned above, the viral rods are composed of a single stranded DNA about which 2700 copies of its major coat protein, often referred to as g8p or p8 after the eighth gene which encodes the protein, are helicoidally wrapped in two layers of five-fold symmetry. Each of the layers is repeated along the long axis of the virus every 3.3 nm. This virus structure is illustrated schematically in Fig. 4.2. The helical pitch of the DNA within the virus is measured to be 2.7 nm [67]. The major coat protein (p8) (shown in Fig. 4.4 for *fd*) is responsible for both the viral surface charge and the charge neutralization of the DNA within the protein shell.

PHAGE	**AMINO ACID SEQUENCES OF MAJOR COAT PROTEIN SUBUNITS**	n/s **RATIO**	q_S/q_{DNA} **RATIO**
X2	- - - - + + ++ + EGTTTNTDYAGQAMTELLTQANDLIGKVWPVVVAVVGAALAIRLFKKFSSKAV	2.4	1.3
I2-2	-- - + - - + ++ + ADDGTSTATSYATEAMNSLKTQATDLIDQTWPVVTSVAVAGLAIRLFKKFSSKAV	2.2	1.4
IKe	- - - + - + ++ + AEPNAATNYATEAMDSLKTQAIDLISQTWPVVTTVVVAGLVIRLFKKFSSKAV	2.2	1.4
If1	-- + - - + ++ + ADDATSQAKAAFDSLTAQATEMSGYAWALVVLVVGATVGIKLFKKFVSRAS	2.4	1.3
Ff(fd,f1)	- -- + - - + ++ + AEGDDPAKAAFDSLQASATEYIGYAWAMVVVIVGATIGIKLFKKFTSKAS	2.4	1.3
M13	- -- + - + ++ + AEGDDPAKAAFNSLQASATEYIGYAWAMVVVIVGATIGIKLFKKFTSKAS	2.4	1.3
fd-K48T	- -- + - - + ++ AEGDDPAKAAFDSLQASATEYIGYAWAMVVVIVGATIGIKLFKKFTSTAS	~1.8	1.1
fs-2	- - - + ++ + AIPQEAQAALDAVGEFTSTVVGWMWGVGTAMIVGFVGLKVVKKGANKAT		
Pf1	- - - + ++ GVIDTSAVQSAITDGQGDMKAIGGYIVGALVILAVAGLIYSMLRKA	1.00	1
FXP	- - + - - + ++ EGGIAEAAGKALDSAQSDVTITAPKVMMVVATVVGVGILINMMRKA	(1)	(1)
Vf03K6,f237	- - ++ EVDITGAINSAVSGGQANVSLVVAGLIGMAALGFGVTMVVGFLRR	(1)	(1)
CTX (cholera)	- - + +- ++ + DAGLVTEVTKTLGTSKDTVIALGPLIMGVVGAIVLIVTVIGLIRKAK		
VSK	++ + + + MPLCKKFSLQSTLLVSLLSLLLLVLPSLASTWLSKASLSANALSTKPNR		
Yp01 (plague)	- - - + + + AEGAASSGVDLSPLTNSIDFSTVLVAIMAVAASLVTLYAGVAGVRWVLRTVKSA		
X	- - + - + + + AEGDVVGGKGIDLTPLTNSVNFGSVLTGIMAVAGSLIVLYAGSAGVRWILRMVRGA	1.9	1.05
C2	- - + + + MGPTAPTDIASLASSVDFSSVGLGILAIAGTVITLYVTWKGAQFVIRGVRGA	2.0	.5
Pf3	- - + + MQSVITDVTGQLTAVQADITTIGGAIIVLAAVVLGIRWIKAQFF	2.3-2.5	.4
Lf	- - + ++ MGDILTGVSGAEAATAMIAAAAIIALVGFTKWGAKKVASFFG		
fs-1(VGJ)	- - + ++ + MADIFGAIDFAGVAALVTAAGVSIIGITMAFKGISLGKRAVNKA		
VSKK	- + ++ + AIDFAGIAALVTAAGVAIIGINMAFKGITLGKRAVNKA		
Vf12,Vf33	- - - + + ++ + AEGGAADPFSAIDLSGVATKIGAAGLVIVGITMAYKSITLAKRAVNKA		
PH75	- - + ++ + MDFNPSEVASQVTNYIQAIAAAGVGVLALAIGLSAAWKYAKRFLKG	2.2-2.4	1.3
B5(Gm+)	- - + ++ + MLPMVILEAPSDVGGTVSAAITALGPQITPIIGVAIGVSLIPFAAKWIFRKAKSLVS		
Xf	- - + + ++ SGGGGVDVGDVVSAIQGAAGPIAAIGGAVLTVMVGIKVYKWVRRAM	2.0-2.2	1.4
Cf1c	- - + + + + -++ SGGGGDFDGTAIIGKVTTYTAIGVTILAPSRSVVGRFATRSDRRQVSQSAA		

Figure 4.3: Amino acid sequence of the major coat protein of several bacteriophages. C-terminal ends, which are closest to the DNA, are lined up on the right for comparisons with each other. The n/s ratio is calculated by dividing the number of nucleotides (n) by the number of protein subunits (s). The q_s/q_{DNA} ratio is calculated by dividing the charge of the protein subunit (q_s) by the number of negative charges from the phosphate backbone of the viral DNA per protein subunit(q_{DNA}). q_s is equal to the sum of positive amino acids and the negative terminal Carboxylate ($q = -1$ for pH>pKa=3.4), and q_{DNA} is equivalent to n/s. Most of the sequences are available in Genbank (sequences provided by L. Day.)

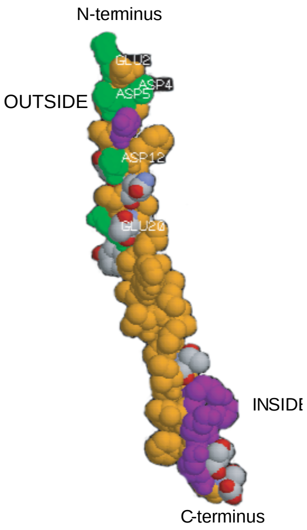

Figure 4.4: (color online) Structure of major coat protein (p8) for *fd* virus. The protein is oriented such that the observer is looking at the protein from the inside of the virus. The negative amino acids are labeled and are colored green and the positively charged amino acids are colored purple. Charges are for neutral pH. The hydrophobic amino acids are colored orange. Image created using RasMol software from protein data base structure 1IFI [33].

In Fig. 4.3 we present a representative list of the major coat protein structures for many phage particles. For all the phage proteins listed there is consistently a large sequence of amino acid residues which are neutral separating the external charged residues from the internal charged residues. Measurements of the titration curves of *fd* and Pf1 indicate that the amino acid residues which are exposed to the surface are responsible for the viral surface charge [34]. The residues which are located on the interior of the virus are therefore responsible for charge neutralization of the viral DNA. From Fig. 4.3 we can identify approximately three types of protein-DNA charge interactions. For charge neutralization we expect the ratio $q_s/q_{DNA} = 1$, where the positive charges from the amino acid residues on each protein subunit (q_s) are equalized by the negative charges from the phosphate backbone of the DNA $q_{DNA} = 1e^-$/nucleotide. For most of the phages, however, the charge of the interior of the coat protein (C-terminus) is slightly larger than the charge of the DNA from the phosphate backbone, or $q_s/q_{DNA} \gtrsim 1$. Phage with this q_s/q_{DNA} ratio include *fd* and M13. For *fd* it is believed that q_s/q_{DNA} is actually one; the remaining negative charge required for neutralization may come from the slight negativity of the Thymine and Guanine nucleosides (pKa=9.2, negative at high pH, neutral at low pH) [34]. However the amount of negative charge from the nucleosides is fairly small, as most of our experiments are at a pH much lower than 9.2. If the charge is not neutralized within the *fd* particles it is possible that there will be some internal stress which we suggest may effect the macromolecular shape of the virus.

For a few phages including Pf1, the phosphate backbone charges are completely neutralized by the positive amino acids on the coat proteins, and for C2 and Pf3, there are not enough charged amino acids to neutralize the DNA, $q_s/q_{DNA} < 1$. Charge neutralization within the virus particles is what allows the particles to maintain their stability. The phage fd-K48T, for example, differs from *fd* only by the replacement of the neutral T_{48} for the positively charged K_{48} in *fd*. In order to maintain charge neutrality within the virus core, *fd*-K48T grows to be 35% longer than the wild type *fd* even though the enclosed DNA is the same length [74]. Presumably this is because 35% more p8 proteins were needed to neutralize the negatively charged DNA.

We mention the three types of charge ratios because these protein/DNA interactions seem to correlate to the structure of the DNA within the phage, and to the presence/absence of a cholesteric phase. First, it is well known that *fd*, which may have a net positive charge internally, exhibits a well defined cholesteric phase [65]. The *fd* phage is also known to exhibit a DNA structure oriented such that the charged phosphate backbone is near the coat proteins ("inside-in"). Pf1, which is stoichiometrically neutral inside, however does not exhibit a cholesteric phase. It, furthermore, has a different DNA structure where the phosphate backbone is oriented towards the inside of the DNA ("inside-out"). Additionally, new studies by S. Tomar and L. Day have shown that Pf3 also exhibits a cholesteric phase [75]. The DNA structure of Pf3 is also inside-out, but the structure contains a large hole in the center of the

DNA which allows for the addition of metal cations into the virus interior [66]. These metal cations relieve the positive charge deficit and help to neutralize the interior of the phage. Qualitatively, there perhaps is a correlation between the difference in the DNA structure and the presence of a cholesteric phase. We mention this correlation to emphasize the plausibility of a link between the chiral DNA structure, chiral virus structure, and the cholesteric pitch, which we will test in one way in this Chapter.

The composition of the major coat protein (p8) on M13 differs from that of *fd* by only one amino acid. The negatively charged aspartate (asp_{12}) in *fd* is substituted for the neutral asparagine (asn_{12}) in M13 [33]. The single amino acid difference between M13 and *fd* has a minimal effect on the virus structure, as determined previously by x-ray diffraction [76]. But the difference has a significant effect on surface charge. The *fd* virus p8 protein has 5 negatively ionizable amino acids and one positively ionizable amino acid which are exposed to the virus surface. These amino acids and the terminal amine, which contributes approximately 1/2 e^+ at neutral pH, are the only amino acids on the p8 protein responsible for the net viral surface charge as a function of pH. At pH 7.2 the surface charge of *fd* is approximately $3.5e^-$/protien subunit [34]. M13, correspondingly, has a surface charge of about $2.5e^-$/protein subunit at neutral pH. The two particles have a total charge difference of approximately 30%. Additionally, the net surface charge of both virus particles can be altered by changing the solution pH; for *fd* the viral pKa is approximately 3 [34].

4.3 Sample Preparation

The M13 and *fd* bacteriophages were prepared and purified from bacterial solutions as previously described [36]. To study the role of surface charge on the cholesteric pitch, samples were prepared at either pH 8.2 using a 20 mM Tris-HCl buffer or at pH 5.2 using 20 mM Sodium Acetate buffer adjusted with Acetic acid. At pH 8.2 *fd* has a surface charge of 10 e^-/nm and M13 has a surface charge of 7 e^-/nm. At pH 5.2 the surface charges are 7 e^-/nm and 3.6 e^-/nm, respectively. The surface charge was determined by titration experiments (*fd*) [34], and by whole virus gel electrophoresis (M13) as described in Chapter 2, Fig. 2.2. Ionic strength (I) was adjusted by adding NaCl.

To study the effect of the viral DNA structure on the macroscopic cholesteric pitch, *fd* suspensions were dialyzed against a 150 mM $NaHBO_3$ (Boric Acid) buffer at pH 8.6. The ionic strength of the buffering solution was calculated to be 30 mM. Quantities of $AgNO_3$ were added in $m = 0$, $m = 0.5$ and $m = 1$ quantities, where m is the molar concentration of DNA nucleotides (0.26 mg/ml *fd*=0.031 mg/ml DNA=0.1 mM nucleotides). The monovalent silver ion, Ag^+, diffuses freely through the viral coat protein and binds with the DNA within the virus [67, 68]. The silver ions have a very high affinity for the amines (N) in the nucleotides and have been shown to complex with the base pairs at these amines in place of the hydrogen-bonding. This strong binding site accounts for the binding of silver ions up to $m = 0.5$. For silver concentrations above $m = 0.5$ the remaining binding sites are weaker. The complexing of the silver to the nucleotides is also completely reversible by the addition of NaCl to the solution. After the silver is allowed to diffuse into the virus, the virus solution is centrifuged at ∼200 000 g to pellet the virus. The virus pellet is then resuspended in 150 mM Borate buffer. This helps to assure that any unreacted Ag^+ or NO_3^- are removed from the solution and do not contribute to the ionic strength of the solution. Disassociation of the silver from the DNA after centrifugation is predicted to be minimal [75].

Typically *fd* concentration is measured via absorption spectrophotometry at 269 nm, optical density $OD_{269\text{nm}}^{3.84\text{ml/mg}}$ for a sample 1 cm thick, however, the silver cations alter the absorption spectra of the virus particles. To determine the *fd* concentration in the presence of silver cations, the absorption was measured instead at

260 nm where absorption is independent of silver concentration [67]. The OD at 260 nm was determined to be $OD^{3.49\text{ml/mg}}_{260\text{nm}}$, again for a 1 cm sample, from the equation $OD_{260} = OD_{269} * A_{260}/A_{269}$ using a silver-free sample of *fd*. To confirm the concentration of the silver intercalated within the virus the difference between the actual absorption at 269 nm and the predicted absorption at 269 nm as calculated from the absorption at 260 nm, or $A_{269} - A_{260} * 3.84/3.49$, was first calculated. This difference was plotted as a function of *fd* concentration to approximate the absorption due to silver at $c_{fd} = 0.238$ mg/ml which has been measured previously [67]. The values of m determined from absorption measurements agreed with the amount of silver added initially to the solution. Typically, any silver excluded from within the virus particles is removed from solution before the silver concentration is measured. Consequently we assume that there are no extra silver ions in solution and that the absorption change measured is due only to intercalated silver ions.

In all instances samples of different virus concentrations and different buffering solutions were added to 0.7μm diameter glass capillaries (Charles Supper Co.), gently centrifuged to pull the sample to one end of the capillary, sealed within the glass, and then allowed to equilibrate for more than three days. After equilibration the samples were observed microscopically under crossed polarizers. From the "fingerprint" texture characteristic of cholesteric phases, measurements of the cholesteric pitch were made, as illustrated in Fig. 4.5. The pitch P of the cholesteric phase is defined by the distance between rods of the same orientation rotated by 360^o. Under crossed polarizers the length of the cholesteric pitch spans two bright and two dark lines, regions where the rods are parallel, or perpendicular to the plane of observation, respectively, as indicated in the Fig.4.5. The pitch was measured in multiple locations throughout the sample to get a measure of the variability.

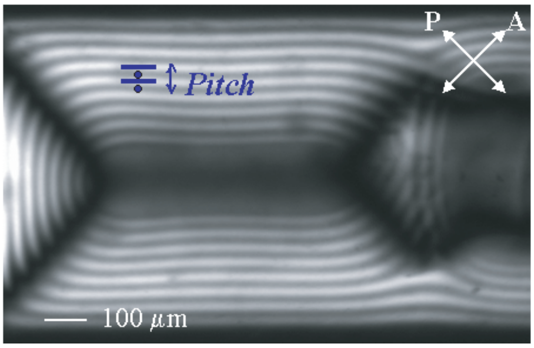

Figure 4.5: “Fingerprint” texture of a cholesteric phase of *fd* virus, as observed by optical microscopy between crossed polarizers after a few days of equilibration following the preparation of the sample. Picture was taken of a sample contained in a cylindrical capillary, where planar anchoring of the liquid crystal to the glass surface occurs. Dark lines correspond to regions where the rods are perpendicular to the plane of observation and bright lines correspond to regions where rods are in the observation plane.

4.4 Results

4.4.1 The cholesteric pitch of M13 and *fd* suspensions as a function of ionic strength

To study the surface charge dependence of the cholesteric pitch we first measured the variation of the cholesteric pitch of M13 virus suspensions with concentration and ionic strength at pH 8.2 and compared it to similar measurements made previously for *fd* suspensions [35]. These measurements are presented Fig. 4.6. At a constant concentration, both M13 and *fd* exhibit increasing values of the cholesteric pitch with increasing ionic strength. Motivated by previous theories [77, 78], the evolution of the pitch of the cholesteric phase with concentration was fit to the form $P = a + c^{-b}$, where P is the measured pitch and c is the concentration. Surprisingly, M13 exhibits the same scaling exponent b≈1.4 independent of ionic strength, while *fd* exhibits a scaling exponent which increases with increasing ionic strength, b = 1.5 to 1.8 [35]. Furthermore, because b remains constant we can measure the increase in pitch with increasing ionic strength to be $P \propto a_{fit} \propto I^{0.3}$.

The measured values of the pitch are close to previous theories for semiflexible hard rods with a threaded screw-like structure where the exponent was predicted to be 1.66 [77] and 2.0 [78]. However these theories do not predict the strong ionic strength (and in the following section, surface charge) dependence observed. The increase in pitch with ionic strength can be qualitatively understood by a straightforward electrostatics argument. First, we have shown with x-ray scattering experiments that the interparticle distance (d_{inter}) is roughly independent of ionic strength in the cholesteric (nematic) range [42]. Second, electrostatic interactions, and therefore D_{eff} decrease with increasing ionic strength. Third, charged rods have a lower energy when they are perpendicular to each rather than when they are parallel; this electrostatic twisting increases with increasing electrostatic interactions. Therefore at a given concentration of virus i.e. at a given interparticle distance d_{inter}, the cholesteric angle between adjacent rods tends to decrease with increasing ionic strength, subsequently increasing the pitch as observed in Fig 4.6.

Why does the scaling exponent of the concentration dependence of the cholesteric pitch vary with ionic strength for *fd* suspensions but remain constant for M13 suspensions? M13 and *fd* differ only by their surface charge. It is possible that this surface charge difference is responsible for the difference in ionic strength dependence of the cholesteric pitch, however, the results presented in the following section indicate that the cause of this strange difference between M13 and *fd* pitch is more subtle. We will discuss the implications of these results further in the following two sections.

4.4.2 The cholesteric pitch of M13 and *fd* suspensions as a function of solution pH

To systematically investigate the relationship between the viral surface charge and the cholesteric pitch we measured the concentration dependence of the pitch of M13 and *fd* suspensions as a function of pH. Decreasing the pH of the virus solution decreases

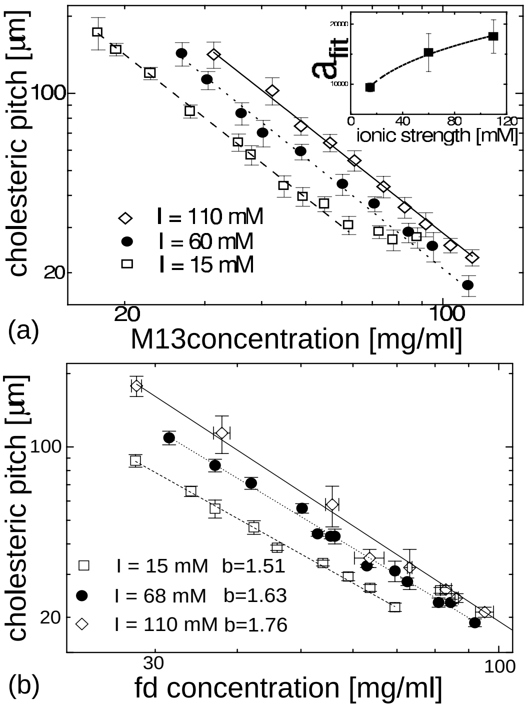

Figure 4.6: Concentration dependence of cholesteric pitch of suspensions of (a) M13 and (b) *fd* for (◇)110 mM, (•) 60 mM, and (□) 15 mM ionic strength pH 8.2. For M13 $b = -1.4$ for all ionic strengths. The inset in (a) displays the coefficient a for M13 suspensions, which increases with ionic strength.

the viral surface charge [34]. In Fig. 4.7 we plot the cholesteric pitch for M13 and *fd* suspensions measured at pH 8.2 and pH 5.2 at low and high ionic strength. The pH dependence of the pitch of M13 suspensions at high ionic strength is not presented because at pH 5.2 the samples appeared completely nematic, implying the pitch was larger than measurable in the 0.7 mm capillaries. With decreasing pH (decreasing surface charge), the cholesteric pitch of both M13 and *fd* suspensions increases (a increases). Additionally, the scaling exponent b is roughly independent of pH (independent of surface charge) for both M13 and *fd* suspension. These measurements show that the cholesteric pitch, depends on both the pH (viral surface charge) and ionic strength of the solution.

The results in Fig. 4.7 provide us with some interesting insight into the correlation between electrostatic interactions and cholesteric pitch. First, the strong pH dependence of the pitch indicates that subtle changes in electrostatic repulsion created by changing viral surface charge have a large effect on macroscopic chiral properties. Recall that for highly charged particles, like these viruses, the electrostatic interactions, typically described by D_{eff}, are predicted to be insensitive to surface charge differences due to condensation of the virus counterions and subsequent effective surface charge renormalization [58]. This insensitivity to surface charge is apparent in the properties of the isotropic-cholesteric phase transition which is well described by the charge independent D_{eff}, as presented in Chapter 2 (see for example Figs. 2.7 and 2.9). However, even near the isotropic-cholesteric transition, the cholesteric pitch can differ by up to 40% between samples at pH 5.2 and at pH 8.2. Due to the inherent twisting nature of the cholesteric phase, small changes in electrostatic repulsion between adjacent rods as a result of a change in surface charge, creates small changes in the nearest-neighbor twisting. These small changes are amplified over many rods spanning the length of the cholesteric pitch resulting in a measurable change in the cholesteric pitch. Subsequently, the cholesteric pitch is highly susceptible to small

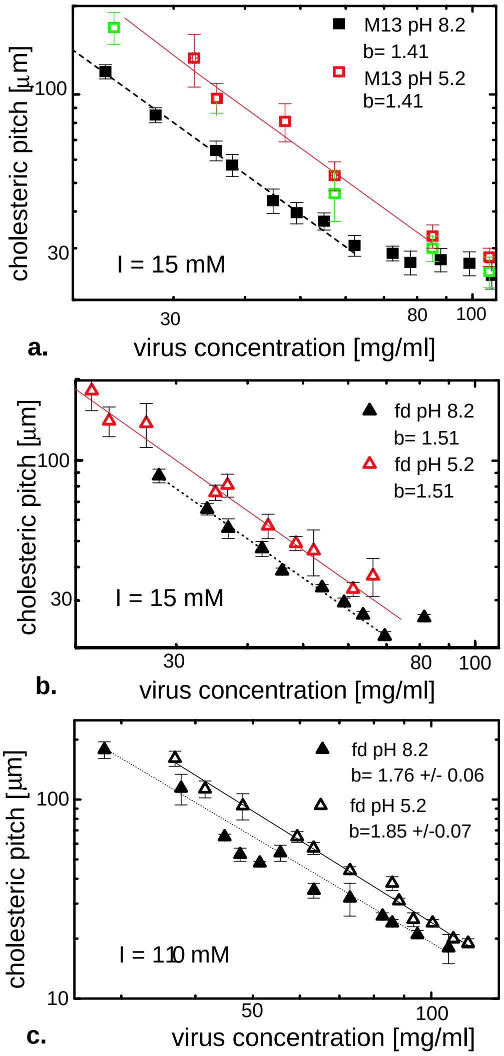

Figure 4.7: Concentration dependence of cholesteric pitch at pH 8.2 and 5.2 for (a) M13 at 15 mM ionic strength, (b) *fd* at 15 mM ionic strength and (c) *fd* at 110 mM ionic strength. At pH 8.2 the virus is in a Tris-HCl buffer, and at pH 5.2 the virus is in a Sodium-Acetate, Acetic Acid buffer. At pH 8.2 M13 has a surface charge of 7 e^{-}/nm and *fd* has a surface charge of 10 e^{-}/nm. At pH 5.2 M13 has a surface charge of 4 e^{-}/nm and *fd* has a surface charge of 7 e^{-}/nm. At pH 5.2 and 110 mM ionic strength M13 has a pitch larger than the capillary size (0.7 mm) for all concentrations and the suspension appears nematic.

changes in surface charge. An increase in pH, which increases the surface charge, increases electrostatic repulsion resulting in a smaller pitch as measured.

Second, the results in Fig. 4.7 indicate that it may be possible to separate the ionic strength and surface charge dependence of the cholesteric pitch. Specifically, at a constant ionic strength, decreasing pH increases the coefficient a in the equation $P = ac^{-b}$. Similarly, independent of pH, ionic strength alone determines the scaling exponent b. This suggests that the two chiral interparticle interactions which contribute to the formation of the cholesteric pitch, the intrinsic chiral structure of the rod, and the electrostatic twist h act independently. As h depends predominantly on ionic strength, and only weakly depends on surface charge, we can deduce that the ionic strength dependence of b is influenced predominantly by electrostatic twisting. This agrees with the measurements for both *fd* and M13, but the ionic strength independence of b for M13 suspensions is still not explained by this relationship. Also, this suggests that changes in the microscopic chiral structure of the rods, caused by changing the solution pH, influence the macroscopic pitch (by shifting a). This is plausible as changing pH indeed changes the microscopic chiral structure by changing configuration of charges on the surface of the virus.

Third, the observation of a nematic phase in M13 suspensions at high ionic strength and low pH suggests that strong electrostatic interactions between the helical virus rods are required for the realization of a macroscopic cholesteric pitch. We note that experimentally this is the condition of smallest electrostatic interactions. This is somewhat contradictory to the previously mentioned recent measurements of the cholesteric pitch of *fd* coated with polymer [38] which exhibit a cholesteric phase even at 100 mM ionic strength, even though their isotropic-nematic phase transition is independent of ionic strength (independent of electrostatic interactions). These two results suggest that the electrostatic interactions from the surface charge of the polymer coated *fd* (10e$^-$/nm) is somehow strong enough to induce macroscopic chiral structure even in the presence of a sterically stabilizing polymer coating, but are not strong enough to form a cholesteric phase for M13 at low pH.

4.4.3 Comparison of M13 and *fd* suspension measurements

In the previous section we found that by changing the viral surface charge via the solution pH, the cholesteric pitch shifted by a constant amount (a changed, b remained constant), independent of virus concentration. We now present the surface charge dependence of the cholesteric pitch as measured by comparing M13 (7e^{-}/nm) to *fd* (10 e^{-}/nm) at pH 8.2 as a function of concentration and ionic strength. In Fig. 4.8 we compare measurements of the pitch of M13 and *fd* suspensions for three different ionic strengths. Immediately we see that the change in the cholesteric pitch as a function of surface charge depends on the virus concentration, in contrast to the pH measurements. Specifically, at low concentrations the M13 and *fd* suspensions have very similar values for the pitch. This is consistent with the agreement between M13 and *fd* coexistence concentrations (Chapter 2). However, with increasing concentration, the disagreement between M13 and *fd* measurements increases significantly, particularly at high ionic strength. The increasing difference between M13 and *fd* measurements originates from the difference in scaling exponents ($b = 1.5 - 1.8$ for *fd* and $b = 1.4$ for M13). We note that the pitch of the *fd* suspensions is consistently smaller than the pitch of the M13 suspensions at high concentrations, which is consistent with the *fd* having a higher surface charge. Whereas the agreement between *fd* and M13 measurements at low concentration suggests charge insensitivity, the disagreement of the pitch measurements at high concentrations suggests the opposite.

Because the charge dependence of the cholesteric pitch as measured in Fig. 4.8 differs quite significantly from the charge dependence measured as a function of pH (Fig. 4.7) we hypothesize that there is another variable which is causing the difference. To further investigate the conflicting measurements of the charge dependence of the

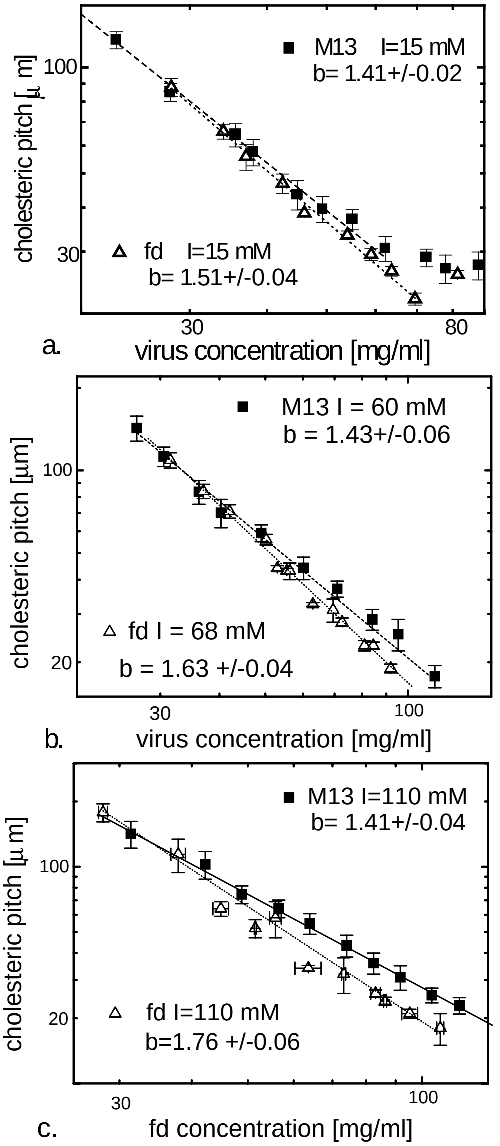

Figure 4.8: Concentration dependence of cholesteric pitch of (■) M13 and (△) *fd* at (a) 15 mM, (b) 60 mM, and (c) 110 mM ionic strength pH 8.2. Data for *fd* at 15 mM and 68 mM are taken from Ref. [35].

cholesteric pitch we compare the cholesteric pitch measurements from M13 and *fd* suspensions when both virus have the same surface charge. In Fig. 4.9 both M13 (pH 8.2) and *fd* (pH 5.2) have a measured surface charge of 7 e^-/nm. Surprisingly, M13 and *fd* have measurably different values of the cholesteric pitch at both 15 mM and 110 mM ionic strength even though they have the same surface charge. As M13 and *fd* only differ by their surface charge configuration we propose that it is indeed this subtle structural difference between the two viruses which leads to the different cholesteric behavior. This structural difference could also explain why the scaling exponent b changes with ionic strength for *fd*, but remains constant for M13 as illustrated in Fig. 4.8. Similar surprising results are observed in measurements of the nematic-smectic phase transition of M13 and *fd* suspensions where both M13 and *fd* had a surface charge of 7e^-/nm and yet their phase transition concentrations were measurably different, as shown in Chapter 3. Observing a difference in cholesteric pitch behavior between M13 and *fd* suspensions strengthens the theoretical suggestion that the surface charge configuration directly influences the macroscopic expression of chirality [69].

4.4.4 Measurements of the cholesteric pitch as a function of DNA/coat-protein interactions

In Fig. 4.10 we present measurements of the cholesteric pitch of *fd* as a function of concentration with silver ions added at concentrations of $m = 0, m = 0.5$ and $m = 1$. Recall that the silver ions are thought to intercalate between the single stranded DNA base pairs within the virus particles [67, 68]. Approximately one silver molecule will form a bridge between two nucleic acids on opposing strands, and as mentioned previously, we assume there is no extra silver in solution. This is confirmed by the measurement of an isotropic-cholesteric phase transition concentration which is independent of m. Free ions would alter the solution ionic strength and subsequently

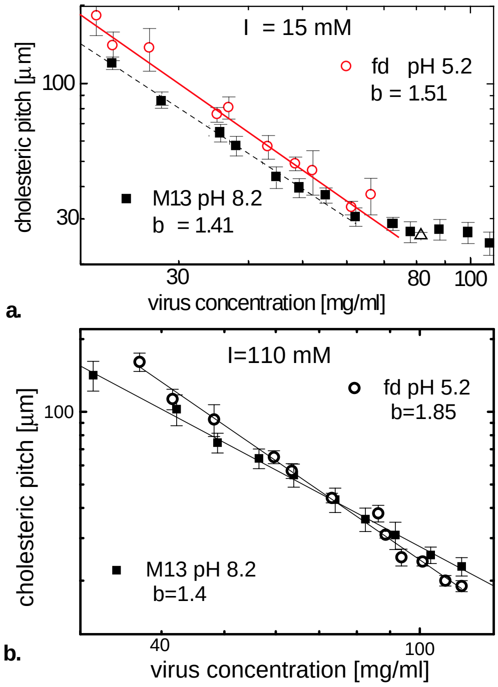

Figure 4.9: Concentration dependence of cholesteric pitch of (■) M13 and (○) *fd* at (a) 15 mM and (b) 110 mM ionic strength. M13 is at pH8.2 in a Tris-HCl buffer, and *fd* is at pH 5.2 in a Sodium-Acetate Acetic Acid buffer. Both M13 and *fd* have a surface charge of 7e$^-$/nm.

shift the isotropic-cholesteric phase transition concentration (or the cholesteric pitch). Even with large variation of the pitch within each sample (large error bars), we observe in Fig. 4.10 that the intercalation of the silver and subsequent bridging between the DNA strands increases the cholesteric pitch, particularly at $m = 1$. The scaling exponent of the pitch with concentration also increases with increasing silver ions. A further confirmation that the silver ions are not in solution is that the change in pitch at constant concentration due to adding $AgNO_3$ is much larger than the corresponding change in pitch with added NaCl at the same concentration (and smaller increase in ionic strength). For example, at 30 mg/ml adding $m = 1$ $AgNO_3$ (8 mM) increases the pitch by 60 μm, whereas adding 40 mM NaCl increases the pitch by only 35 μm. At high concentrations, the cholesteric pitch becomes independent of concentration due to pre-smectic unwinding of the pitch [65]at some minimum value which increases with increasing m.

We have previously proposed that these chiral viruses have a macromolecular helicity associated with them. One possible explanation for the measured change in the cholesteric pitch with the addition of silver ions is that the *fd* rods are changing their helical properties. This change in helical properties would arise from a change in viral DNA configuration due to the intercalation of the silver ions into single stranded DNA. Because the DNA and viral coat proteins are rigidly coupled [72], changes in DNA configuration could be translated to changes in the whole virus structure. We note that the addition of silver to single stranded DNA solutions has been shown to have only a small effect on the DNA configuration [68]. This is also true for the virus configuration [68]. However, as mentioned before, small changes in the interactions between adjacent particles can be amplified over many rods in the cholesteric phase, resulting in measurable pitch differences.

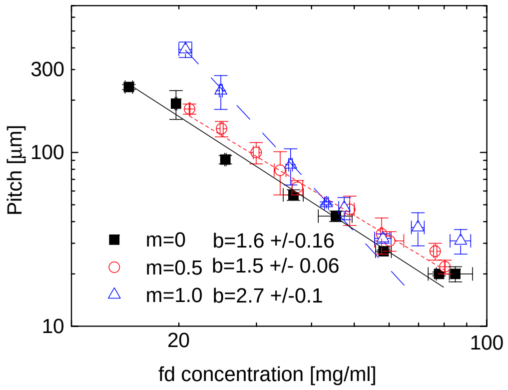

Figure 4.10: Concentration dependence of cholesteric pitch of suspensions *fd* in the presence of silver, Ag^+ in 150 mM Borate buffer at pH 7.2 (I= 30 mM). Black squares are at $m = 0$, Red circles at $m = 0.5$ and Blue triangles at $m = 1$. m is the number of moles of silver ion per moles of nucleotides. Intercalation of the silver ions between base pairs in the DNA within the virus causes slight relaxation of the pitch.

4.5 Discussion

The measurements of the pitch of M13 and *fd* suspensions as a function of pH, ionic strength and intercalated silver ions present us with many surprising results. We can conclude with reasonable confidence that the chirality of the nematic phase, as shown in the cholesteric pitch, is strongly coupled to both the ionic strength of the solution and surface charge of the rods. In fact, the scaling exponent b in the relationship between pitch and virus concentration $P = ac^{-b}$, depends only on the ionic strength of the solution for *fd* suspensions (Fig. 4.7). Additionally, because of the coupling of nearest-neighbor interactions in the cholesteric phase, we find that the cholesteric pitch is extremely sensitive to differences in viral surface charge (Fig. 4.7 and Fig. 4.8) even in a regime where the surface charge is predicted to be well screened by counterion condensation and added salt ions. For both *fd* and M13, the offset a of the pitch curve depends strongly on the pH of the solution (viral surface charge), at a constant ionic strength (Fig. 4.7). Oddly, M13 has a scaling exponent b which is independent of ionic strength (Fig. 4.6). As a result, M13 and *fd* exhibit different phase behavior, even when they are known to have the same surface charge: *fd* at pH

5.2 and M13 at pH 8.2 (Fig. 4.9). This difference in cholesteric pitch between *fd* and M13 suggests that perhaps the cholesteric pitch is quite sensitive to the viral surface charge configuration, in agreement with theoretical predictions [69]. This is in strong contrast to the surface charge independent measurements of the isotropic-cholesteric coexistence concentrations (Chapter 2).

The appearance of a nematic phase in M13 suspensions in the limit of low pH and high ionic strength suggests that there is a transition from a cholesteric phase to a nematic phase for rods with small interparticle electrostatic interactions. It has been suggested that *fd* and M13 have some macroscopic "corkscrew" like curling associated with them which allows the chiral information of the virus to be incorporated, even through a polymer layer [38], into the interparticle interactions. The lack of a cholesteric pitch for M13 at low pH and high electrostatic screening suggests that perhaps this curling, if it is real, depends on electrostatics. Measurements of the pitch of M13 suspensions at low pH for intermediate values of the ionic strength would more clearly determine whether the M13 suspensions are indeed nematic or just have a very large pitch. Furthermore, measurements of the pitch of polymer coated *fd* and M13 as a function of pH would help to determine the role of electrostatics versus the proposed curling in the pitch of polymer coated rods.

Finally, the change in cholesteric pitch due to the intercalation of silver ions within the *fd* virus DNA confirms the intrinsic coupling between the DNA and the coat proteins which in turn influences the cholesteric phase, perhaps via the proposed curling mechanism. Comparisons of these results to measurements of the pitch of other phages with known macroscopic helicity, like X phage (Fig. 4.1) [71], under similar conditions of added silver ions should reveal more about the relationship between the internal chirality of the virus and the transmission of that chirality to the bulk nematic phase. Similarly studying the cholesteric phase of mutants of the *fd* virus which have altered DNA/protein interactions, obtained by mutation of amino acid residues near the C-terminal from positive to neutral and vice-versa, can provide further insight into the relationship between the DNA-coat protein interactions and the chirality of the cholesteric phase. Finally, we suggest measurements of M13 suspensions in the presence of the silver ion to determine if the difference between M13 and *fd* cholesterics is related to their internal structure.

Chapter 5

Measurements of the orientational distribution function of the nematic phase of *fd*virus suspensions via x-ray diffraction

5.1 Introduction

In Chapter 1, we described the theory developed by Onsager describing the free energy of a system of hard-rods at the second virial level. All theoretical predictions for the properties of this phase transition, such as the coexistence concentrations and the nematic order parameter, depend on the functional form of the orientational distribution of the rods in the nematic phase [1]. Onsager chose one test function and in a later review paper Odijk showed that qualitatively similar results for the properties of the phase transition can be found by choosing a Gaussian test function [21]. The exact form of the orientational distribution function that satisfies the Onsager theory can be obtained via series expansion [79, 41, 7] or by direct iterative methods

[15, 80]. But experimentally determining the orientational distribution function of the nematic phase of a colloidal rod system is the most sensitive test of whether a system is described by Onsager's theory.

In this chapter we present measurements of the orientational distribution function and nematic order parameter of *fd*virus via x-ray diffraction. We explore the behavior of the nematic phase of *fd*virus, investigating the concentration and ionic strength dependance of the spatial and orientational ordering measured from both interparticle and intraparticle diffraction data. We present measurements of the orientational ordering of the nematic phase in coexistence with the isotropic phase as a function of ionic strength and compare the results with the predictions for semiflexible rods. Previously, measurements of the orientational distribution function of a nematic phase have been made either from form factor scatter as in work done by Oldenbourg *et. al.* on TMV [81] and work done by Groot *et. al.* and Kassapidou *et. al.* on persistence lengthed DNA fragments [82, 83] or from structure factor scatter as in work done by Davidson *et. al.* [84]. Using *fd*as our model rod allows us to measure the orientational distribution function from both intraparticle scattering and interparticle interference scattering. This permits us to experimentally resolve the question of whether or not correlations between angular and spatial order present in interparticle scatter influence the measurement of the order parameter. By measuring the birefringence of each sample we also determined the saturation birefringence of fd. This permits measurements of the order parameter to be made using birefringence methods, which involve much simpler and inexpensive techniques than x-ray diffraction.

This Chapter is organized in the following manner. In section 5.2 we describe the virus system and the experimental methods. In section 5.3 qualitative observations about the diffraction data are made. This is followed by an extensive description of the analysis technique used to extract the measured orientational distribution function from the x-ray diffraction data in section 5.4. Quantitative measurements of the nematic spatial ordering and orientational ordering are presented in section 5.5. This section includes first a subsection describing the measured spatial ordering and then subsections presenting the measured orientational distribution function and the order parameter of the nematic suspensions of fd. Section 5.6 summarizes the significant results of this paper.

5.2 Materials and Methods

The *fd*virus was prepared using standard biological protocols found in Ref. [36] and described in detail in Appendix A. The purified virus was extensively dialyzed against a 20 mM Tris-HCl buffer at pH 8.2 and the ionic strength was adjusted by adding NaCl. To observe the effect of charge on the nematic phase, samples were prepared at different concentrations and ionic strengths. The *fd* concentration was measured with a UV spectrometer by absorption at 269 nm with an absorption coefficient of 3.84 cm^2 mg^{-1}.

X-ray diffraction was done at the SAXS station on beamline 8-ID at the Advanced Photon Source at Argonne National Lab. The beam flux is 2×10^{10} photons/s for a $50 \times 50\mu$m beam with a photon energy of 7.664 KeV (λ=1.617 Å). The samples were a suspension of monodisperse *fd* in the cholesteric phase, sealed in ~ 0.7 mm diameter quartz x-ray capillaries. Cholesteric samples were unwound and aligned in a 2 T permanent magnet (SAM-2 Hummingbird Instruments, Arlington, MA 02474)[48], forming a single domain nematic phase parallel to the long axis of the capillary and the magnetic field, which we will call $\hat{z}$. The free energy difference between the cholesteric and nematic phases is negligible, and the theory of the phase behavior of the isotropic to nematic transition can be applied equally well to the isotropic to cholesteric transition observed in *fd* [30]. The magnetic field does not have a significant effect on the ordering of the nematic phase [49, 39, 50]. Samples had to remain in the magnetic field for a minimum of 15 minutes at low concentrations and a maximum of about 8 hours at the highest concentrations. The strength of the magnetic field limited the maximum concentration at which we could unwind the cholesteric phase into a mono-domain nematic to about 100 mg/ml [65].

To view the liquid crystal with a polarizing microscope, samples were placed in an index matching water bath to correct optical distortions produced by the cylindrical capillary. This was done while the samples were within the magnet in order to maintain the sample as a mono-domain nematic. Alignment of the nematic sample was checked with the polarizing microscope, and using a 3λ Berek compensator, its optical retardance was measured. By measuring the optical retardance R and the sample thickness within the capillary d we can calculate the sample birefringence $\Delta n = R/d$. Birefringence is measured because it is a simple way to determine the nematic ordering of a sample as it is equal to the nematic order parameter S times a constant Δn_{sat} intrinsic to the sample material [85]. In this system, Δn_{sat} is the saturation birefringence of perfectly aligned fd, the value of which we have measured and report in section 5.5. Details of the origin of the birefringence of anisotropic particles are outlined in appendix 5.7. The magnet and sample were then mounted in a vacuum chamber such that the sample was in the beam line, and the magnetic field was perpendicular to the incoming beam.

When the solutions of *fd* were exposed to x-rays for extended time, disclination lines that matched the pattern traced by the beam could be seen with a polarizing microscope. Since our samples were exposed for varied times, a series of x-ray diffraction patterns from the samples were collected with increasing x-ray exposure time to quantify sample damage and its effects on the scattering pattern. The polarizing microscope revealed sample changes after ~ 6 s of exposure, but the angular spread of the diffraction peaks was not affected until exposure times increased above 10 s, at which point the angular interference peak scatter broadened significantly. The effect of exposure for < 10 s on the calculation of the order parameter was not measurable. Data was collected for the interparticle interference scatter by averaging ten 10 s exposures taken at different $50 \times 50\mu$m sections. To observe the much less intense intraparticle scatter, the sample was continuously moved through the $50 \times 50\mu$m beam allowing for a total exposure of 120 s. A single long exposure was used to image intraparticle scatter as it resulted in less noise than multiple short exposures because readout noise on the CCD was higher than the dark current. Readout noise and solvent scatter were subtracted from data images during analysis, but over the q-range which was analyzed this background scatter was very uniform and could be approximated as a constant.

5.3 Observations

The two dimensional scattered intensity of low angle interparticle and high angle intraparticle interference peaks are shown in Fig. 5.1 for concentrations spanning the range over which *fd*is nematic at 10 mM ionic strength. The angular spread of both types of scatter broadens with decreasing *fd*concentration or increasing ionic strength, corresponding to an increase in disorientation of the rods. The low angle structure factor peak exhibits a typical “bow-tie” pattern as shown in Fig. 5.1a, characteristic of interparticle interference [86]. The maximum of the scattering vector q_r of this intense structure factor peak is inversely proportional to the average interparticle separation, and the radial width of the peak is inversely proportional to the correlation length of the interacting rods. We note briefly that the observation of a structure factor peak in our system of *fd*and in other lyotropic liquid crystal systems [82, 81, 84] contradicts theoretical predictions by van der Schoot and coworkers which predict that the angular dispersion of nematic rods should destroy spatial order [87, 88].

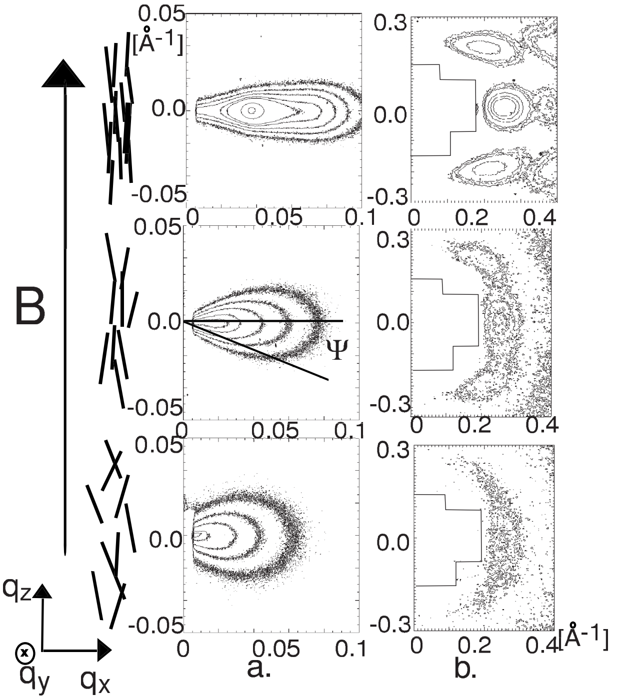

Figure 5.1: Contour plots of scattering as a function of scattering vector $\vec{q}[\text{Å}^{-1}]$ from nematic *fd*due to (a) interparticle scatter and (b) intraparticle scatter; the zeroth and ±first layer lines are shown in (b). The interparticle scatter shown in (a) is hidden behind the beamstop in (b) which is located on the left side of the images. From top to bottom the concentration of the samples are 93 mg/ml, 33 mg/ml, and 15.5 mg/ml. Samples shown are at an ionic strength of 10 mM (20mM Tris buffer), pH 8.2. The magnetic field and virus orientation are perpendicular to the scatter as shown in the schematic. Ψ is the angle from the equator on the detector film. Note the scales are different in (a) and (b).

At larger scattering angle, the zeroth and ±first *fd*layer lines are visible as shown in Fig. 5.1b. These intraparticle peaks are much less intense than the interparticle interference peaks and are the result of single particle scatter arising from the helical packing of the viral proteins. The layer lines occur at intervals along the $\hat{z}$ direction proportional to the reciprocal of the axial repeat of the helical protein coat, which is 33Å [89]. Because of discrepancy in both intensities and scattering angle between the interparticle and intraparticle scatter, we were unable to image both the high and low angle scatter simultaneously.

Because of the short ranged positional order in the nematic phase these intraparticle interference peaks should be independent of interparticle correlations. We confirmed this hypothesis by observing that the location of the peaks does not change with concentration as do the interparticle peaks. We also compared our data to published fiber diffraction results for M13 [45, 90]. M13 is also a filamentous bacteriophage, which differs from *fd*by only one amino acid per coat protein: their structures are otherwise identical and virtually indistinguishable by x-ray fiber diffraction [76]. Upon comparing published fiber diffraction data with our data from nematic fd, we observed that they were similar, but that the fiber diffraction patterns had Bragg peaks due to the hexagonal packing of the virus in the fiber which were absent in our nematic diffraction data. We also noticed that the horizontal location of the single particle peaks in the fiber diffraction was 4% larger than the location of our solution diffraction peaks, indicating that the fiber diffraction was done on virus which had a smaller diameter than those in our nematic samples. The fibers are partially dehydrated, so it is not surprising that they become compressed. The layer line spacing, however, was not altered, indicating that no stretching of the virus occurs in the fibers. From these observations we concluded that the high angle scatter from the nematic *fd*was independent of interparticle correlations. Detailed descriptions of the analysis of both the interparticle and intraparticle diffraction continues in the following sections.

5.4 X-ray Diffraction Analysis

5.4.1 Interparticle versus Intraparticle Interference

In x-ray diffraction, the scattered intensity consists of two parts, intraparticle scatter $F(\vec{q})$ and interparticle scatter $S(\vec{q})$. The intensity can be written as a product of the two types of scatter

$$I(\vec{q}) = NF(\vec{q})S(\vec{q}, f(\vec{q})) \tag{5.1}$$

where $\vec{q} = 4\pi \sin \frac{\Theta}{2}/\lambda$ is the three dimensional reciprocal vector in cylindrical coordinates $\vec{q} = (q_r, q_z, \phi)$. Θ is the angle between the incident and reflected x-ray beams of wavelength λ. In a uniaxial nematic, q_r is perpendicular to the nematic director and the scattered intensity is independent of the azimuthal angle ϕ about the director. If the system is oriented such that the nematic director is in the $\hat{z}$ direction, $\vec{q}$ can be described by $\vec{q} = (q_r, q_z)$. The intraparticle interference, or form factor $F(\vec{q})$, contains information about the structure of the individual particles. $F(\vec{q})$ can also be written as $< f(\vec{q})^2 >$ where $f(\vec{q})$ is the fourier transform of the electron density of a particle and the average is over all the particles and their orientations. The interparticle interference, or structure factor $S(\vec{q})$, contains information about the positional and orientational correlations between particles. The structure factor depends on the positions of the centers of gravity of two scatterers $\vec{R}_i, \vec{R}_j$ and their relative orientations [91]:

$$S(\vec{q}) = 1 + \frac{1}{NF(\vec{q})} < \sum_{i \neq j}^{N} e^{i\vec{q}(\vec{R}_i - \vec{R}_j)} f_i(\vec{q}) f_j(\vec{q}) > \tag{5.2}$$

The orientation of the particles is included in $f(\vec{q})$ and the average $<>$ is over all particles and their orientations. For scatterers of isotropic shape, $f_i(\vec{q}) = f_j(\vec{q})$ and the structure factor and the form factor decouple, but for anisotropic scatterers, $f_i(\vec{q}) \neq f_j(\vec{q})$ unless the particle orientations are the same. Therefore, in contrast to scatter from spheres, the structure factor $S(\vec{q})$ of rods can not, in general, be decoupled from its anisotropic form factor $F(\vec{q})$.

In a nematic system, however, there is no long ranged translational order. As a result, $S(\vec{q})$ approaches unity in the limit of high $\vec{q}$, and if $S(\vec{q}) = 1$ the scattered intensity is due only to the intraparticle interference diffraction and $I(\vec{q}) = F(\vec{q})$. In this regime the angular distribution of the scattered intensity is a function only of the single particle orientational distribution function. Because of the crystalline internal structure of viruses such as *fd*and Tobacco Mosaic Virus (TMV), x-ray diffraction produces a complex pattern of intraparticle scatter at high $\vec{q}$ which can be used to measure the single particle orientational distribution function of the viruses [81].

At low $\vec{q}$ the scattered intensity is dominated by $S(\vec{q})$, and the angular distribution of the interparticle interference scatter is influenced by the angular and spatial correlations between neighboring rods. When intraparticle interference scattering is absent or too weak to interpret, as in thermotropic liquid crystal systems [92], or the system of lyotropic vanadium pentoxide (V_2O_5) [84], x-ray investigations of the nematic orientational distribution rely on measuring the angular distribution from interparticle interference scattering. In this case one does not calculate the single particle orientational distribution function, but instead the coupled fluctuations of neighboring rods; this is predicted to overestimate the value of the nematic order parameter for highly ordered samples [92, 93].

5.4.2 Method for determining the orientational distribution function from diffraction images

Because of the short ranged positional order of the nematic phase, the high angle scattered intensity should be independent of interparticle correlations $S(q_r, q_z) = 1$. We have demonstrated above that this is true for fd. In this case, the intraparticle scattered intensity of a system of rods is related to the orientation of those rods in the following manner [81, 94]:

$$I(q_r, q_z) =< I_s(q_r, q_z) >= \int \Phi(\Omega) I_s(q_r[\Omega], q_z[\Omega]) d\Omega \tag{5.3}$$

Where Ω is the solid angle (θ, ϕ) a rod makes with respect to the nematic director θ and azimuthally with respect to the incident beam ϕ. Because *fd*is axially symmetric $\Phi(\Omega)$ simplifies to $\Phi(\theta)$. $I_s(q_r, q_z)$ is the axially symmetric three dimensional form factor $f(\vec{q})^2$ of a single rod. $\Phi(\theta)$ is the orientational distribution function (ODF) of the rods. Because the form of the ODF is not known exactly, three test functions were used:

$$\begin{aligned}\Phi(\theta) = &\quad A \exp -\tfrac{\theta^2}{2\alpha^2} \quad (0 \leq \theta \leq \pi/2) \\ = &\quad A \exp -\tfrac{(\pi-\theta)^2}{2\alpha^2} \quad (\pi/2 \leq \theta \leq \pi)\ , \qquad (5.4)\\ \Phi(\theta) = &\quad A \exp -\tfrac{(\sin\theta)^2}{2\alpha^2} \quad (0 \leq \theta \leq \pi)\ , \qquad (5.5)\\ \Phi(\theta) = &\quad \tfrac{\alpha \cosh(\alpha\cos\theta)}{4\pi \sinh\alpha} \quad (0 \leq \theta \leq \pi)\ , \qquad (5.6)\end{aligned}$$

where α sets the width of each of the peaked functions, and A is the normalization constant such that $\int \Phi(\theta)\sin(\theta) d\theta d\phi = 1$. Eq. 5.6 is normalized. The first ODF is the Gaussian used by Odijk [21], the second is the function used by Oldenbourg et al. [81] in their study of diffraction from nematic TMV, and the third was defined by Onsager. The second moment of the orientational distribution function, or the nematic order parameter, S (Eq. 5.5.3) was determined for the orientational distribution functions which best described the diffraction patterns.

Intraparticle interference analysis method

Previously Oldenbourg *et. al.* measured the ODF from the intraparticle interference scatter of TMV by simplifying Eq. 5.3 to a one dimensional integral at a constant q_r [81]. This one dimensional method could not be used for intraparticle *fd*scatter because *fd*has a protein coat with a pitch much larger than that of TMV, 33Å versus 23Å respectively, resulting in layer line overlap at low concentrations. Instead, the scatter from intraparticle interference was analyzed by comparing it to a simulated scatter created from the evaluation of Eq. 5.3 using a three dimensional model for the single rod form factor and a trial ODF.

A single long rod Fourier transforms as a disk of thickness $2\pi/L$ oriented perpendicular to the long axis of the rod[95]. Because of the helical periodic structure along the long axis of fd, the Fourier transform of a single *fd*consists of a series of disks separated by a distance proportional to the reciprocal of the period [96]. This is shown schematically in Fig. 5.2a. The radial intensity along these disks is a summation of Bessel functions whose exact form depends on the structure of the rod. When projected onto a screen these disks are visible as layer lines. The images shown in Figure 5.7b show the zeroth and ± first layer lines.

For our model, the radial intensities of the disks were approximated by [94]

$$I_s(q_r, q_z) = I_m(q_r, q_z)\sqrt{2\pi}\alpha q_r. \tag{5.7}$$

$\sqrt{2\pi}\alpha q_r$ is the disorientation correction term and I_m is the scattered intensities along the middle of the zeroth and ± first layer lines of our most aligned nematic sample, $S = 0.96$ and Gaussian $\alpha = 0.11$ as determined by the interparticle interference peak. For a small amount of disorientation of rods, the radial intensity decreases as $1/q_r$. The effect of the disorientation is illustrated in Fig. 5.2b. This approximation method was developed by Holmes and Leigh, and is valid if the sample from which the I_m is taken was well aligned [94]. The layer lines are located at $q_z = 0, \pm 0.33$Å, respectively.

In order to model diffraction from a nematic phase of fd, this single particle scattered intensity is multiplied by a test ODF and integrated over all possible angles of orientation, as in Eq. 5.3. The intersection of the resulting three dimensional nematic form factor and the Ewald sphere is then "projected" onto a two dimensional "screen" and a final two dimensional image is created, as shown in Fig. 5.2a. The shell thickness of the Ewald sphere was chosen to equal the energy uncertainty of the experimental beam $\Delta E/E = 5 \pm 1 \times 10^{-4}$. The "screen" image is then convolved with the Gaussian point spread function of the experimental x-ray beam on the CCD camera which was approximated as $\exp[-r^2/2\sigma^2]$ with $\sigma = 0.0063$ Å^{-1}, which is slightly larger (6 pixels at 0.00105 Å^{-1}/pixel) than the photon spread quoted by the CCD camera manufacturers (4 pixels). A series of two dimensional images were made for different orientational distribution functions with different amounts of disorder, examples can be seen in Fig. 5.7b.

The intraparticle interference data that fell on the detector in the range of $q_r = 0.19 - 0.33$ Å^{-1}, which encompasses the lowest q_r peak on each of the three layer lines visible in the interference pattern, was fitted to the model diffraction images. For each diffraction pattern, an α was found for each trial distribution function which minimized a computed chi-squared value

$$\chi^2 = \sum_i ((I_{data_i} - B) + CI_{model_i})^2 \tag{5.8}$$

where B and C are fitting parameters and i sums over the pixels in the scattered image. B was calculated once for each scattered image, and was not adjusted when comparing different ODF's.

Interparticle interference analysis method

To measure the orientational distribution function from the interparticle peak, the method of Oldenbourg et al. was used. Because we measure the angular spread of only one diffraction peak, Eq. 5.3 simplifies to a one dimensional integral at constant q_r:

$$I(\Psi) = \int \Phi(\theta) I_s(\omega) \sin\omega d\omega \tag{5.9}$$

where $I(\Psi)$ is the angular intensity distribution along an arc drawn at constant radius, Ψ is measured from the equator on the detector film, $\Phi(\theta)$ is the angular distribution function of the rods and ω is the angle between the rod and the incoming beam. Ψ, θ and ω are related by $\cos\theta = \cos\Psi \sin\omega$. Even though it was originally used for analyzing intraparticle scatter, this equation is identical to that used for analyzing thermotropic interparticle scatter, except that Oldenbourg's method includes a term which accounts for the length of the rod by defining the single rod scattering as $I_s(\omega) = 1/\sin\omega$, for small θ, where ω is the angle between the rod axis and the x-ray beam as illustrated in Fig. 5.2c. This $1/\sin\omega$ proportionality comes from the understanding that the Fourier transform of a rod of finite length is a ring with a finite thickness, and as ω decreases $1/\sin\omega$ increases and more of the disk intersects the Ewald sphere and is subsequently projected onto the detector screen.

Analysis done on interparticle interference from thermotropic liquid crystals typically defines $I_s(\omega) = 1$ [92, 93, 97]. It has been previously shown through calculations that neglecting the angular width when calculating the order parameter from interparticle interference scatter results in inaccurate values for the nematic order parameter for $S > 0.8$ [92]. However, in our analysis we observed that changing I_s from $1/\sin\omega$ to one in the interparticle interference scatter analysis did not have a significant effect on the calculated value of the nematic order parameter, nor did the χ^2 values reveal any information as to which I_s better describes the data. We chose to include the effect of rod length in our interparticle scatter analysis to be consistent with our intraparticle scatter analysis, which requires a knowledge of the rod length.

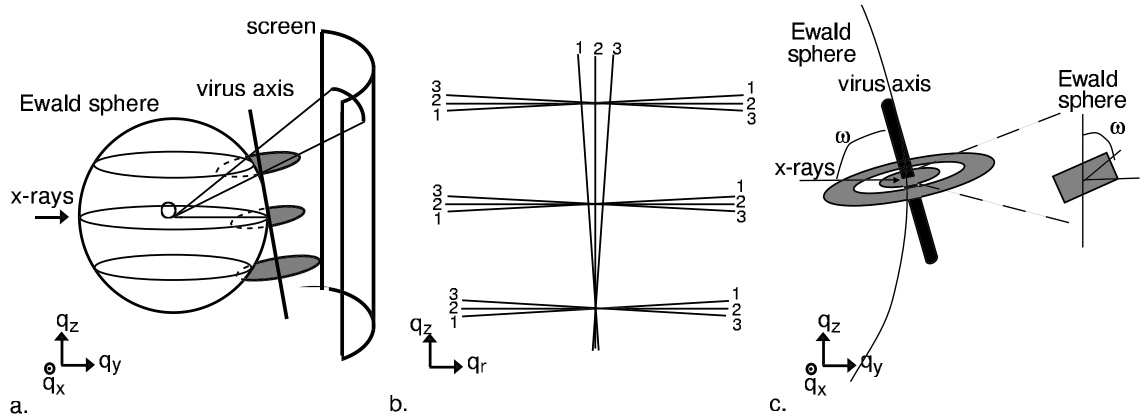

Figure 5.2: (a)Schematic of the Fourier space of a single rod tilted at a slight angle. (b) Schematic showing how the intensity along the center of the layer lines decreases as q_r when there is a small amount of angular disorder. Three rod axes (vertical) are labeled 1,2,3 along with their corresponding contribution to layer lines 0,1,2 (horizontal) as shown. (c) Schematic showing effect of the thickness of the form factor disks on the scatter with changing ω. The right hand image in (c) is an enlargement of the equatorial intersection of the Ewald sphere and I_s.

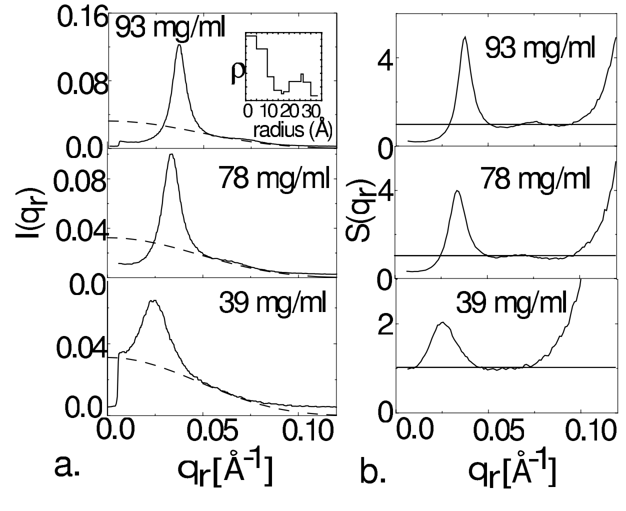

Figure 5.3: (a) Equatorial intensity profile, $I(q_r)$, and (b) equatorial structure factor, $S(q_r)$, for three representative samples at 10 mM ionic strength pH 8.2. Smaller inset graph is the binned cylindrically averaged electron density ρ used to calculate the equatorial form factor shown as a dashed line. The deviation of the structure factor from one at high q_r is due to both background noise in $I(q_r)$, which hides the actual form factor, and a loss of accuracy in the model form factor at high q_r.

5.5 Results

5.5.1 Nematic spatial ordering

The location of the maximum, q_m, of the first interference peak and its radial width, Δq_m, were measured along the equator, $q_z = 0$, in order to obtain information about the spatial ordering of the system. Because we are only analyzing data along the equator, these properties can be determined by dividing the equatorial form factor, $F(q_r, 0)$, from the scattered intensity peaks, $I(q_r, 0)$, and then by fitting the remaining structure factor peak, $S(q_r, 0)$, to a gaussian $S(q_r, 0) = e^{-(q_m - q_r)^2/2(\Delta q_m)^2}$ as done in Ref. [98] . $I(q_r, 0)$ and $S(q_r, 0)$ are shown in Fig. 5.3 for three different samples. The equatorial form factor scatter was approximated by the Fourier transform of the known equatorial projection of the cylindrically averaged electron density of *fd*[99]. The electron density was approximated by binning the radial electron density into 10 sections as illustrated in the inset of Fig. 5.3a. The location of the equatorial peaks produced by the Fourier transform of the electron density agree with the equatorial form factor data obtained at higher angle, but the increase in $S(q_r, 0)$ at high q_r shown in Fig. 5.3 indicates that this approximation is only qualitatively correct at high q_r and that the presence of background noise in the interparticle diffraction data hides any high q_r form factor information. At high concentrations the scattered intensity is much stronger than the readout noise and as a result we are able to analyze the structure factor data to higher q_r than at low concentrations.

The q_m and Δq_m measured are plotted as a function of concentration for two different ionic strengths in Fig. 5.4a. With increasing concentration c, the average rod separation decreases as $c^{-1/2}$ ($q_m \propto c^{1/2}$) as expected for both isotropic and nematic suspensions of rods [91, 82]. At a given concentration the rod separation remains constant and the variance increases with decreasing ionic strength. The electrostatic repulsion present between the rods causes the rods to maintain the maximum separation possible, but a smaller effective diameter at high ionic strength allows for more fluctuations. The number of rods per correlation length $q_m/\Delta q_m$ is plotted as a function of concentration in Fig. 5.4b. The concentration dependance of $q_m/\Delta q_m$ is much more significant at 10 mM ionic strength, than at 110 mM, indicating that at high ionic strength the rods are less correlated.

It is interesting to note that the second interference peak is much weaker than the first interference peak, indicating a large Debye-Waller factor. This is in contrast to charged 3D spherical and 2D disk systems which show a much stronger second, and even third interference peak [100, 101]. The structure factor of nematic *fd*also contrasts that of nematic end-to-end aggregated TMV, a very rigid rod, which has a structure factor closely resembling that of the 2D disk systems [98]. One way to interpret the large and sharp first peak in the structure factor of *fd*is that flexible nematic rods have long range spatial correlations similar to a dense fluid of disks. However the near absence of secondary peaks in the structure factor implies that *fd*particles have a greater degree of positional disorder about their average position than do disks. Perhaps the flexibility of *fd*accounts for this dramatic difference in spatial organization.

5.5.2 Experimental determination of the nematic orientational distribution function

By examining the χ^2 values obtained from orientational analysis (Section 5.4) of the inter- and intra-particle scatter, and the residues (I_{data}-I_{fit}) from the interparticle scatter orientational analysis we determined that analysis of x-ray diffraction data does not yield a unique orientational distribution function. The Gaussian and the Onsager distribution function each fit the intensity data equally well when comparing residues and χ^2 values from each of the two functions. However, we were able to eliminate Oldenbourg's distribution function from the possible ODF forms because

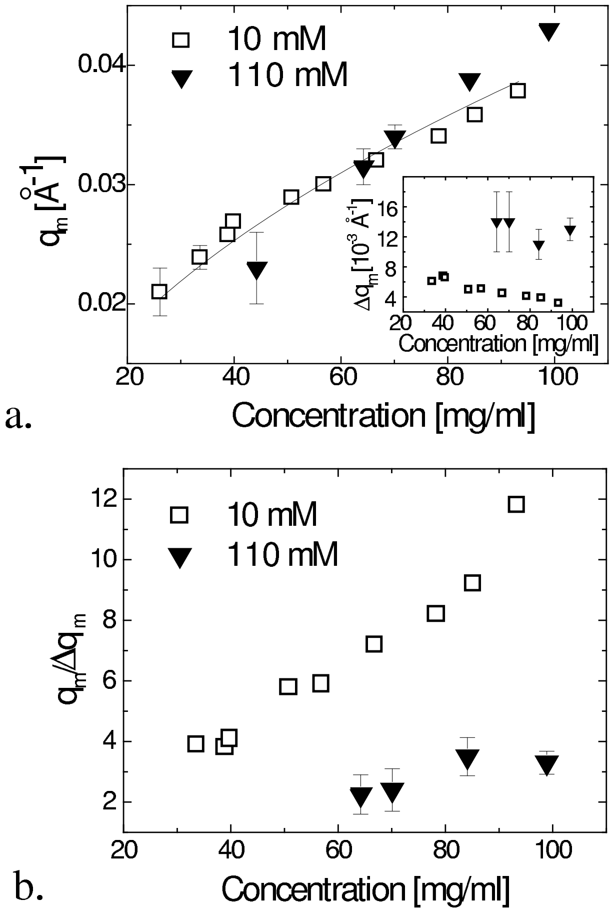

Figure 5.4: (a) The concentration dependance of the maximum q_m of the interparticle interference peak. The average rod separation is a distance of $2\pi/q_m$ Å. The equation of the curve fitted to the combined data sets is $q_m = 0.004c^{1/2}$. The inset graph shows concentration dependance of the variance of the interference peaks Δq_m. (b) The concentration dependance of $q_m/\Delta q_m$, the number of rods per correlation length. Squares (□) are at 10 mM and triangles (▼) are at 110 mM ionic strength pH 8.2.

it did not accurately model the tails of the diffraction data at low concentration. This insensitivity of x-ray diffraction to the exact form of the ODF was predicted by Hamley who showed that x-ray patterns are insensitive to higher order terms in the spherical harmonic expansion of the orientational distribution function and therefore only an approximation to the full orientational distribution function can be found [102].

To demonstrate this assertion, the scattered interparticle intensity at a constant radius of $q_r = 0.07 \pm 0.001$ Å^{-1} is plotted in Fig. 5.5a with the best-fit model intensities for each of the three ODFs. Ψ is the angle from the equator on the detector film as illustrated in Fig. 5.1a. The actual best-fit orientational distribution functions calculated from these interparticle angular scans are shown in Fig. 5.6. The residues calculated from the interparticle and intraparticle interference results for the three samples are illustrated in Figs. 5.5b and 5.7c, respectively. The intraparticle scatter residues shown are for the scattered intensity shown in 5.7a minus the model images shown in Fig. 5.7b created with the Gaussian ODF. The intraparticle model scatter produced relatively uniform residues indicating that it was a qualitatively good model. In two dimensions (Fig. 5.7c), we were unable to distinguish differences between residue plots of ODFs of the same width, therefore residue analysis was limited to the interparticle scatter (Fig. 5.5b).

At high concentration small systematic disagreements between the best-fit models and the data are most visible in the residue plots in Figs. 5.5b and 5.7c, but each of the three models and their respective ODFs are nearly indistinguishable. Except at low concentration, the best-fit model intensities obtained from the three distribution functions can not be distinguished from one another both by analyzing residue plots and by comparing minimum χ^2 values computed from the fitting routine. At low concentration the systematic disagreements between the data and the fits are lost in the noise, but disagreements in fits from different ODFs become visible. The

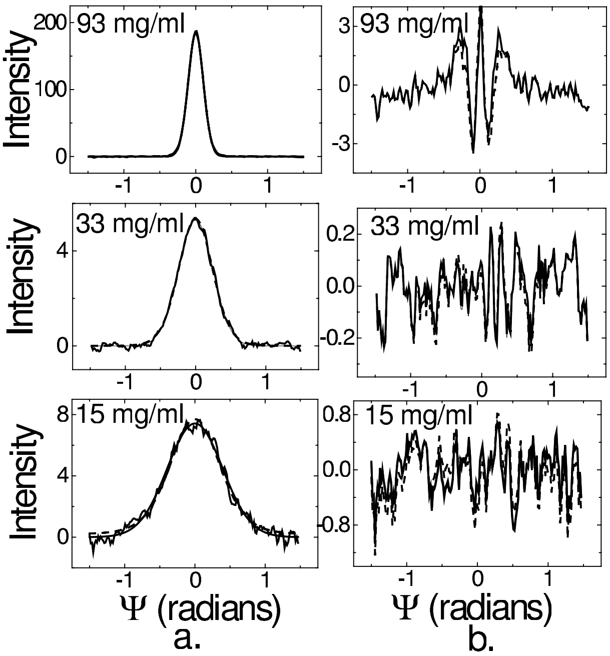

Figure 5.5: (a) Angular intensity scan at q_r=0.07 ± 0.001Å^{-1} from the three data scatter shown in Fig. 5.1a with best-fit curves calculated from the three trial ODF. Solid fit line represents fit of both the Gaussian and Onsager ODF's, dotted line is the fit of Oldenbourg's ODF. (b) Residue (I_{data} -I_{fit}) plot. Ψ is illustrated in Fig. 5.1a.

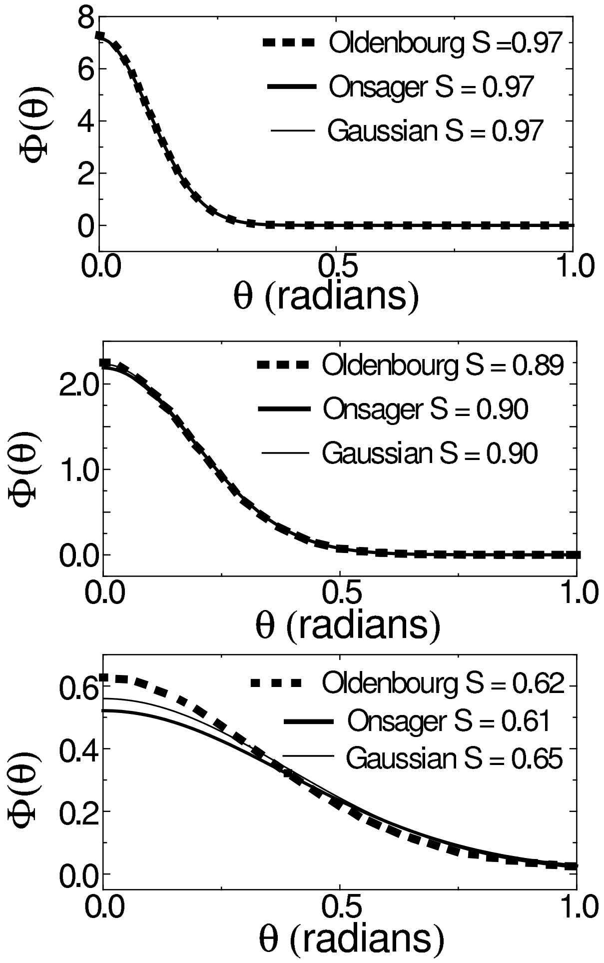

Figure 5.6: Orientational distribution functions calculated from the interparticle angular intensity scan at constant radius q_r=0.07 ± 0.001Å^{-1} shown in Fig. 5.5b. Gaussian (thin solid line) , Oldenbourg (dotted line) and Onsager (thick solid line) ODF are shown. Order parameters shown are calculated from each ODF. From top to bottom the concentration of the samples are 93 mg/ml, 33 mg/ml, and 15.5 mg/ml. The ionic strength of the samples is 10 mM, pH 8.2.

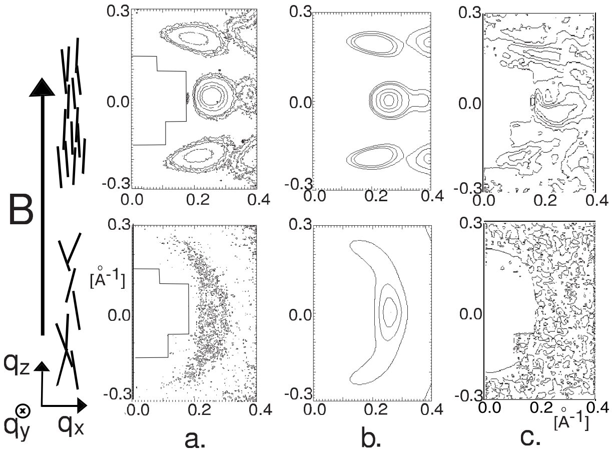

Figure 5.7: (a) Contour plots from Fig. 5.1b of scattering from nematic *fd*samples due to intraparticle interference. Bottom scatter is at 15.5 mg/ml and top is at 93 mg/ml. Samples were at 10 mM ionic strength pH 8.2. (b) Simulated intraparticle scatter using a Gaussian ODF which best fit the intraparticle scatter shown in (a). (c) Residue $(I_{data} - I_{fit})/I_{fit}$ plot. Maximum residues in (c) are ±10%. The axis of the plots are labeled in Å^{-1}.

best fit model intensities from the Gaussian and Onsager ODFs are indistinguishable, but the residues from the Oldenbourg ODF show disagreement, and the fits are systematically higher than the background scatter at high angle Ψ. The calculated Oldenbourg ODF also looks significantly different from the calculated Gaussian and Onsager ODFs. At the isotropic-nematic transition the χ^2 values computed from the Oldenbourg ODF were also consistently higher. From these qualitative observations we argue that the distribution function used by Oldenbourg et al. does not describe our diffraction data as well as the Gaussian or the Onsager distribution function at low concentrations. The Gaussian and the Onsager orientational distribution functions fit the diffraction data equally well.

Because of small differences in the trial orientational distribution functions (as illustrated in Fig. 5.6), best-fit ODFs vary slightly in their width, and subsequently returned slightly different order parameters. But, the order parameters calculated from the best-fit Gaussian and Onsager ODFs were in agreement with one another for a given sample within the experimental uncertainty of $\Delta S/S < 6\%$. Order parameters calculated with the Oldenbourg ODF were in common agreement at high concentrations, where model scatter agreed with the data. The nematic order parameter calculated at multiple q_r across interparticle peak also remained relatively constant, $\Delta S/S \leq 4\%$. Because we can not distinguish between the Gaussian and the Onsager model scatter, the order parameters to be presented henceforth are an average of the values calculated from only the Gaussian and the Onsager ODF, and the uncertainty on the values given are a combination of experimental error and uncertainty due to variation in order parameters from two trial ODFs.

5.5.3 Concentration and ionic strength dependence of the nematic order parameter

The concentration dependance of the nematic order parameters was measured from both the interparticle and intraparticle peaks and the resulting values are graphed in Fig. 5.8. In Fig. 5.9 the order parameter of the nematic phase in coexistence with the isotropic phase is plotted for five different ionic strengths as a function of concentration. The coexistence concentrations are an increasing function of ionic strength. Our analysis shows that the order parameters calculated from the interparticle and intraparticle scatter are consistent with one another both as a function of concentration and of ionic strength, indicating that correlations in the interparticle peak do not visibly change measured nematic order parameters. Fig. 5.8a shows data obtained at an ionic strength of 10 mM and Fig. 5.8b shows data obtained at an ionic strength of 110 mM, pH 8.2. With increasing concentration, the order parameter increases until it saturates near $S = 1$, and at constant concentration, the nematic order parameter decreases with increasing ionic strength. At low concentrations, the scattered intensity is spread over a large area due to the broad orientational distribution function, which leads to a large decrease in the signal to noise ratio, increasing the variation in the calculated order parameters to a maximum of $\Delta S/S \leq 10\%$. The solid lined theo-

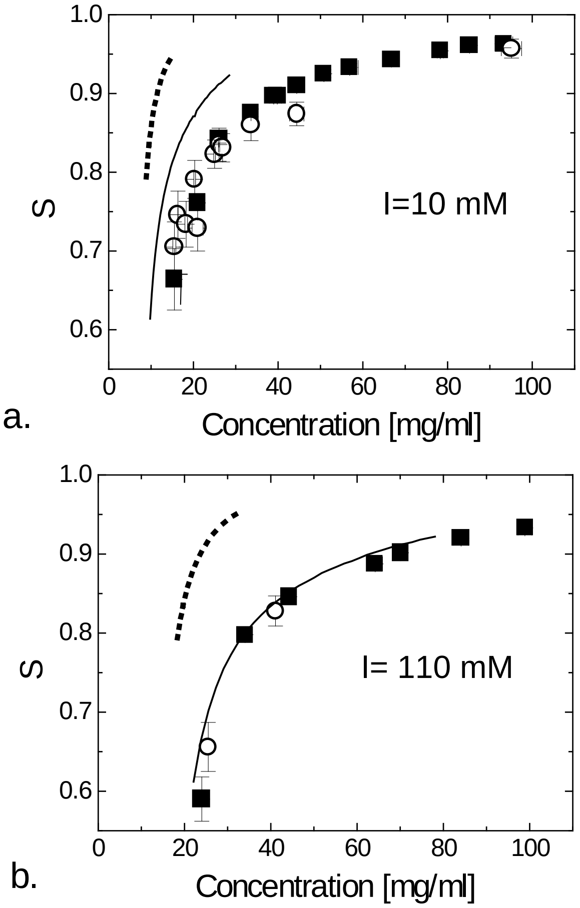

Figure 5.8: Concentration dependence of the nematic order parameter. (a) is at 10 mM, and (b) is at 110 mM ionic strength and pH 8.2. Squares (■) are from the interparticle interference peak, and open circles (○) are results from the intraparticle peak. The solid lines shown are for a scaled particle theory for charged semi-flexible rods described in Chapter 1. Dotted lines are theoretical curves for charged rigid rods in the Onsager model [80].

retical curves shown in Fig. 5.8 were computed from the scaled-particle theory which was described previously and includes semi-flexibility in the orientational entropy and electrostatic interactions by way of Onsager's effective diameter. For comparison, we also include as a dotted line the concentration dependence of the nematic order parameter from Onsager's theory for charged rigid rods at the second virial level as calculated by Lee[80]. Onsager's rigid rod theory is only valid at low concentrations near the isotropic-nematic transition for which the second virial approximation holds, whereas the scaled particle theory, which takes into account third and all higher virial coefficients in an approximate way, allows for a more adequate prediction of data at higher concentrations. The Onsager ODF was used in calculating each of these theoretical curves. The rigid rod theory does not agree with our data indicating that though our rods are fairly rigid, flexibility significantly changes the concentration dependence of the nematic order parameter. However, our results qualitatively agree with the scaled particle theory at low ionic strength, and quantitatively agree at high ionic strength. Deviation of the scaled particle theory from experimental results at low ionic strength is most likely due to using the effective diameter approximation to incorporate electrostatic interactions between the particles. This approximation is also valid only at low concentrations for which the second virial approximation holds.

The order parameters calculated from the x-ray diffraction data were also compared to birefringence measurements for the whole range of concentrations and these results are plotted in Fig. 5.10. Birefringence was measured by the technique described in Section 5.2. We expect $\Delta n/c = S\Delta n_{\mathrm{sat}}/c$ where Δn is the sample birefringence and Δn_{sat} is the birefringence of perfectly aligned *fd*[85, 49]. We observed that the x-ray order parameter measurements of S were indeed linear with the birefringence measurements $\Delta n/c$ with a zero intercept. From this relationship, the saturation birefringence per unit concentration was measured as $\Delta n_{\mathrm{sat}}/c = 3.8 \times 10^{-5} \pm 0.3 \times 10^{-5}$ ml/mg using data from samples at five different ionic strengths. Previously, Δn_{sat}

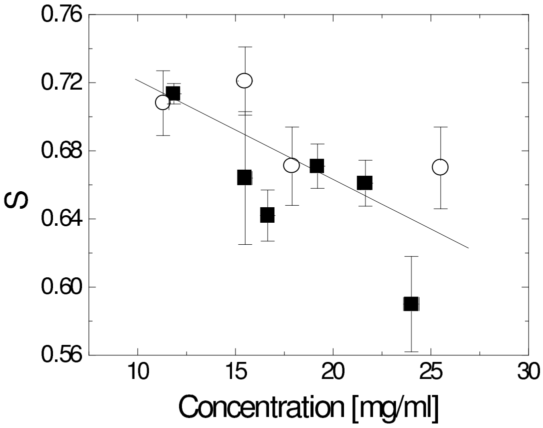

Figure 5.9: Concentration dependence of the order parameter of the nematic phase co-existing with the isotropic phase as determined from the intraparticle peak (open circles ○) and the interparticle peak (solid squares ■). Increasing coexistence concentration is due to increasing ionic strength [30]. The solid line is a linear fit to the combined sets of data and is presented as a guide to the eye.

was measured by Torbet *et. al.* to be $\Delta n_{\mathrm{sat}}/c = 6 \times 10^{-5}$ ml/mg. This value was calculated by assuming $S = 1$ for solutions of *fd*at 16 mg/ml in 10 mM Tris-HCL buffer at pH 7.5 in a 2-4 T magnetic field [49]. At 16 mg/ml we would expect the nematic order parameter to be $S \sim 0.75$ not $S = 1$, which would push the previously measured Δn_{sat} to a higher value even farther away from our measured value. We have no explanation why the previously published value is inconsistent with ours.

5.5.4 Comparison of nematic order parameter at coexistence with theoretical predictions

Theoretical models suggest that semi-flexibility acts to significantly lower the nematic order parameter at coexistence. For fd, a relatively rigid polymer with $L/p = 0.4$, the nematic order parameter at coexistence is predicted to be $S = 0.55$, which is significantly smaller than predicted for rigid rods, $S = 0.79$ [23]. Previous measurements of the isotropic and nematic coexistence concentrations of *fd*are well known to agree well with numerical results from Chen for $L/p = 0.4$ [30]. This order parameter

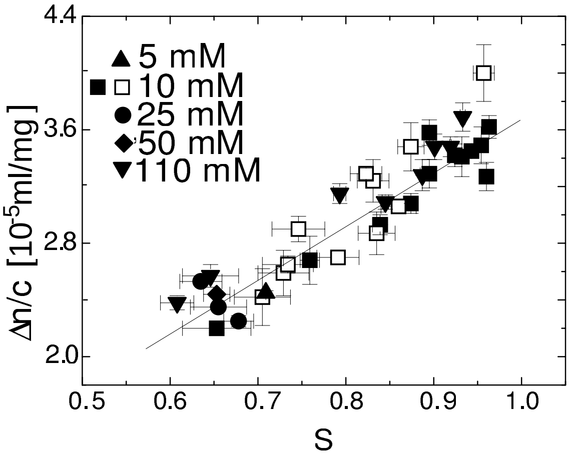

Figure 5.10: Comparison of measured birefringence $\Delta n/c$ to the deduced x-ray order parameter S. Open shapes are from intraparticle interference peak measurements. Closed shapes are from interparticle interference measurements. The equation of the fitted line is $\Delta n/c = (3.8 \pm 0.3)S - (0.11 \pm 0.19)$ where $\Delta n/c$ is in units of 10^{-5} ml/mg.

is predicted to remain constant independent of ionic strength, but in Figs. 5.9 and 5.11, a weak dependance of the order parameter with ionic strength is seen. In Fig. 5.11, the ionic strength dependance of the nematic order parameter at coexistence is plotted as deduced from both x-ray diffraction and birefringence measurements. The change in ionic strength from 5 mM to 110 mM corresponds to an L/D_{eff} for the rods changing from ~ 40 to ~ 85. As the effective aspect ratio for approaches the long rod limit, $L/D_{\text{eff}} > 100$, the coexistence order parameter decreases, approaching the theoretically predicted value of $S = 0.55$, as calculated by Chen for long semi-flexible rods with a length to persistence length ratio, $L/p = 0.4$ [23]. Even though the persistence length of *fd*virus is more than twice its contour length, and thus can be considered fairly rigid, all of our co-existing samples had a nematic order parameter significantly lower than the Onsager prediction of $S = 0.79$ as measured by both diffraction and birefringence.

To explain the ionic strength dependence of the order parameter at the isotropic-nematic transition we turn to electrostatic interactions. Stroobants et al., have shown

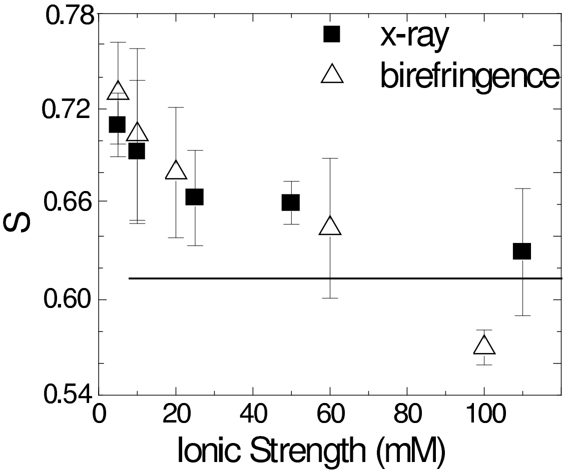

Figure 5.11: Ionic strength dependance of the order parameter of the nematic phase co-existing with the isotropic phase as calculated by x-ray diffraction measurements (solid squares ■) and birefringence measurements (open triangles △). X-ray points are an average of co-existence order parameters measured from inter- and intraparticle scatter at the same ionic strength. Solid line shows the order parameter predicted by scaled particle theory for charged semi-flexible rods as in Fig. 5.8.

theoretically that there is an additional electrostatic twisting factor which acts to misalign adjacent particles and decrease the nematic order parameter at coexistence [57]. This effect scales as $h = \kappa^{-1}/D_{\text{eff}}$ where κ^{-1} is the Debye screening length. The effect of h on the coexistence concentrations of the system is predicted to be small [57, 30], as the nematic order parameter is predicted to increase 2.4% when decreasing ionic strength from 110 mM to 5 mM, whereas we measure an increase of about 15%. Decreasing the ionic strength of the solution is also predicted to increase the nematic order parameter by way of increasing the electrostatic persistence length [51]. However this effect is also predicted to be small as the effective electrostatic persistence length of *fd*(2.203 μm at 10 mM ionic strength) is less than one percent larger than the bare persistence length(2.2 μm). Nevertheless, the observed trend of increasing order parameter with decreasing ionic strength suggests that electrostatics is significantly affecting the nematic order parameter. It is also important to note that below about 10 mM, the concentration of the virus may begin to have an effect on the ionic strength of the solution in that the concentration of the virus counterions may act to increase the ionic strength. Overall, we expect and observe better agreement with the theoretical predictions for the nematic order parameter at high ionic strength.

5.6 Conclusions

To summarize, we have observed, as predicted by Hamley [102], that the method of using x-ray diffraction to calculate the orientational distribution function is insensitive to the details of the form of distribution function used. Nevertheless, we were able to rule out the function used by Oldenbourg et al. [81] because we could qualitatively see that models created using this function did not fit the data equally well at low concentration and at high angle Ψ from the equator on the detector. The Onsager and Gaussian trial angular distribution functions fit the angular distribution of both the intraparticle and interparticle diffraction peaks equally well and returned similar values for the nematic order parameter. The concentration dependence of the nematic order parameter at high ionic strength, or large L/D_{eff}, as determined from both the interparticle and intraparticle scatter agrees with that predicted by a scaled particle theory of charged semi-flexible rods. At low ionic strength, theoretical predictions qualitatively reproduce the concentration dependance of the order parameter. Similar agreement of the concentration dependence of nematic ordering to Onsager's theory has been measured for other semi-flexible molecules [82, 83, 40]. This similarity demonstrates the universality of Onsager's theory and its applicability to charged semi-flexible systems.

The nematic order parameters derived from both interparticle and intraparticle scatter return similar results, implying that it is sufficient to use the easier, one dimensional analysis of the interparticle interference peak to calculate nematic order parameters as has been done for many years for thermotropic liquid crystals. It has also been shown that the relationship between the birefringence and the nematic order parameter as calculated by x-ray diffraction is linear. From this relationship the saturation birefringence of *fd*was calculated. Subsequently, the order parameter can also be obtained simply by measuring the birefringence of a sample of nematic *fd*and rescaling it by the saturation birefringence. We note that the birefringence measurements were less reproducible than diffraction measurements, as can be observed by the large variance in the data points throughout the entire range of data shown in Fig. 5.10.

The spatial ordering of nematic *fd*was also explored. The structure factor had a single large peak and a much diminished second peak in contrast to experiments with TMV, a rigid rod [98].

At high ionic strength, or large effective aspect ratio, we observed that the order parameter of the nematic phase coexisting with the isotropic phase was $S \sim 0.6$, close to the theoretically predicted value for semi-flexible rods and significantly lower than the theoretical value of $S = 0.79$ for rigid rods. Agreement is very good with scaled particle theory predictions for the order parameter $S = 0.61$. With decreasing ionic strength however, a weak systematic increase in the nematic coexistence order parameter was found. This is consistent with both a decrease in the twist parameter $\kappa^{-1}/D_{\text{eff}}$ and an increase in the electrostatic persistence length, though these effects are predicted to be seven times smaller than observed. In order to fully understand the interactions which are producing the nematic phase diagrams, particularly at lower ionic strength where L/D_{eff} is small, new theories and simulations need to be developed which include a more complete picture of the complicated electrostatic interactions.

5.7 Appendix: Birefringence Calculation

The birefringence of an aligned nematic phase oriented perpendicular the incident light is directly related to the second moment of the orientational distribution function. The following is a derivation of this relationship [103].

A light beam is directed along the y-axis through a magnetically aligned sample with a polarization in the $x - z$ plane. The polarization per unit volume, $\vec{P}$, can be related to birefringence by the following steps:

$$\vec{P} = \frac{N}{V}\vec{p} = N\alpha\vec{E} = \chi\vec{E} = \frac{(n^2 - 1)\vec{E}}{4\pi} \tag{5.10}$$

where $\vec{p}$ is the dipole moment of a rod,$\frac{N}{V}$ is the number of rods per unit volume,α is the polarizability of a rod, χ is the susceptibility of the bulk solution of rods, and n is the index of refraction, which is related to χ by $n^2 = \epsilon = 1 + 4\pi\chi$, for uniform χ. χ and α are both 3x3 matrices. Because the light is directed in the y direction, the polarizations of interest are P_x and P_z. The total birefringence of the sample, $\Delta n = n_z - n_x$, for small deviations between n_z and n_x is derived by:

$$n_z^2 - n_x^2 \approx (n_z - nx)(n_z + n_x) \approx (n_z - n_x)2\Delta n \tag{5.11}$$

For a system of rods with a distribution $f(\mathbf{\Omega})$, the index of refraction can be written as:

$$\Delta n = \frac{4\pi N}{2nV}\int f(\mathbf{\Omega})(\alpha_{zz} - \alpha_{xx})d\mathbf{\Omega} \tag{5.12}$$

where α_{zz} and α_{xx} are from the α matrix. The index of refraction (n_i) in a given direction only depends on the component of the polarizability(P_i) in the direction of the field(E_i).

To determine α_{zz} and α_{xx} the α matrix is determined for an arbitrary orientation of a rod. In the rod frame, the polarizability is as follows

$$\alpha = \begin{pmatrix} \alpha_\perp & 0 & 0 \\ 0 & \alpha_\perp & 0 \\ 0 & 0 & \alpha_\parallel \end{pmatrix} \tag{5.13}$$

where $\alpha_\perp$ is the polarizability perpendicular to the rods long axis, and $\alpha_\parallel$ is the polarizability of the rod parallel to its long axis. To calculate polarizability of a rod oriented at angles θ, ϕ in the lab frame, the rotation matrix needed is:

$$\mathbf{R} = \begin{pmatrix} \cos\phi\cos\theta & \sin\phi & -\sin\theta\cos\phi \\ -\sin\phi\cos\theta & \cos\phi & \sin\phi\sin\theta \\ \sin\theta & 0 & \cos\theta \end{pmatrix} \tag{5.14}$$

this comes from rotating the rod coordinate system first by θ about the x_{rod}-axis, then by ϕ about the z_{lab} axis. α in the lab frame is obtained by performing the matrix multiplication $[\mathbf{R}][\alpha][\mathbf{R}]^{-1}$. The resulting values for α_{xx} and α_{zz} are:

$$\alpha_{zz} = \alpha_\perp \sin^2\theta + \alpha_\parallel \cos^2\theta \tag{5.15}$$

$$\alpha_{xx} = \alpha_\perp \cos^2\phi\cos^2\theta + \alpha_\perp \sin^2\phi + \alpha_\parallel \sin^2\theta\cos^2\phi \tag{5.16}$$

These values can then be used in Eq. 5.12. After assuming that $f(\mathbf{\Omega})$ is cylindrically symmetric and depends only on θ, and doing some algebra the following equation is obtained:

$$\Delta n = \frac{4\pi N}{2nV}(\alpha_\parallel - \alpha_\perp)\int 2\pi\frac{1}{2}(3\cos^2\theta - 1)d(\cos\theta) \tag{5.17}$$

the integral is exactly the nematic order parameter, S. Rewriting the equation with this knowledge gives,

$$\Delta n = \frac{4\pi N}{2nV}(\alpha_\parallel - \alpha_\perp)S \tag{5.18}$$

if we define $\frac{4\pi N}{2nV}(\alpha_{\parallel} - \alpha_{\perp})$ to be the birefringence per density then $S = \Delta n/\Delta n_{sat}$.

Chapter 6

Nematic phase transitions in mixtures of thin and thick colloidal rods

In this Chapter, we present the first experimental measurements of the isotropic and nematic phases of mixtures of thin, charged semiflexible *fd* virus, and thick, *fd*-PEG created by covalently grafting poly-(ethylene glycol) to the surface of *fd*, rods. The *fd*-PEG is sterically stabilized and its phase behavior is independent of ionic strength. The *fd* is charged, therefore by varying the ionic strength of a mixture of *fd* and *fd*-PEG, only the effective diameter of the bare *fd* rods changes, subsequently varying the effective diameter ratio ($d = D_{fd\text{-PEG}}/D_{fd}$) from 3.7 to 1. In solution, binary mixtures of *fd* and *fd*-PEG are shown to exhibit isotropic-nematic, isotropic-nematic-nematic and nematic-nematic coexisting phases with increasing concentration. We measure the binary phase diagrams as a function of composition, total concentration, and ionic strength. We find a lower critical point in the nematic-nematic coexistence which has not been observed previously. These experimental results are qualitatively described with a rescaled Onsager-type theory for the phase behavior of binary rod mixtures.

Measurements of the stability of nematic-nematic coexistence of bidisperse mixtures of rods of different diameter and length are also presented in an appendix at the end of this Chapter.

6.1 Introduction

The entropy driven phase transition of monodisperse suspensions of purely repulsive rods from an isotropic to an aligned nematic phase has been extensively studied theoretically [1], in simulations [25] and in experiments [14, 40] over the past 50 years. Binary mixtures of hard particles of different aspect ratios have an even richer phase diagram. Theoretical studies of binary mixtures of hard rods predict that in addition to isotropic-nematic (I-N) coexistence, isotropic-nematic-nematic (I-N-N), isotropic-isotropic (I-I) and nematic-nematic (N-N) coexistence are stable when the length or diameter ratio of the particles is large enough [6, 104, 8, 10, 105, 12]. Experimentally, however, only I-N, I-N-N and N-N coexistence have been observed, and only in binary length mixtures [40, 106, 107, 108]. Because of polydispersity, viscosity and/or weak attractions, past experiments have been constrained to studies near the I-N transition [40, 106, 107]. Consequently, the location and stability of N-N coexistence is still a topic of much controversy. The phase behavior of binary hard rod mixtures was recently predicted to include N-N coexistence constrained by an upper critical point at rod concentrations above and I-N-N three phase region for rods of large size difference [109, 8, 110, 105]. However it has also been predicted that N-N coexistence may be stable in the absence of an I-N-N coexistence region, by way of a lower critical point bounded N-N region [105]. In this Chapter we present experimental measurements of the phase behavior of bidisperse mixtures of thin and thick rods of equal length and multiple diameter ratios to very high nematic concentrations. These rods are strongly repulsive and highly monodisperse. With phase diagrams well into the nematic region we experimentally answer the question of the evolution of nematic-nematic coexistence in bidisperse mixtures [8, 110, 105]. We compare these results to the theoretical predictions for bidisperse rod phase behavior [105].

The origin of liquid crystal phase formation in a bidisperse rod mixture is closely related to monodisperse hard rod theory, which was originally developed by Onsager [1]. Onsager showed that the decrease in orientational entropy present in an aligned nematic phase is more than compensated for by an increase in the excluded volume entropy of the rods. Onsager also extended his second virial theory for the free energy of hard-rigid rods to binary mixtures [1]. The binary phase behavior at the limit of the second virial coefficient (Onsager's theory) has subsequently been determined numerically for mixtures of different diameter [8], and different length [110]. We note that many other studies of binary rod phase behavior have been published [111, 10, 104, 12], however these studies use an analytical trial function to describe the orientational distribution of the nematic rods. Minimizing the free energy numerically has the advantage that the orientational distribution function used, though not analytical, is exact. For monodisperse rod suspensions the difference in predicted phase behavior between these two methods is small [112]. However, in binary rod suspensions using an approximate orientational distribution function predicts qualitatively different phase behavior from that predicted when the same free energy is solved numerically [110, 109].

The description of the I-N transition at the level of the second virial expansion of the free energy is quantitatively accurate only for particles of infinite aspect ratio [1]. In this Chapter, we experimentally study the phase behavior of binary mixtures of rods of finite aspect ratios. Correspondingly, to compare our experimental results with theoretical predictions, we adopt a Parsons-Lee free energy, as used by Varga *et. al.* [113, 114, 105] which can be thought of as an interpolation between the Carnahan-Starling free energy for hard spheres and the Onsager free energy for long, hard rods, yielding the following expression:

$$\frac{\beta F}{N} = \text{const} + \sum_{i=1}^{2} x_i(\ln(\rho) + \ln(x_i) + \sigma(f_i)) +$$
$$\frac{\beta F_{\text{exc}}^{\text{HS}}}{N v_{\text{HS}}} \sum_{i=1}^{2} \sum_{j=1}^{2} \int \int x_i x_j v_{ij}(\Omega_1, \Omega_2) f_i(\Omega_1) f_j(\Omega_2) d\Omega_1 d\Omega_2$$

In this equation $\beta = 1/k_B T$ (T is the temperature and k_B is Boltzmann's constant), $\rho = (N_1 + N_2)/V$ is the total number density, x_i and f_i are, respectively, the mole fraction and orientational distribution function of particle i. The term σ is the single particle orientational entropy term, v_{ij} is the excluded volume between particles i and j, and Ω is the orientational unit vector (polar and azimuthal angles) [105]. In the second term, $\beta F_{\text{exc}}^{\text{HS}}/N v_{\text{HS}} = (4\eta - 3\eta^2)/8(x_1 v_1 + x_2 v_2)(1-\eta)^2$, where $F_{\text{exc}}^{\text{HS}}$ and v_{HS} are the residual free energy and volume of an equivalent hard sphere system, $\eta = \rho(x_1 v_1 + x_2 v_2)$ is the packing fraction, and v_1 and v_2 are the volumes of particles 1 and 2. Parsons-Lee scaling is appropriate for studying phase transitions between isotropic and nematic phases, but not phases of higher order (smectic, columnar) as no positional inhomogeneity is incorporated into the free energy. The theoretical phase diagrams presented here are calculated numerically from this free energy functional using techniques previously described [115, 105].

6.2 Experimental System

Experimentally, our system consists of mixtures of two well characterized systems, suspensions of the charged semiflexible *fd* virus [30] and *fd* virus irreversibly coated with the neutral polymer poly(ethylene glycol) (PEG) [37, 38]. The bare *fd* virus will serve as our thin rods, while the polymer coated *fd* (*fd*-PEG) will be our thick rods. Both pure *fd* and pure *fd*-PEG suspensions exhibit an isotropic-cholesteric transition. Because the free energy difference between the cholesteric and nematic phases is small, comparison with nematic theories is appropriate [39]. Properties of the bare *fd* include its length $L = 880$ nm, diameter $D = 6.6$ nm, surface charge of 10 e^{-}/nm at pH 8.2 and molecular weight $M_w = 1.64 \times 10^7$ [14]. The virus has a persistence length, defined as the tangent-tangent correlation length along a polymer, of P =2.2 μm. The *fd* virus was grown and purified following standard biological protocols [116]. The *fd* rods are charged, thus to compare *fd* phase behavior with hard rod predictions the electrostatic interactions are accounted for by rescaling the bare rod diameter D to a larger effective diameter D_{eff}, calculated from Onsager's second virial coefficient, which increases with decreasing ionic strength [1, 16]. Over a wide range of ionic strengths, monodisperse suspensions of *fd* are known to undergo a phase transition from an isotropic phase to a nematic phase which is accurately described by Onsager's theory for semiflexible rods with diameter D_{eff} [30], as illustrated by the squares in Fig. 6.1. The relationship between the isotropic coexistence concentrations (c_i) and the effective diameter can be calculated from Onsager's theory and is equal to c_i[mg/ml]= $222/D_{\text{eff}}$[nm] for semiflexible rods with $L/P = 0.4$[37, 23]. This implies that the interaction between the bare *fd*is additive. However, because D_{eff} is not an actual hard diameter, the interaction between bare *fd* and *fd*-PEG is non-additive, as shown in the inset of Fig.6.1.

Our thick rods were created by attaching a 20,000 molecular weight [g/mol] amino-reactive PEG (SSA-PEG20K, Shearwater Polymer Corp.) to the exposed amino termini of the viral coat proteins. Monodisperse suspensions of these *fd*-PEG rods have been investigated [37] and it has been shown that the dense polymer coating of approximately 200±30 PEG20K molecules per *fd* [38] acts as a steric stabilizer above an ionic strength of 2 mM. In this regime, *fd*-PEG exhibits an ionic strength independent isotropic-nematic phase transition (Fig. 6.1). The effective diameter of the thick rods (virus+polymer) is calculated from the monodisperse isotropic coexistence concentrations, resulting in a value of D_{thick} from 25 to 40 nm, depending on

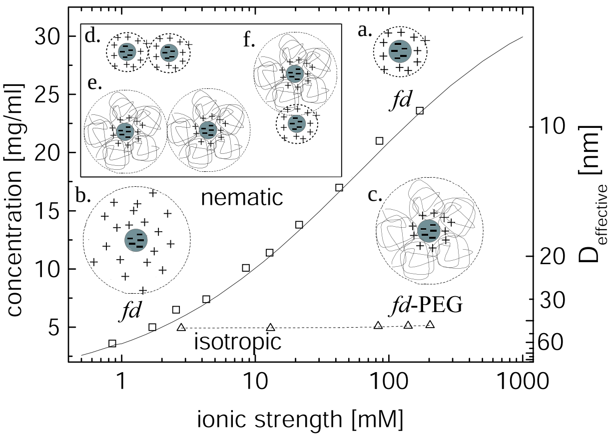

Figure 6.1: (Color Online) Isotropic-nematic phase boundary as a function of ionic strength for pure *fd* (squares) and pure *fd*-PEG (20,000 M_w)(triangles). The data is taken from previous work [30, 37]. The theoretical relationship between the I-N coexistence concentrations (c_i) and the effective diameter c_{i}[mg/ml]= $222/D_{\mathrm{eff}}$[nm] is shown by the solid line, as calculated from Onsager's theory for semiflexible rods with $L/P = 0.4$ [23, 37]. The concentration measured is the bare *fd* concentration, the mass of the PEG is not considered. The illustrations show end-on pictures of (a)*fd* at high ionic strength,(b) *fd*at low ionic strength and (c) and *fd*-PEG. The inset illustrates the distance of closest approach for (d) two *fd* rods, (e) two *fd*-PEG rods, and (f) *fd* and *fd*-PEG. Interactions are additive in (d) and (e), non-additive in (f).

the reaction conditions. D_{thick} was determined for each *fd*-PEG reaction and rods with different D_{thick} were used separately.

6.3 Observation of bulk phase separation

To determine the binary phase diagram of *fd* and *fd*-PEG mixtures samples were prepared at multiple virus compositions and concentrations. Virus suspensions were dialyzed against 20mM Tris-HCl buffer at pH 8.15 with NaCl added to vary ionic strength such that the diameter ratio $D_{\mathrm{thick}}/D_{\mathrm{thin}} \equiv d$ varied from $1 < d < 3.7$. To hasten phase separation, samples were occasionally centrifuged at 3300g [m/s^2]. We verified that centrifugation did not alter the coexistence concentrations, a concern raised by recent theory [117]. Bulk phase separation typically occurs on the order of days to weeks. Phase separation yields either an isotropic phase (I) coexisting

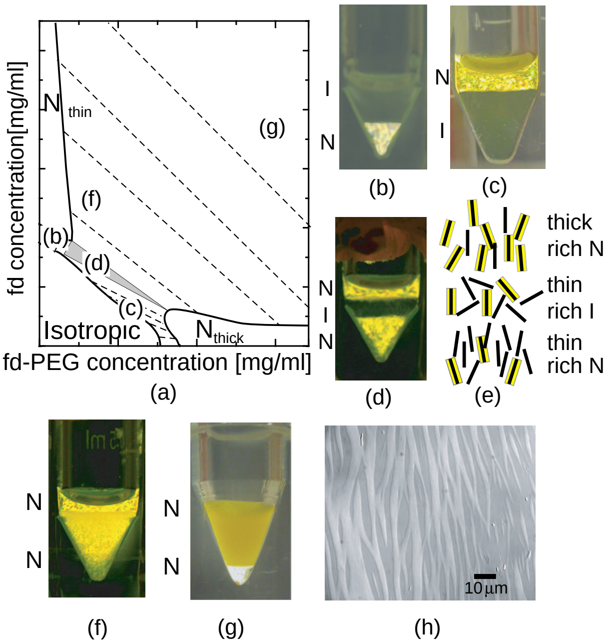

Figure 6.2: (Color Online) Phase separation of mixtures of *fd* and *fd*-PEG (20,000 M_w PEG) at 110mM ionic strength ($d = 3.7$) as viewed under crossed polarizers. The isotropic phase is dark and the nematic phase is birefringent. Yellow color in the nematic phases is due to the dye on the thick rods. The location of the samples on the phase diagram is represented schematically in (a). (b) I-N coexistence. (c) Highly fractionated I-N coexistence. In (c) a *fd*-PEG-rich nematic phase floats above the *fd*-rich isotropic phase, even though the volume fraction of rods is higher in the nematic, due to the difference in mass density between the two phases. The mass density difference arises in part because of the difference in single particle densities $\rho = 1.35$ for *fd* and $\rho = 1.007$ for *fd*-PEG. (d) I-N-N triphasic region. (e) Schematic representation of the fractionation of thick and thin rods in the I-N-N triphasic region. (f) Nematic-nematic demixing just above the triphasic region. (g) Highly concentrated N-N coexistence showing strong fractionation of the thick (yellow, *fd*-PEG) and thin (white, *fd*) rods. (h) Differential interference contrast microscopy image of low density *fd*-PEG-rich nematic tactoids in coexistence with high density *fd*-rich nematic bulk phase.

with a nematic (N) phase, I-N-N three-phase coexistence, or N-N coexistence. This confirms the theoretical predictions for the stable coexisting phases [8, 105]. Fig. 6.2 depicts these coexisting phases as viewed under crossed polarizers. Because of our unique system N-N coexistence is very stable to high concentrations (see Fig. 6.2f,g). After equilibration, the concentrations of *fd* and *fd*-PEG in coexisting phases were measured by absorption spectrophotometry. The optical density (A) of *fd* is $A^{269\mathrm{nm}}_{3.84\mathrm{ml/mg}}$ for samples 1 cm thick. To independently measure the thin and thick rods in the coexisting phases, *fd*-PEG was also labeled with fluorescein isothiocyanate (FITC) dye molecules which have an optical density of $A^{495\mathrm{nm}}_{68000\mathrm{L/mol}}$.

Samples which did not bulk phase separate were observed using fluorescence and polarization microscopy. If in coexistence, droplets of one phase in another can easily be seen, however microscopic coexistence did not necessarily result in bulk phase separation even after many months. Fig. 6.2h shows a representative differential interference contrast (DIC) image of nematic-nematic coexistence, which did bulk phase separate after a few days. Strong difference in concentration is indicated by a large difference in intensity between the two nematic phases in the DIC image.

6.4 Results

In Fig. 6.3 we present a characteristic phase diagram of an *fd* and *fd*-PEG mixture at high ionic strength. At low concentrations of *fd* and *fd*-PEG the system is in an isotropic phase. With increasing concentration of either rod the system will exhibit isotropic-nematic coexistence. If the mixture is predominantly one type of rod (thin-rich or thick-rich), only an I-N transition will occur. The I-N transition of thin or thick rich samples the suspension will remain completely nematic to very high concentrations. With roughly equal amounts of *fd* and *fd*-PEG the system will exhibit I-N-N coexistence above the I-N transition. Additionally, in this region of equal

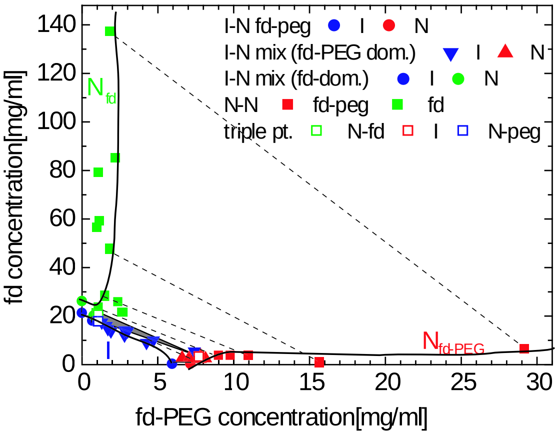

Figure 6.3: Phase diagram of mixtures of *fd* and *fd*-PEG (20 000 M_w PEG) at 110 mM ionic strength ($d = 3.7$). Coexisting phases are indicated by dashed lines. Solid lines are a guide to the eye indicating the phase boundaries.

ratios of *fd* and *fd-PEG* the composition of the isotropic and nematic phases is highly fractionated. The thick rods partition into the nematic phase while the thin rods remain in the isotropic phase. This partitioning is due to the fact that the thick rods prefer alignment because of their comparatively large excluded volume interactions [8]. The degree of fractionation in a coexisting sample can easily be determined by the slope of the tie line. If there is no fractionation, equal ratios of thin and thick rods will be in each of the coexisting phases and the tie lines will intersect the origin of the graph. A fractionated sample will have different ratios of the two particles in each of the two phases and the tie lines will not intercept the origin. At higher concentrations N-N coexistence is stable from the region of I-N-N coexistence to arbitrarily high concentrations. Partitioning of *fd* and *fd*-PEG is very strong the N-N region, as well as in the I-N region.

In Fig. 6.4 we present the experimental phase diagrams of the bidisperse mixture of *fd* and *fd*-PEG at four ionic strengths such that $1.1 < d < 3.0$. At large diameter ratios, $d > 3.0$ in Fig. 6.4a, large fractionation is seen in the isotropic-nematic coexistence region, followed by a triangular I-N-N three phase region and

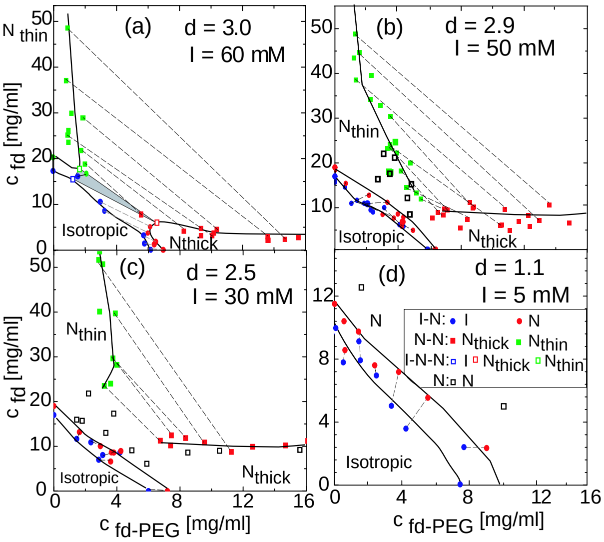

Figure 6.4: (Color Online) Phase diagrams of suspensions of *fd*-PEG (20,000 M_w PEG) mixed with *fd* at (a) 60 mM, (b) 50 mM, (c) 30 mM and (d) 5 mM ionic strength pH 8.2. Above $d = 3.0$ I-N, I-N-N, and N-N coexistence is observed (a). Below $d = 3.0$ N-N coexistence exists above a single phase nematic and the I-N-N triphasic region is absent(b,c). Below $d \approx 2.0$ only I-N coexistence is observable (d). The legend for all four diagrams is in (d). Dark lines are guides to the eye representing the phase boundaries of the two nematic phases and the isotropic phase. Dashed lines indicate coexisting samples, and open squares are single phase nematic samples as determined by fluorescence microscopy.

N-N coexistence with increasing concentration. Almost complete partitioning of the thick and thin rods is observed in the N-N coexistence region. The I-N-N coexistence region becomes smaller as d decreases, and pinches off such that below about $d = 3.0$ the triphasic region vanishes. Between $d = 3.0$ and $d \sim 2.0$ there is a continued presence of N-N coexistence at high concentrations, even in the absence of a well defined I-N-N triangle, suggesting a lower critical point bounded N-N region. The partitioning of thick rods into the nematic phase coexisting with the isotropic phase also decreases significantly without I-N-N coexistence, as indicated by the shortening of tie lines which do not radiate from the origin in Fig. 6.4b,c. Below a diameter ratio of approximately $d = 2.0$ only a single nematic phase is observed and all tie lines radiate from the origin (no partitioning).

6.5 Comparison to Theory

For comparison with our experimental results we present the phase behavior predicted by numerically solving the free energy functional from Parsons-Lee theory [105] in Fig. 6.5. The actual calculations for the Parsons-Lee theoretical phase behavior were performed in collaboration with S. Varga. We also present the phase behavior predicted from the second virial theory in Fig. 6.6, as determined by van Roij *et. al.* [8]. From Parsons-Lee scaling of the free energy, four distinct types of phase diagrams (indicated by the Greek symbols) are predicted as a function of the diameter ratio and the length of the thick rods. Fig. 6.5b-f displays the qualitative evolution of the phase behavior as a function of d for $L/D_{\text{thick}} = 4$ and 24 (experimental L/D_{thick}). The I-I region (δ) is not probed experimentally and is not discussed here. For very small d, Region α, an isotropic to homogenous nematic transition is predicted at low concentrations and a N-N coexistence region bounded by a lower critical point is predicted high concentrations (Fig. 6.5b,d). For long thick rods, $L/D_{\text{thick}} \gtrsim 7$, increasing d increases the N-N stability and upon entering Region β, I-N-N coexistence capped by an upper critical point bounded N-N coexistence region is predicted in addition to the lower critical point bounded N-N region(Fig. 6.5e). With increasing d these critical points coalesce forming a single N-N coexistence region (Region γ, Fig. 6.5f). For short thick rods, $L/D_{\text{thick}} \lesssim 7$, Region β is bypassed, and the lower critical point bounded N-N region coalesces with the I-N transition creating an I-N-N coexistence region (Region γ, Fig. 6.5c).

The phase diagram in Region γ is qualitatively similar to that predicted by the second virial theory [8] for $d > 4.3$ (Fig. 6.6a), and is experimentally observed for $d \geq 3$ (Fig. 6.4a). Surprisingly, the phase diagrams in regions α and β, are not predicted in the second virial limit ($L/D- > \infty$) [8]. Upper critical point bounded N-N coexistence is predicted at the second virial limit for $3.8 < d < 4.3$ (Fig. 6.6c), similar to Fig. 6.5e, but lower critical point bounded N-N coexistence is not [8], as it is unstable in favor of a nematic-smectic or nematic-columnar transition [118]. The stability of the N-N demixing with respect to nematic-smectic or nematic-columnar transitions was not included in the Parsons-Lee theory. Additionally, Fig. 6.6d is qualitatively similar to Fig. 6.5b and d at low concentrations, but again does not predict the N-N coexistence at high concentrations. However, it is precisely this lower critical point bounded N-N coexistence which is experimentally measured in Figs. 6.4b and 6.4c for $3 > d > 2$. Simply by extrapolating between the Onsager limit ($L/D \rightarrow \infty$) and the Carnahan-Starling sphere limit ($L/D \rightarrow 1$) [113], Parsons-Lee scaling [105] qualitatively reproduces the experimental phase diagram for $3 > d > 2$ whereas the second virial limit ($L/D \rightarrow \infty$) alone does not.

Though our experimental rods have an $L/D_{\text{thick}} = 24$ we do not observe a lower critical point at intermediate d, as predicted, but instead the experimental phase behavior qualitatively follows the phase behavior predicted for short rods, $L/D_{\text{thick}} \lesssim 7$. It has been shown via simulations that the excluded volume of a flexible rod

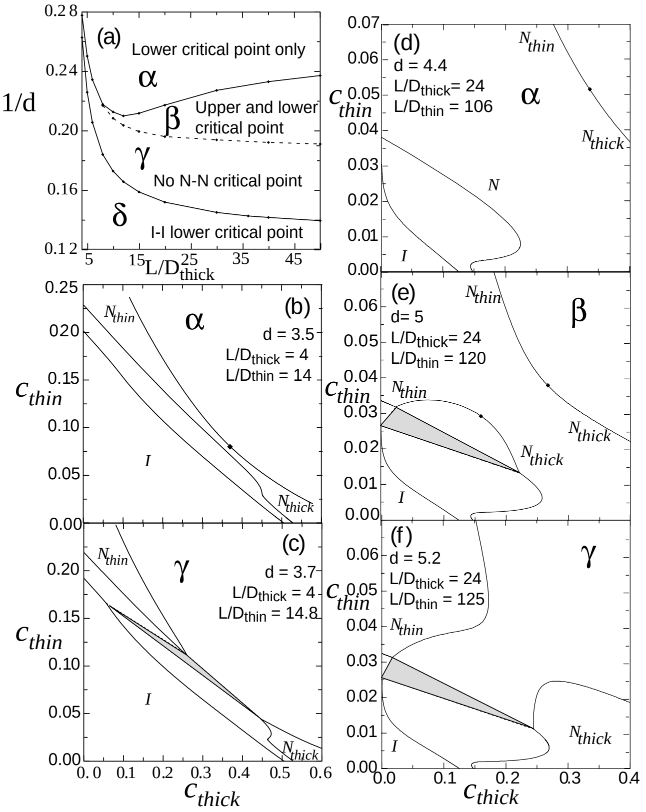

Figure 6.5: Characterization of the Parsons-Lee theoretical phase diagrams for rods of equal length and varying diameters. (a) Characterization of stable phase diagrams as a function of $1/d$ and L/D_{thick}. With increasing d, N-N coexistence becomes increasingly stable at lower concentrations (lower pressures). I-N-N coexistence occurs below the uppermost line. Coalescence of the upper and lower critical points occurs below the dashed line, and I-I-N coexistence becomes stable below the lower line. For $L/D_{\text{thick}} < 7$, the lower critical point joins with the I-N coexistence at the uppermost solid line. The theoretical phase diagrams calculated using Parsons Lee scaling are shown for $L/D_{\text{thick}} = 4$ for $d = 3.5$ (b) and $d = 3.7$ (c), and for $L/D_{\text{thick}} = 24$ (experimental aspect ratio) for $d = 4.4$ (d), $d = 5$ (e), and $d = 5.2$ (f). Phase diagrams are presented as a function of reduced concentration $c_i = v_i N_i / V$. The three phase coexistence region is indicated by the grey triangle.

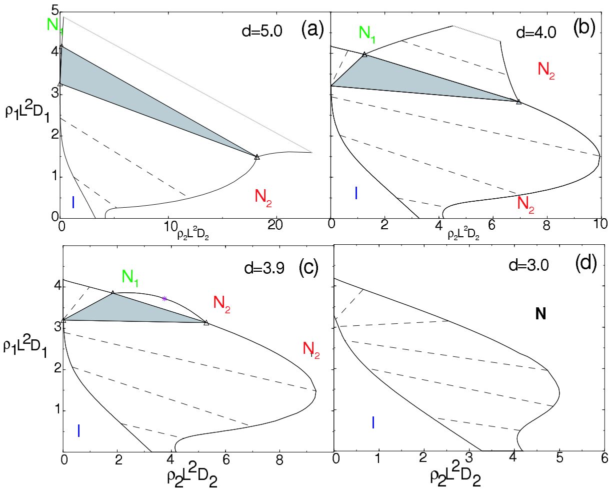

Figure 6.6: Theoretical phase diagrams in the Onsager limit as calculated by van Roij *et. al* [8] for mixtures of thin and thick rods with (a) $d = 5$ (b) $d = 4$, (c) $d = 3.9$ and (d) $d = 3$. Concentrations are presented in units of $\rho_i L_i^2 D_i$. At high concentrations the nematic-nematic coexistence is bounded by an upper critical point for $3.8 < d < 4.3$.

is equivalent to the excluded volume of a shorter-thicker rod [119]. Thus it is not entirely unexpected that our experimental results for mixtures of semiflexible rods are similar to theoretical predictions for short rigid rods. Looking further at the qualitative agreement between experiment and theory we find that the experimental I-N-N coexistence is stable to much lower diameter ratios, $d \sim 2$, than predicted. The non-additivity of the thin-thick interparticle interaction can account for some of this discrepancy as this results in an effectively smaller thin-rod diameter (larger d). For $d < 2$, N-N coexistence is no longer experimentally observed, though it is theoretically predicted in Varga's theory. This is because the N-N coexistence region moves to increasingly high concentrations as d decreases. Eventually the nematic-smectic transition will precede the N-N phase separation, and thus N-N coexistence will not be observed experimentally.

6.6 Conclusions

We have presented quantitative measurements of the phase behavior of mixtures of semiflexible thin (*fd*) and thick rods (*fd*-PEG) and have shown that isotropic-nematic, isotropic-nematic-nematic and nematic-nematic phase separation occurs in these suspensions with increasing concentration. Onsager's second virial theory for hard-rigid rods qualitatively reproduces the main features seen in our experimental bidisperse mixtures at large diameter ratios, but does not accurately capture the evolution of nematic-nematic coexistence with decreasing diameter ratio. Using the Parsons-Lee scaling of the free energy for hard-rigid-rods [105], we proposed an evolution of the bidisperse phase diagram with changing diameter ratio which indeed qualitatively describes the observed binary phase behavior. We have shown theoretically that an isotropic-nematic-nematic coexistence region is not required for the existence of a stable nematic-nematic coexistence region, in agreement with experimental observations. The existence of an upper critical point, which is predicted for very long rods by both theories, has not yet been observed. Our experimental results for long semiflexible rods most similarly follow Varga's theory for very short rods, where no upper critical point is predicted. Perhaps mixtures of longer, more rigid rods, will exhibit this upper critical point. We now have an experimental system in which we can systematically vary the diameter and length ratios from $1 < d < 5$ and $1 < l < 3$, respectively inviting further studies into the presence of an upper critical point bounded nematic-nematic region in bidisperse mixtures, as well as investigation into tri-disperse and quantitatively polydisperse rod mixtures.

6.7 Appendix: Mixtures of rods of different lengths and diameters

To further our understanding of the N-N coexistence region we investigated the stability of nematic-nematic coexistence in suspensions of rods of different diameters and lengths. These measurements were made to find the limits of diameter ratio d and length ratio l below which nematic-nematic coexistence was not experimentally measurable as a preliminary screening for investigation into the presence of an upper critical point bounded nematic-nematic coexistence region.

As mentioned in Chapter 2 we have the ability to create virus mutants of multiple lengths [37]. These length mutants are identical in structure to M13 virus, but vary in contour length and correspondingly, molecular weight (M) by $M = M_{wt}L/L_{wt}$ [37, 44]. Note that M13 virus is identical to *fd* virus accept for one amino acid per coat protein; the asp_{12} in *fd* is converted to asn_{12} in M13. The two particles otherwise share same length, diameter, persistence length and molecular weight. The length of the M13 virus particles is varied using the well established phagemid technique described in Chapter 2. For this experiment we use four M13 virus particles of lengths 0.39μm, 0.64μm, 0.88μm and 1.2μm.

As in the *fd* mixtures, bare virus will be our thin rods and virus coated with PEG will be our thick rods (both of arbitrary length ratio). The diameter ratio of the thin and thick rods was varied by varying the ionic strength of the solution, and subsequently the electrostatic effective diameter of the thin rods. To create a sterically stabilized thick rod, we again use an SSA-PEG20K to bind to the amine groups which are accessible on the virus surface. However, compared to *fd*, M13 contains an additional amine group (the functional group of the asparagine (asn) is an amine) to which our SSA-PEG20K can bind. Subsequently, approximately 600 PEG20K are attached to each M13, compared to 200 for *fd*, as determined by measurements of the

L [μm]	ρ_i [mg/ml]	$b_{\text{eff}}c_i$	D_{eff} [nm]
1.2	4.5 ±0.1	5.6	40
0.88	4.6 ±0.1	5.0	49
0.64	6.2 ±0.1	4.5	45
0.39	8.2 ±0.1	4.0	49

Table 6.1: Table of measured isotropic coexistence concentrations (ρ_i) and calculated effective diameters D_{eff} for M13-PEG virus of varying length L. The values for $b_{\text{eff}}c_i$ were obtained numerically by Chen [23] for semiflexible rods with a persistence length of 2.2 μm.

differential index of refraction dn/dc as previously described [38]. The effect of this high number of bound PEG molecules is easily observable in the isotropic-nematic coexistence concentrations of the monodisperse M13-PEG and mutant-PEG suspensions which are presented in Table 6.1. From the isotropic coexistence concentrations in Table 6.1 the effective diameter of these rods was calculated to be $D_{\text{thick}} = 46 \pm 4$ nm using the equation $b_{\text{eff}}c_i = \frac{\pi}{4}D_{\text{eff}}L^2N_i/V = 25.4\rho_i[\text{mg/ml}]L[\mu\text{m}]D_{\text{eff}}[\mu\text{m}]$, where ρ_i is the measured isotropic coexistence concentration in [mg/ml] and $b_{\text{eff}}c_i$ is the predicted isotropic coexistence concentration for semiflexible rods with a persistence length $P = 2.2\mu$m as determined by Chen [23].

In Fig. 6.7 we present a plot which shows the length and diameter ratio of binary mixtures of rods which either do or do not exhibit nematic-nematic coexistence. Nematic-nematic coexistence was either observed in bulk, or when the diameter ratio was small, microscopically. The mixture was determined to be single phase if nematic-nematic coexistence was not observed, even at very high concentrations. If nematic-nematic coexistence was not observed at high concentrations we suggest that the N-N lower critical point, as predicted by the Parsons-Lee theory, was at concentrations above which the mixed samples could be concentrated by centrifugation at 200 000 g.

We plot our experimental results with Hemmer's theoretical prediction for N-N stability [104]. We note that the theoretical nematic-nematic stability was de-

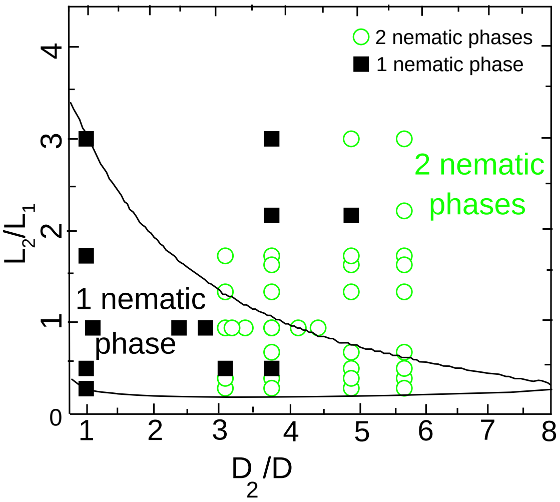

Figure 6.7: Stability of two phase nematic coexistence for rods of different diameters and lengths. The data at $l = 1$ is from the *fd*+*fd*-PEG mixtures. The data for $d = 1$ was taken using mixtures of bare M13 mutants to assure equal diameters. The open circles are where two nematic phase were observed in coexistence. The solid squares indicate that only one nematic phase was observed. We assume that for diameter ratios smaller than those which exhibited a single phase nematic point, a single phase nematic is also present. Solid line is the theoretical stability of the two phases as predicted by Hemmer [104].

termined using a Gaussian trial angular distribution function at the second virial limit of the free energy [104]. As has been shown previously [110], the use of a trial distribution function instead of numerically determining the distribution function can significantly change the predicted phase behavior. Additionally, we have shown above that the second virial approximation does not include the lower critical point bounded nematic-nematic coexistence region. Unfortunately, the N-N coexistence measured in our system is most likely bounded by a lower critical point as shown in Fig. 6.4,. Consequently, comparison with Hemmer's stability analysis can only be qualitative. As a result, it is not surprising that our experimental measurements of N-N coexistence extend to a much larger range of d and l than predicted.

Chapter 7

Nematic-Smectic transition of rod-sphere colloidal copolymers

7.1 Introduction

In the history of studying hard-particle phase behavior, both rods and spheres alike have been extensively studied. It has been shown that hard-rods can undergo a phase transition from an isotropic to a nematic phase by increasing the particle concentration [1]. Similarly hard-spheres undergo a liquid to crystal transition with increasing concentration [13]. In this chapter we theoretically explore the stability of the smectic phase of suspensions of hard-rods on which one end a hard-sphere is attached. These "lollipop" shaped particles are the hard-particle analogs of molecular amphiphiles. It has been shown previously that in mixtures of rods and unattached spheres, the spheres intercalate between the smectic layers, significantly increasing the stability of the smectic phase [120]. Additionally, theoretical models of rod-coil copolymer melts show that the presence of a coil on the end of a rod has a stabilizing effect on the smectic phase [121]. Using a model of parallel hard rod-sphere copolymers we investigate the stabilizing nature of spherical ends in a rodlike suspension.

Experimentally, colloidal particles have become the most reliable medium for studying sterically driven phase transitions as their phase behavior accurately reproduces hard-particle predictions. The challenge, however is to create rod-sphere shaped colloidal particles. In this Chapter, in addition to theoretically exploring the nematic-smectic phase behavior of ideal hard-lollipop particles, we present evidence of the feasibility of the creation of colloidal lollipop particles composed of a genetically functionalized filamentous M13 virus, for the rod component, and a functionalized polymer for the sphere component. M13 virus is known to exhibit liquid crystal phase behavior which agrees well with hard-rod predictions [14], and thus is an ideal choice for the rod-component. It is also easily end-modified. By successfully and anisotropically labelling the M13 virus with a fluorescent tag, we give evidence that synthesis of colloidal block-copolymer particles is possible.

7.2 Stability analysis of nematic-smectic A phase transition of hard rod-sphere particles

We performed a stability analysis of the smectic phase of rod-sphere particles using a similar technique to that done for suspensions of rod-sphere mixtures [120] and binary rod mixtures [122, 123, 124]. The theory we use is based on the second virial expansion of the free energy. We note that the second virial expansion of the free energy is an approximation, however it has been shown that it qualitatively describes the phase behavior observed in simulations of mixtures of rods and un-attached spheres [120]. Our theoretical system consisted of a bidisperse mixture of aligned spherocylinder-spheres. For parallel aligned rod-spheres there are only two configurations "up" and "down", and thus we can treat this as a mixture of two distinct particles. The general equation for the free energy of a bidisperse liquid at the limit of the second virial coefficient is

$$\beta F = \sum_{i=1,2} \int \rho_{\mathbf{i}} ln \rho_{\mathbf{i}} d\mathbf{r_1} \Lambda^3 - 1/2 \sum_{i=1,2} \sum_{j=1,2} \int \rho_{\mathbf{i}}(r_1) \rho_{\mathbf{j}}(r_2) f_{i,j}(r_1, r_2) d\mathbf{r_1} d\mathbf{r_2} \tag{7.1}$$

where ρ_1 is the density of “up” facing lollipops and ρ_2 is the density of “down” facing lollipops. The function $f_{i,j}(r_1, r_2)$ is the Mayer function for the hard spherocylinder-sphere particle which is equal to -1 if two particles touch and zero otherwise. The free energy can be broken down into four terms based on interparticle interactions

$$F = F_{11} + F_{22} + F_{12} + F_{21} \tag{7.2}$$

The Mayer functions for each of the four sets of interparticle interactions are f_{11}, f_{22}, f_{12}, and f_{21}. The Mayer functions are presented here, with H equal to a Heavyside function:

$$f_{11} = \begin{cases} -H[((D+d)/2)^2 - r^2 - (z-L)^2] & L < z < L + (D+d)/2 \\ & -L_(D+d)/2 < z < -L \\ -H[((D+d)/2)^2 - (r^2)] & \sqrt{(}D^2 - ((D+d)/2)^2) - L < z < 0 \\ -H[D^2 - (r^2 + z^2)] & -\sqrt{(}D^2 - ((D+d)/2)^2) < z \\ & z < \sqrt{(}D^2 - ((D+d)/2)^2) \end{cases} \tag{7.3}$$

$$f_{12} = \begin{cases} -H[(\frac{D+d}{2})^2 - (r^2)] & \sqrt(D^2 - (\frac{D+d}{2})^2) - L + \frac{D-d}{2} < z \\ & z < (D-d)/2 \\ -H[(\frac{D+d}{2})^2 - r^2 - (z - \frac{D+d}{2})^2] & \frac{D-d}{2} < z \\ & z < \frac{D-d}{2} + \sqrt(D^2 - (\frac{D+d}{2})^2) \\ -H[d^2 - r^2] & \frac{D-d}{2} + \sqrt(D^2 - (\frac{D+d}{2})^2) < z \\ & z < L + \frac{D-d}{2} \\ -H[r^2 + (z - (L + \frac{D-d}{2}))^2 - d^2] & L + \frac{D-d}{2} < z \\ & z < L + d + \frac{D-d}{2} \\ -H[D^2 - (r^2 + (z+L)^2)] & -L + \frac{D+d}{2} < z \\ & z < \frac{D-d}{2} - L + \sqrt(D^2 - (\frac{D+d}{2})^2) \end{cases} \tag{7.4}$$

In the above equations we use cylindrical coordinates (r, ϕ, z). Through symmetry $f_{11} = f_{22}$, and $f_{12} = f_{21}$. We defined the location of the center of the sphere to be also at the center of the spherical cap of the spherocylinder, thus when the diameter D of the sphere approaches the diameter d of the spherocylinder the sphere vanishes from the equations and we return to the simple spherocylinder problem. In this model L is the length from the center of the sphere to the opposite end of the cylinder, and thus the length of the "rod part" is equal to $L_{rod} = (L - D/2)$, and the total particle length is $L + D/2 + d/2$. Fig. 7.1 illustrates the shape of the rod-sphere particles.

To calculate the free energy in the nematic and smectic phases Eq. 7.1 is expanded to second order in density. Since we are interested in one dimensional layering we look at sinusoidal perturbations about a uniform density (nematic phase), or:

$$\rho_1(z) = X\rho_0(1 + a_1 \cos(kz)) \tag{7.5}$$

$$\rho_2(z) = (1 - X)\rho_0(1 + a_2 \cos(kz)) \tag{7.6}$$

where $\rho_0 = (N_1 + N_2)/V$ is the uniform density of the nematic phase of "up" and

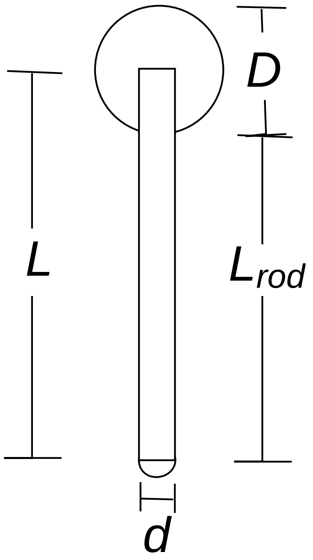

Figure 7.1: Diagram of a rod-sphere particle.

"down" particles and V is the system volume. The variable X denotes the fraction $N_1/(N_1+N_2)$ of up particles. In this calculation we assume that the "up" (1) and "down" (2) rods have the same wavelength. The difference in free energy between the smectic phase and the nematic phase is

$$dF = F(\rho_1, \rho_2) - F(X\rho_0, (1-X)\rho_0) \tag{7.7}$$

To examine the stability of the smectic phase we rewrite dF combining equations 7.1-7.7 as $dF = \mathbf{\tilde{a}Sa}$ where $\mathbf{S}$ is a two dimensional stability matrix and $\mathbf{\tilde{a}} = (a_1\ a_2)$. This relationship can be written in terms of the free energy as:

$$\det|\mathbf{\tilde{a}Sa}| = \begin{vmatrix} F_{11} - F_{11}(a_1 = 0) & F_{12} - F_{12}(a_1 = 0, a_2 = 0) \\ F_{21} - F_{21}(a_1 = 0, a_2 = 0) & F_{22} - F_{22}(a_2 = 0) \end{vmatrix} \tag{7.8}$$

When increasing concentration from the nematic phase the smectic phase becomes stable when the determinant

$$\det|\mathbf{S}| = 0. \tag{7.9}$$

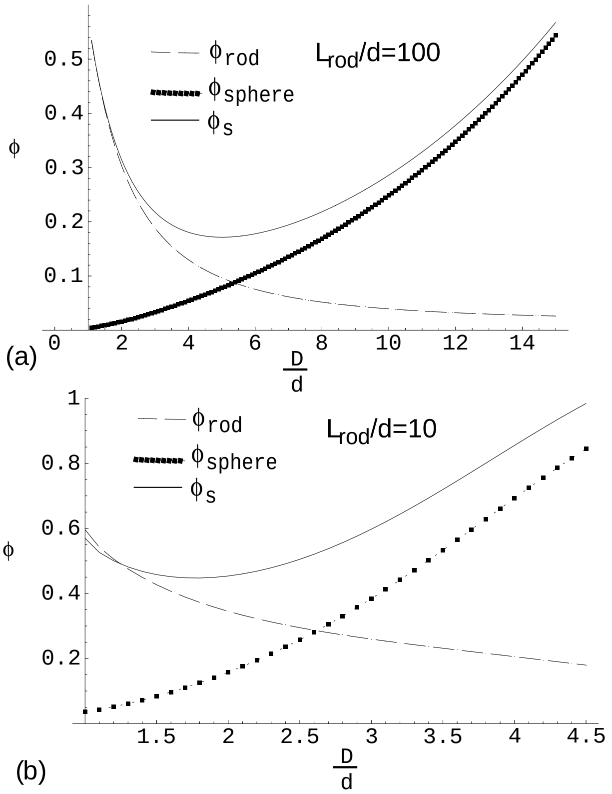

Figure 7.2: Smectic phase stability for equal numbers of up and down molecules, $X = 0.5$. $L_{\mathrm{rod}}/d = 100$ in (a) and 10 in (b). Solid line is the volume fraction of smectic phase stability ϕ_{s}, dashed line is the volume fraction due to the rod ϕ_{rod} and the dotted line indicates the volume fraction due to the spheres ϕ_{sphere}. With increasing D/d the sphere increasingly contributes to the volume fraction eventually stabilizing the nematic phase over the smectic phase.

To determine the stability diagram from the determinant, we slowly increase $\phi_s = \rho(\pi D^3/6 + \pi(L - D/2)d^2/4 + \pi d^3/12)$ for a given aspect ratio L/d and sphere to rod diameter ratio D/d. At a certain value of ϕ_s this determinant will equal zero at a non zero wave vector k_s. The lowest density for which Eq. 7.9 is satisfied is the density at which the smectic phase is stable [122]. To solve for both k_s and ϕ_s we used $d(\det|\mathbf{S}|)/dk = 0$ as our second equation. This equation is appropriate as the determinant of S is a smoothly varying function with one minimum.

7.3 Stability Results

For our stability analysis we determined the volume fraction at which the smectic phase become stable and the corresponding layer spacing for hard lollipops with rod aspect ratios of $L_{rod}/d = 100$ and 10, and for varying sphere to rod diameters (D/d). The smectic layer spacing λ remains essentially constant with changing L_{rod}/d, D/d and X and is equal to $\lambda_s = 2\pi/k_s = 1.4(L + D/2 + d/2)$.

In Fig. 7.2 we plot the minimum volume fraction at which the smectic phase of rod-sphere particles becomes stable ϕ_s as a function of the sphere to rod diameter ratio, D/d for an equal number of up and down particles, $X = 0.5$. We also plot the relative volume fractions of the rod and sphere components of the system in order to better understand the contribution of the rod and sphere to the smectic stability. We note that the volume fraction of rod-sections $\phi_{\text{rod}} = \rho v_{\text{rod}}$ is proportional to the number concentration of rod-sphere particles independent of D/d where v_{rod} is the volume of the rod section of the lollipop. We find that with increasing D/d, the volume fraction of rods and therefore number of rod-sphere particles needed to stabilize the smectic phase continuously decreases. However, only for small values of D/d does the total volume fraction decrease. As D continues to increase relative to d, the volume fraction of a stable smectic phase first reaches a minimum ϕ_{min} at a diameter ratio D^* and then begins to increase again. Comparing the stability curves for $L_{rod}/d = 100$ and $L_{rod}/d = 10$ in Fig. 7.2 a and b, respectively, we find that as L_{rod}/d decreases D^* decreases and ϕ_{min} increases. This suggests that a smectic phase of long lollipops with small spheres is much more stable than a smectic phases a system of shorter lollipops with a sphere of the same size. When the spheres are increasingly large the volume fraction of particles needed to have a stable smectic phase exceeds the volume fraction needed for simple rod-shaped particles $\phi_s > 0.57$. In this region the spheres are the dominant contribution to the volume fraction. When $\phi_s > 0.57$, the large spheres have stabilized the nematic phase in favor of the smectic phase.

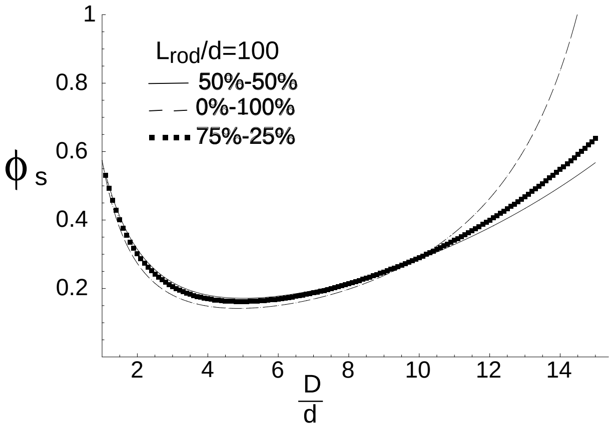

Figure 7.3: Smectic phase stability as a function of the ratio of sphere diameter to rod diameter, D/d, and the ratio of up and down lollipops, X, for hard lollipop particles with $L_{rod}/d = 100$. Different lines indicate different ratios of up and down molecules.

In Fig. 7.3 we show that changing the ratio of up and down facing particles has a significant effect on the stability of the smectic phase. At high D/d the nematic phase quickly becomes more stable than the smectic phase when the system is rich in up or down particles. Having a system of lollipops which is predominately up or down is highly unfavorable entropically as the excluded volume between like-oriented particles is much larger than the excluded volume between up and down particles. Experimentally, lollipops would most likely be evenly distributed in steeply peaked orientational distributions about both the "up" and "down" directions.

These results are consistent with the stability analysis of the lamellar (smectic phase with spheres intercalated between the layers) phase of mixtures of rods and spheres [120] which predicts that in a mixture of rods and spheres, the smectic phase becomes increasingly stable with increasing sphere diameter until a certain diameter ratio($D^* \sim 10$ for $L_{\mathrm{rod}}/d = 100$) at which point the large sphere size similarly begins to destabilize the smectic transition [120]. The value of D^* for rod-sphere mixtures also decreases with L_{rod}/d. For very large spheres, the rod-sphere mixtures demix creating a rod-rich phase and a sphere-rich phase. This however, is not possible in our lollipop particle system, as the rod and sphere are rigidly connected. We note that is possible, however, for the “up” and “down” lollipops to demix. This was also investigated. Demixing is defined to occur when the wavelength of the layer approaches infinity, alternately when $k_s \rightarrow 0$. We find that for the condition $k_s = 0$, there are no stable phase transition concentrations, indicating that there is no demixing of “up” and “down” lollipops. As demixing is not an option, the lollipop particles in this stability analysis will prefer a nematic phase if the sphere is large as the packing of lollipops with large spheres into smectic layers is very costly entropically.

7.4 Bio-chemical synthesis of colloidal rod-sphere particles

Experimentally, we propose to create colloidal rod-sphere copolymers using a single semiflexible rodlike bacteriophage, M13-C7C, as the rod component and a coiled water soluble polymer as our sphere component. This rod-component phage is grown from the New England Biolabs Ph.D.-C7C Phage display peptide library kit (New England Biolabs, Beverly MA). Its physical characteristics include its length $L \sim 1\mu$m diameter $d = 6.6$ nm and persistence length $P = 2.2$ μm. M13-C7C is nearly identical to M13 virus in structure except for an alteration in the minor coat protein P3 located on the infective end of the virus. Altering the P3 protein allows for the creation of unique binding sites located on only one end of the M13 virus. A schematic of an M13-C7C virus is shown in Fig. 7.4. The P3 protein in M13-C7C has an additional 13 amino acids inserted before its terminal amine: Gly-Gly-Gly-Ser-Cys-X-X-X-X-X-X-X-Cys-NH_2, where the X’s are seven random amino acids. The use of the C7C peptide sequence is ideal because it contains an accessible disulfide bridge formed by the sulfur molecules in each of the two Cysteines (Cys). This allows us to bind any sulfur-reactive polymer to the P3 proteins on M13. Using the C7C library instead of

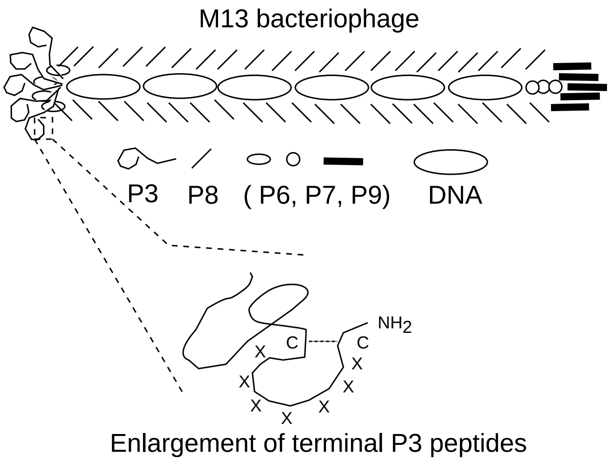

Figure 7.4: Schematic diagram of M13 phage, with enlargement of the P3 terminal amino acids showing the C7C arrangement and disulfide bridge.

a linear amino acid library is necessary as it has been shown that an odd number of Cysteines in the P3 protein renders the phage non-infective.

To produce the M13-C7C phage we followed the protocol in the Ph.D.-C7C^{TM} Phage Display Peptide Library Kit Instruction Manual (v2.8) from New England Biolabs(Beverly MA), making the changes indicated in the Appendix. The resulting phage are then sequenced to ensure the presence of the peptide insert. Typically, the correct sequence is obtained for one out of three Liters grown. Contamination of the C7C-phage solution by any wild-type virus (like *fd* or M13) results in rapid growth of the wild-type phage and minimal growth of the C7C-phage. Because the peptide expression is on the P3 protein, which is also responsible for viral infection, M13-C7C grows at a rate much slower than the wild-type. Typical yield for one Liter of media is about 5-10 mg M13-C7C.

Accessibility and reactivity of the disulfide bridge was tested by multiple methods culminating in the use of a Fluorescein-5-Maleimide fluorescent dye molecule as our sulfur-label. To bind the Fluorescein-Maleimide to the M13-C7C phages, the phage was dialyzed to a 50 mM Tris buffer at pH 7.2. Maleimide binds to sulfurs, but also has non-specific amine binding at higher pH. Since all of the coat proteins along the length of the phage have terminal amines, we wanted to minimize the possibility of non-specific binding by working at pH 7.2. After dialysis, the disulfide-bridge is reduced using a molar excess of TCEP (tris(2-carboxyethy)phosphine) and Fluorescein-5-Maleimide dissolved in Dimethylformamide (DMF) is added to a $\approx$1 mg/ml solution of M13-C7C. Measurements of the fluorescent dye binding by absorption spectrophotometry techniques was not possible as the concentration of dye molecules (not more than 10 per virus) was below the resolution of the spectrophotometer. Confirmation of the reaction was achieved by observing the smectic phase of the M13-C7C rods under fluorescence microscopy. Fluorescent dye is present between the smectic layers, but not within the layers as can be seen in Fig. 7.5. For comparison a differential interference contrast image of the same smectic sample. Had there been non-specific binding of the Fluorescein-5-Maleimide along the length of the phage, the fluorescence image would show uniform fluorescence and not the modulation shown in Fig. 7.5.

To create the rod-sphere copolymers, we initially used a Maleimide functionalized 20,000 molecular weight poly(ethylene glycol), or PEG20K-Maleimide. The reaction process is the same as described above for attaching Fluorescein-5-Maleimide to the Cysteines. The formula relating the molecular weight of PEG to its radius of gyration(R_g) is $R_g = 0.215(MW)^{.583}$Å[125]. The diameter of the PEG20K sphere is calculated to be $\sim$14 nm, about twice the bare diameter of the rods. Again using the smectic layers as a technique for detection of these spheres, we predict that the layer spacing should increase by about $\sim$ 14 nm, which is about 1.5%. Unfortunately, detection of a 1.5% layer spacing difference is nearly impossible as a single smectic layer spans only about 11 pixels on our CCD camera (Retiga EXi QImaging). Consequently we were unable to resolve the effects of the polymer binding on the smectic layer spacing. In the future addition of larger polymers would allow for better resolution of any changes in layer spacing.

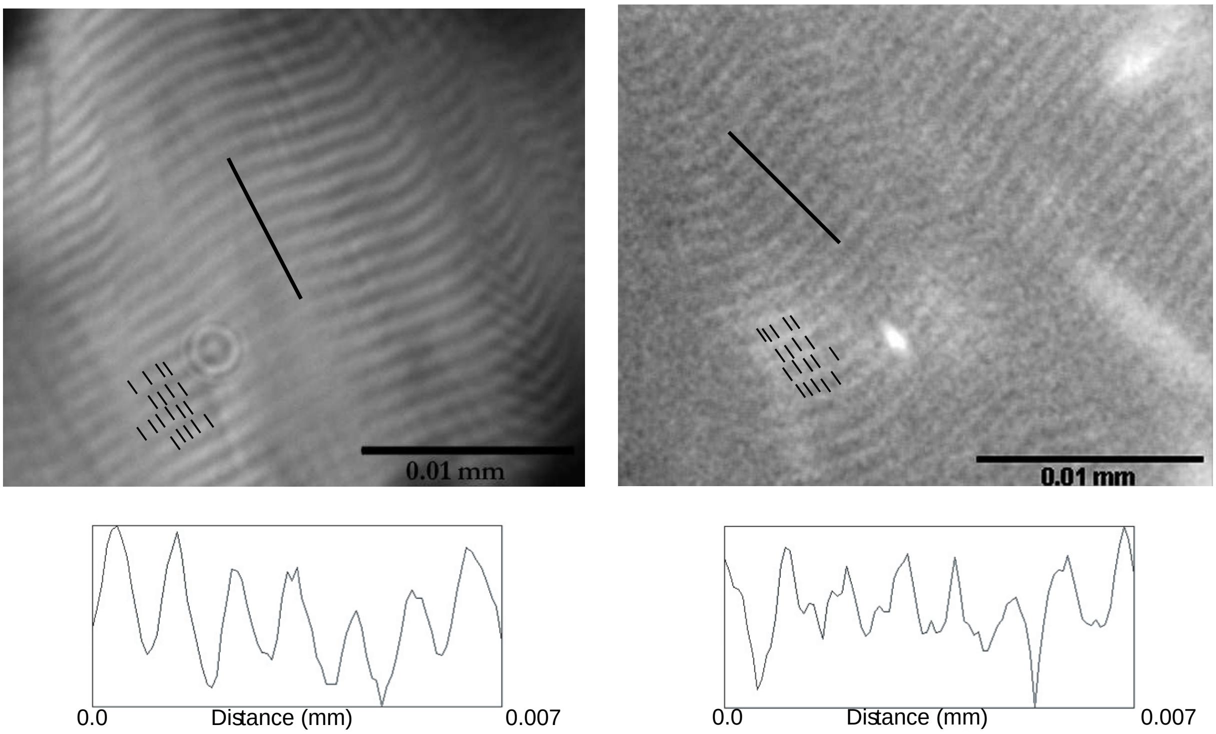

Figure 7.5: Left: DIC image of smectic layers of M13-C7C-Fluorescein suspension. Right: Fluorescence image of smectic layers of M13-C7C-Fluorescein suspension. Graphs below images represent respectively, the density and fluorescence modulation perpendicular to the smectic layers as indicated by the line drawn on the images.

7.5 Discussion

We have shown theoretically that attaching a small hard sphere to one end of a hard rod significantly increases the stability of a smectic phase of parallel hard rod-sphere copolymers. However, with increasing sphere size the smectic phase becomes increasingly unstable such that above a critical sphere size, which depends on rod length ($D/d > 15$ for $L_{rod}/D = 100$) the smectic phase is actually less stable with spheres than without. We note that previous studies of similar systems, rod-coil di-block copolymer melts ($\phi = 1$), have shown that for large polymer fractions (equivalent to large spheres in our model) the copolymers favor a smectic C phase, in which the rod part of the copolymer is tilted at an angle θ with respect to the smectic layers [126, 121, 127, 128], over a smectic phase of rods exactly perpendicular to the layers (Smectic A). Smectic C phases have been seen in simulations of di-block copolymer melts ($\phi = 1$) [129] and of polymer-nanorod copolymers ($\phi < 1$) [130]. In both these simulations the rigid-rod segment was approximately equal in length to the polymer segment. Theoretical analysis of the smectic C phase stability for colloidal particles, beyond our current simple stability analysis, may reveal a stable smectic C phase, perhaps in the region of the stability diagram where ϕ_s begins to increase and the smectic A becomes increasingly unstable, at large sphere diameters (large D/d).

Experimentally, we have only begun the process of creating rod-sphere colloidal particles. There is a wealth of polymeric material which can be functionalized to attach to the Cysteine functionalized M13 virus. DNA, for example can be functionalized with an amine containing nucleic acid. A simple crosslinker could bind the virus to the DNA creating a simple technique to vary the size of the "sphere" component. It is also possible to chemically modify polystyrene spheres to bind to M13-C7C. Experiments to perfect both these chemical reactions are currently underway. Once we have these colloidal copolymers, we can compare their experimental phase behavior to the predictions presented above. The two most obvious parameters to tune would be the diameter of the sphere (or rod), or the associative properties of the sphere (or rod). Changing the diameter of the sphere (changing the length of the polymer) can alter the stability of the smectic phase by changing the nematic-smectic transition concentration. By tuning the repulsive or attractive properties of the two independent parts, (perhaps by suspending the copolymer in a solution in which the “spherical” polymer is in a bad solvent), it may be possible to create colloidal micelles in the extreme limit, or to simply tune the stability of the smectic phase. Additionally, having end-functionalized virus allows for the creation of hard particles of many other shapes, rod-rod dimers, rod-polymer-rod tri-block copolymers, and even star shaped particles where many rods bind to one small sphere.

Appendix A

Growth of *fd* and Other Mutant Viruses

In this appendix we present a condensed protocol of the molecular biological and chemical protocols commonly used to produce the materials discussed in this thesis. Protocols included in this appendix include the procedures to grow large and small amounts of *fd*, M3, M13K07, phagemid virus of different length, and M13-C7C from a phage display library. Protocols are also included for dialysis, agarose gel electrophoresis, and chemical modification the virus. Extensive descriptions of these protocols are available in *Molecular Cloning* [36], and the *Phage Display Peptide Library Kit Instruction Manual* (v2.8) from New England Biolabs.

A.1 Preparation wild-type bacteriophage M13, fd, M13K07(from Maniatis[36])

A.1.1 Recipes for LB Media and Agar Plates

LB Media (from Maniatis p. A1)

1. Add to 950ml filtered H_2O:

10 g bacto-tryptone

5 g bacto-yeast

7.5 g NaCl

2. Dissolve solutes by stirring. After dissolved, adjust volume to 1 L with more filtered water.

3. Sterilize by autoclaving for 20 minutes.

Preparation of Agar Plates(from Maniatis p. A4)

1. Prepare LB media and add the following agar before autoclaving:

15 g/L bacto-agar (for plates)

2. Sterilize by autoclaving for 20 minutes.

3. Let solution cool after autoclaving, and then pour media solution into ~20 sterile plates/L. After plates have cooled, invert them to prevent condensation from dripping on hardened agar.

4. Let plates sit out overnight. This will allow time for any plates that have been accidentally contaminated to begin to grow impurities. Discard any impure plates, and store the remaining plates inverted at 4^oC. Plates are good for 1-2 months.

Preparation of Stock Supply of Top Agar

1. Prepare LB media and add the following agar:

7 g/L bacto-agar (for top-agar)

2. Heat the solution until Agar is completely dissolved, then place 3 ml of the solution in a series of test-tubes.(For an easy way to heat and dissolve agar autoclave the solution for 20 min. Note, that you will still need to autoclave the solution again after placing solution into test tubes)

3. Sterilize by autoclaving test-tubes for 20 minutes.

4. After the agar solution has cooled, the test tubes can be stored indefinitely in the refrigerator.

A.1.2 Step 1: Plating Bacteria: JM101 or XL1-Blue

Bulk bacteria JM101 and XL1-Blue are located in the deep freezer in the basement of Rosenstiel. JM101 grows quickly and is good for making batches of wild-type virus *fd* M13, and M13K07. XL1-Blue grows slower but when growing mutant virus strains the level of polydispersity is less. If all of the plates of bacteria within the lab are old (ie. single colony does not grow in 3mL sterile LB media when incubated overnight at 37^{o}C) or infected, new plates of bacteria must be streaked.

1 Prepare Plates of LB media A.1.1.

2. Using sterile wooden sticks, touch bulk frozen bacteria. **Gently** streak this bacteria onto sterile plate in a zig-zag motion, filling ∼1/3 of the plate. Using a different sterile stick, zig-zag through the first set of streaks into the second 1/3 of the plate. Zig-zag through the second set of streaks with a new sterile stick to fill the third 1/3 of the plate. Make 2 or 3 new plates.

3. Incubate overnight at 37^{o}C. These plates are good for about a month, after which the percent of living cells decreases rapidly. Be sure to label plates with date and type of bacteria. To prevent evaporation seal the edges of the plates with parafilm.

A.1.3 Step 2: Plating Virus-Infected Bacteria (JM101 or XL1-Blue infected with *fd*, M13 or M13K07)

If there is no fresh stock solution of virus (M13, fd or M13K07) (Preparation of this stock solution is described in A.1.4). The technique described in this section will provide you with plaques of bacteria which have been infected with the virus you added. These plaques can then be used for amplification (ie. in creation of the stock solution described in (A.1.4)). If a fresh stock solution exists it can be used for large scale virus growth or new plates and new infecting batches of virus can be made using this technique. If there is no stock solution at all it must be obtained from an outside source.

1.(AM) Grow a Small Quantity of Bacteria in Solution

1. Prepare 1-2 test tubes of 3 mL of sterile LB media.(Flame mouth of LB container before pipetting liquid from bulk. Flame vial mouth before and after LB is added, to ensure sterility.)

2. Inoculate each test tube with a colony of bacteria from previously prepared plates (section A.1.2) by touching the colony with a sterile wooden stick. Swirl tip of infected stick in the test tube briefly, then flame mouth of the test tube and recap.

3. Incubate in an agitator at 37^oC for 6-10 hours until turbid.

2. Titrate Existing Virus Solution

If bulk solution of wild-type virus as described in A.1.4 exists prepare a series of tenfold dilutions of the bacteriophage to 10^{-11} of the original concentration. Dilute 100μl of the stock solution with 900 μl H_2O, mix and repeat dilution. You should end up with a series of solutions of concentrations $10^{-1}, 10^{-2}...10^{-11}$. Use these one of these for each plate. If this bulk solution does not exist or is too old to trust titrate from stock located in freezer (stock labeled in pfu's, titrate down to ~1 pfu). *pfu=Plaque forming unit.

3. (PM) Mix Bacteria and Virus in Top Agar and Plate

1. Prepare top agar fresh in test-tubes(A.1.1), or thaw pre-made test tubes of agar in beaker of water which is brought to boil. Keep agar warm (45-50^o C) in temperature controlled environment (typically a heating block with a test-tube holding rack installed).

2. Into one test-tube of melted top agar add 100 μl of a virus solution and 300 μl of the bacteria solution. Gently swirl mixture, and then quickly pour mixture onto media plates which have been brought to room temperature. Repeat this for each of the different concentrations of titrated virus. Be sure to flame all test tubes every time they are opened and closed. The only exception being after you add the last component to the top agar do not flame the test tube. Occasionally flaming immediately before you pour the top agar onto the plates will kill the bacteria as you pour out the agar because the glass is still too hot.

3. Incubate plates overnight. Keep plates containing small single plaques. These plates should contain $\sim$1 pfu. The plaques of virus infected bacteria are used when making large quantities of virus.

A.1.4 Step 3: Small Scale Amplification, Making the "Infecting Batch" of Virus from a Plaque

1. Take 50 ml of sterile LB and inoculate it with 1 or 2 plaques of bacteria infected with the virus from plates made in section A.1.3. This is usually done by stabbing plaque with a glass pipette tip which has been sterilized by dipping in alcohol and flaming and then releasing the clump of infected media into the LB.

2.Agitate in an incubator at 37^{o}C overnight.

3.Remove turbid solution of infected bacteria from incubator and pour into sterile centrifuging vial. Spin at 3300 g (4000 rpm in Sorvall RT-7 with RT-750 rotor) for $>$ 30 minutes.

4. Pour supernate of virus solution into sterile vial with purple lid. Refrigerate at

4^oC until needed for use.

A.1.5 Step 4, Day 1: Large Scale Wild-type Virus (*fd*, M13 or M13K07) Amplification

Day 1 AM: Prepare a Small Quantity of Bacteria in Solution

1. Prepare 1 test tube of 3 mL of sterile LB media for each of the 3 L of LB media you plan to infect.(Flame mouth of LB container before pipetting liquid from bulk. Flame vial mouth before and after LB is added, to ensure sterility.)

2. Inoculate each test tube with a colony of bacteria from previously prepared plates (section A.1.2) by touching the colony with a sterile wooden stick. Be careful not to breathe on the open plates. Swirl tip of infected stick in the test tube briefly, then flame mouth of the test tube and recap.

3. Incubate in an agitator at 37^oC for 6-10 hours until turbid.

4. Prepare 3 liters of sterile LB media(A.1.1) for each test tube of bacteria you are growing. Placing ∼700ml in in a 2L flask.

Day 1 PM: Infect X liters of LB 1. Infect each 2L flask with $\sim 0.7ml$ of bacteria. Incubate and agitate until slightly turbid,∼3 hours.

2. After 3 hours, add 0.5ml infecting batch virus as prepared in A.1.4 to each 2L flask and incubate for another 6-10 hours, or overnight.

A.1.6 Step 5, Day 2: Purification of Virus

1. Pour turbid solution of bacteria and virus into large centrifuge jars. Centrifuge at 3300 g for >30min. Keep supernate.

2. Add 20 g/L PEG 8000 and 20 g/L NaCl to the supernate. The solution should become slightly turbid as it is mixed. This is due to the condensation of the virus particles from the depletion by the PEG. Respin this solution at 4000 rpm (3300 g)

for another 30-45 minutes.

3. On the bottom of the centrifuge jars should be thick concentrated virus and polymer mixture. Dissolve it with $\sim$3 ml of distilled H_2O. Pipette off as much virus solution as possible and transfer it to the $\sim$ 50 ml Sorvall centrifuge containers (round bottom, purple lid).

4. Yield at this stage should be approximately 10-100mg/L depending on the freshness of the bacteria and virus solutions used.

5. To continue purification, spin concentrated virus solution at $\sim$20000 g (13000 rpm in Sorvall centrifuges on 3rd floor Rosenstiel) for $>$ 45 minutes. Keep supernate, and check for virus in supernate by spectrophotometry. If virus is not present in large quantities sediment should be diluted and spun again. Otherwise the sediment can be discarded.

6. Spin virus solution again at 13000 rpm (20000 g) for $>$ 45 minutes.

7. Spin virus at $\sim$250000 g for 3 hours (50000 rpm LE 80 or LE 70 Beckmann centrifuge using Ti 70.1 rotor). Carefully discard supernate (which should contain only polymer and other unwanted contaminants). Dilute virus with buffer or water(approximately 500 μl), and let resuspend overnight (vortex thoroughly to aid in resuspension).

8. At this point in the purification process virus should be dialized against a buffer (see A.4.1) before continuing on to the final step.

9. Spin virus down again at $\sim$250000 g for $>$2 hours, and remove the supernate afterwards. Add just enough buffer to resuspend virus to concentration of a smectic ($\sim$ 200μl).

A.2 Mutant Virus Preparation (Production of Litmus or PGTN28 phagemid)

In order to grow viruses of different lengths other than the wild-type virus, it is necessary to approach the virus preparation with a different method. First, a stock solution of the helper phage (M13K07) must be made. Second, the plasmid DNA which will later be made into a complete virus has to be introduced into the bacteria by shocking the cells. The plasmids are chosen to contain a resistance to both ampicillin and kanamycin. This helps to ensure that only the bacteria containing the plasmids reproduce when they are allowed to grow. After the plasmids are in the bacteria's DNA, the helper phage is introduced. The helper phage will create the protein coat for the plasmid DNA, creating a new virus containing only the new plasmid DNA. The resulting virus is our new"mutant virus."

A.2.1 Solution Recipes

-LB Media: Mix 1L distilled H_2O, 10 g bacto-tryptone, 5 g bacto-yeast, 7.5 g NaCl. Sterilize by autoclaving for 20 minutes.

-LB Plates: 1L distilled $\mathrm{H_2O}$, 10 g bacto-tryptone, 5 g bacto-yeast, 7.5 g NaCl, 15 g/L bacto-agar. Sterilize by autoclaving for 20 minutes. After autoclaving, pour warm media solution into ~20 sterile plates/L. After plates have cooled, invert and let sit out overnight to check for accidental contamination. Discard any impure plates, and store the remaining plates inverted at 4^oC. Plates are good for 1-2 months.

-$\mathrm{CaCl_2}$ buffer: 60 mM $CaCl_2$
15% glycerol
10 mM pipes + NaOH to PH 7
filter into sterilized jar and store at 4^oC.

-Ampicillin Stock: 5 mg/ml Ampicillin in $\mathrm{H_2O}$ for plates, 50 mg/ml Ampicillin in

H_2O for growth in liquid media.

-Kanamycin Stock: 25 mg/ml Kanamycin in H_2O

A.2.2 Step 1: Prepare Competent Cells of XL1-Blue(from Maniatis p. 1.83)

1. Take 100 ml sterile LB and inoculate with XLI-Blue bacteria by touching a colony from a plate as prepared in A.1.2.

2. Incubate ∼6 hours at 37^oC. Then transfer liquid into 50 ml sterile centrifuge containers.

3. Ice solution for 10 minutes . Spin down bacteria at 3300 g (4000 rpm with Sorvall RT 7 centrifuge) for 10-15 min at 4^oC. Decant liquid (pour off) and invert containers for 1 minute.

4. Resuspend bacteria in 10 ml of $CaCl_2$ buffer.

5. Recentrifuge at 3300 g for 10 minutes at 4^oC. Decant liquid and invert containers for another minute.

6. Add 2 ml ice cold $CaCl_2$ buffer for each 100 ml of original solution.

7. Dispense solution of cells into 10 0.5 ml sterile microcentrifuge tubes. Freeze at -70^oC.

A.2.3 Step 2: Insert Plasmid into Competent Cells and Plate (from Maniatis p. 1.82)

1. Obtain a microcentrifuge tube with 200 μL of competent cell solution (A.2.2) from storage and keep it on ice. Add 50ng/10μl (= 1 μl DNA/10 μl water) of plasmid DNA to each tube. Mix by gently swirling. Store on ice for 30 minutes.

2. Transfer tubes to a rack in a circulating water bath that was preheated to 42^oC. Leave tubes in for exactly 90 seconds.

3. Transfer tubes to an ice bath for 2 minutes.

4. Add 800 μl sterile LB medium to each tube. Incubate in a water bath at 37 ^{o}C for 45 minutes.

5. Coat 6 LB+agar plates (A.1.1)with 30 μl Ampicillin stock (150μg total) by using a sterile bent glass rod. A drop of ampicillin is spread over the plate by rotating the glass rod around on the surface of the plate. Rod is sterilized by dipping in alcohol and then flaming. Be sure to cool rod before placing on plate.

6. Transfer 10, 20, 50, 100, 150, or 200 μl infected competent cells onto one of each of the 6 ampicillin treated plates, respectively, by the same method above. Let the plates sit at room temperature for ~15 minutes to let the liquid absorb into the plate. Then invert and incubate plates for 12-16 hours at 37^{o}C (not more than 20 hours or ampicillin resistance increases). Plaques that form are ampicillin resistant. Chose the plates where you can see individual plaques.

A.2.4 Step 3: Prepare Helper Phage M13K07

1. Prepare plates of XLI-Blue bacteria infected with the M13K07 helper phage as described in A.1.3.

2. Prepare a stock solution of M13K07 as described in A.1.4.

A.2.5 Step 4: Large Scale Mutant Production

Day 1 AM: Prepare a Small Amount of Plasmid Containing Bacteria

1. Prepare 1 test tubes of 3mL of sterile LB media and 100μ g/ml Ampicillin (=6μl/3ml) for each of the 3L of LB media you plan to infect.(Flame mouth of LB container before pipetting liquid from bulk. Flame vial mouth before and after LB is added, to ensure sterility.)

2. Inoculate each test tube with a colony of **XL1-Blue containing the plasmid** from previously prepared plates (section A.2.3) by touching the colony with a sterile

wooden stick. Swirl tip of infected stick in the test tube briefly, then flame mouth of the test tube and recap.

3. Incubate in an agitator at 37^oC for >8 hours until growth is saturated.

4. Prepare 3 liters of sterile LB media(A.1.1) for each test tube of bacteria you are growing. Placing $\sim$ 700ml in in a 2 L flask.

Day 1 PM: Infect X Liters of LB.

1.Infect each liter with $\sim 1.0ml$ of plasmid-containing XL1-Blue prepared above, 1 ml Ampicillin stock (50 mg/ml) and 1 ml M13K07 solution prepared in A.2.4. Incubate and agitate 1 hour.

2. After 1 hour Add 3 ml kanamycin stock and incubate for another 14-18 hours.

Day 2 AM: Purify the Virus Suspension

Follow section A.1.6.

A.3 Preparation of P3 Phage-Display M13-C7C virus

M13-C7C is a M13-structured virus which has been modified to display 9 extra amino acids on the end of the P3 infective protein. It is available from New England Biolabs as the C7C Phage Display Peptide Library. The “7” refers to a random sequence of 7 amino acids. These can be specifically selected for using phage display techniques, however as we are only interested in the Cysteines surrounding the random amino acids this protocol is for simple amplification of any phage from the supplied library.

A.3.1 Solution Recipes

-LB Media: 1L distilled H_2O, 10g bacto-tryptone, 5g bacto-yeast, 7.5g NaCl. Autoclave for 20 minutes.

-LB Plates: LB Media, 15g/L Bacto-agar. Autoclave for 20 minutes. After autoclaving, pour warm media solution into ~20 sterile plates/L. After plates have cooled, invert and let sit out overnight to check for accidental contamination. Discard any impure plates, and store the remaining plates inverted at 4^{o}C. Plates are good for 1-2 months.

-LB-TET solution: LB with 1mL/L Tetracycline added after autoclaving.

-LB-TET plates: LB Media, 15g/L Bacto-Agar, Autoclave. When warm, add 1mL/L Tetracycline stock (20mg/mL in ethanol, stored at -20^{o}C). Pour cool solution into ~20 sterile plates/L. After plates have cooled, invert and let sit out overnight to check for accidental contamination. Store inverted at 4^{o}C.

-Top Agar: LB Media, 7g/L bacto-agar. Heat the solution until Agar is completely dissolved, then place 3ml of the solution in a series of test-tubes. Sterilize by autoclaving test-tubes for 20 minutes. Store in the refrigerator.

-Xgal solution: 20mg/mL Xgal in Dimethylformamide (DMF). Store in -20^{o}C freezer. (* Xgal= 5-bromo-4-chloro-3-indolyl-bD-galactoside)

-IPTG solution: 200mg/mL IPTG in dH2O; sterilize by passing IPTG through 0.22 mm filter. Aliquot to 1 ml, store -20^{o}C freezer. (* IPTG= Isopropyl-beta-D-thiogalactopyranoside)

-Sodium acetate buffer: 3M, pH 5.2

Glassware should be washed, rinsed, rinsed with ethanol, dried and then autoclaved before use!

A.3.2 Step 1: Grow ER2738 on LB-TET or LB plates

1. Prepare Plates of LB media.(LB-TET plates are recommended by New England Biolabs but we have found that this produces an abnormally large amount of impure plates and foreign growth. Growth of ER2738 on plain LB plates has shown to drastically reduce foreign grown making the plates much more stable for long periods

of time)

2. Using sterile wooden sticks, touch bulk frozen bacteria ER2738. Gently streak this bacteria onto sterile plate in a zig-zag motion, filling ∼1/3 of the plate. Using a different sterile stick, zig-zag through the first set of streaks into the second 1/3 of the plate. Zig-zag through 2nd third to fill the third 1/3 of the plate. Make 2 or 3 new plates.

3. Incubate overnight at 37^{o}C. These plates are good for about a month. Be sure to label plates with date and type of bacteria.

A.3.3 Step 2: Plating M13-C7C-Infected Bacteria

1.(AM) Grow a Small Quantity of Bacteria in Solution

1. Prepare 1-2 test tubes of 3mL of sterile LB media.(Flame mouth of LB container before pipetting liquid from bulk. Flame vial mouth before and after LB is added, to ensure sterility.)

2. Inoculate each test tube with a colony of ER2738 from previously prepared plates (section A.3.2) by touching the colony with a sterile wooden stick. Swirl tip of infected stick in the test tube briefly, then flame mouth of the test tube and recap.

3. Incubate in an agitator at 37^{o}C for 6-8 hours until turbid.

2. Titration of M13-C7C library

Prepare tenfold dilution series of M13-C7C in LB; Initial library concentration = 1x10^{13}. Dilute to 1x10^3 and plate as desired, though only concentrations ¡ 1x10^6 produce individual plaques suitable for amplification.

3. (PM) Mix and Plate ER2738 and M13-C7C

1. Prepare top agar fresh in test-tubes(A.1.1), or thaw pre-made test tubes of agar in beaker of water which is brought to boil. Keep agar warm (45-50^{o}C) in temperature controlled environment.

2. To each top agar, add 100 μL ER2738 culture (grown for 6 - 8 hrs), 10 μL virus

dilution, 40 μL Xgal, 4 μL IPTG. Be certain to pre-warm the plates. Mix by swirling. Pour top agar onto plate. After top agar has solidified incubate overnight (18 hrs **MAXIMUM**), then refrigerate. Useful plates have clearly defined blue plaques that are not in contact with each other.

A.3.4 Step 2: Small Scale Amplification of M13-C7C Plaque ("Infecting Batch")

1.(Day 1 PM) Grow a Small Quantity of Bacteria in Solution
Prepare 1-2 test tubes of 3 mL of sterile LB media. Inoculate each test tube with a colony of ER2738 from previously prepared plates (A.3.2) by touching the colony with a sterile wooden stick. Swirl tip of infected stick in the test tube briefly, then flame mouth of the test tube and recap. Incubate overnight.
2. (Day 2 AM) Prepare 20 ml Infecting Batch
Use 20 mL sterile LB media, and add 200 μL (overnight) ER2738 culture and 1 blue plaque from the plate. Incubate 5 hours on the shaker. Centrifuge at 4000 rpm for 30 min to sediment bacteria. Keep supernate by decanting into a fresh tube.

A.3.5 Step 3: DNA sequencing

1. Before bulk amplification, the virus solution must be DNA sequenced to ensure that it is C7C. To precipitate the DNA, take 400 μL of each plaque amplification solution. Add 200 μL phenol(toxic!), vortex for 1 minute, and centrifuge for 10 min. Pipette the aqueous layer to a fresh microcentrifuge tube. Add 400 μL chloroform(toxic!) to the aqueous layer, vortex for 1 minute, and centrifuge for 10 min. Pipette aqueous layer to a new centrifuge tube. Add 40 μL sodium acetate buffer. Add 1200 μL cold ethanol, vortex 1 minute. Place in freezer 20 min. to precipitate DNA, then centrifuge 20 min. to pellet DNA. Pipette off supernate, and allow to dry overnight

in the hood. Resuspend the following day in 20 μL dH_2O.

2. To measure concentration and purity, absorption must be measured. Dilute 3 μL of DNA with 400 μL dH_2O. Measure absorption at 260 nm and 280 nm; A^{260}/A^{280} must be greater than 1.5 to obtain a useful sequence. If $A^{260} = 1$, then [solution] = 50 μg/mL. Determine concentration of stock DNA solution by multiplying [diluted solution] by (400/3). For sequencing we Fed-Ex our DNA samples to Elim Biopharmaceuticals and follow their recommended sample preparation protocol. For sequencing, approximately 1 μg of DNA is required, along with 8 pmols of primer (from NEB, -96gIIIp), in a final volume of 15 μL.

3. Upon receiving the sequence, compare it to the NEB C7C kit booklet page 12; the region between restriction sites Eag I and Kpn I must exist for the sequence to be correct. Ensure that the sequence is being read in the proper direction!

Purity of M13-C7C by Agarose Gel Electrophoresis

Prepare gel for electrophoresis as in A.4.2. To run the DNA, dilute 2 μL of DNA solution to 20 μL, and add 4 μL of loading buffer for thick lane comb. If using the thin lane comb, dilute the DNA 1:10, and add 2 μL of loading buffer. Run and stain gel as described in A.4.2.

The band of M13-C7C should be slightly higher than the band for M13, as the size difference is very small, but M13-C7C is longer and should run slower. It is best to run M13, Fd, and a known sample of M13-C7C as standards for comparison.

A.3.6 Step 4: Large Scale Amplification of M13-C7C to 700mL

Day 1 PM: Grow a Small Quantity of Bacteria in Solution

Prepare 1-2 test tubes of 3 mL of sterile LB media. Inoculate each test tube with a colony of ER2738 from previously prepared plates (A.3.2) by touching the colony with a sterile wooden stick. Swirl tip of infected stick in the test tube briefly, then flame mouth of the test tube and recap. Incubate overnight.

Day 2 AM: Amplification

Once a stock solution known to contain M13-C7C is obtained, bulk amplification can begin. Prepare 700 mL of sterile LB media and add 10 mL (overnight) ER2738 solution with 500 μL virus solution. Incubate **5 hours** on the shaker. Do not incubate longer as the probability of wild-type viral growth increases with time.

Day 2 PM: Purification

Follow the same purification steps in A.1.6, but be sure to keep all virus samples separate (from each 700 mL growth), as there is no guarantee that the virus in each growth is the same (wild type or M13-C7C mutant). After virus is centrifuged at ~20000 g (13000 rpm), and the majority of the bacteria has been removed by precipitation, **the viral DNA should be sequenced again (A.3.5)**. Contamination of the M13-C7C solution by miniscule amounts of wild type M13 or fd is quite common and happens 2/3 of the time. The growth of these wild type phages is exponentially faster as the P3 (infecting protein) is not damaged. If the M13-C7C virus has grown the yield will not be very large, perhaps 20 mg/700 mL at best.

A.4 Other Techniques for Manipulating Viruses and Virus Suspensions

A.4.1 Dialysis of Virus

1. Prepare buffer to dialyze virus against. Example: To make a 1.01 M Tris-NaCl buffer:

Add 1 M NaCl and 20 mL of 1 M Trisma to 950 ml $H_2 0$ and stir until dissolved. Adjust pH to 8.15 with 1 N HCl. Ionic strength is 1.01 M (1 M from NaCl and 10 mM from 20 mM Tris).

2. Using snake skin 10000 MWCO (from Pierce), fill about 4 inches of snake skin

with virus solution which is in the isotropic phase. Make sure bottom is closed with dialysis clip. Leaving room at top of snake skin for air (~1/2 inch), close snake skin.

3. Put dialysis bag in 300-500 ml buffer and stir for at least 3 hours. Pour off buffer and fill beaker with fresh buffer. Repeat two or three times, until dialysis is completed.

A.4.2 Agarose Gel Electrophoresis

Solutions:

6x Loading Buffer: 0.25% bromophenol blue and 40% (w/v) sucrose in water.

EDTA: 186.1 Disodium EDTA$\cdot$ $2H_2O$ in 800 ml H_2O. Adjust pH to 8.0 with NaOH ($\sim$ 20 g NaOH pellets).

TAE Buffer (50x): 242 g Tris Base, 57.1 ml glacial acetic acid, 100 ml 0.5 M EDTA (pH 8.0)

Staining Solution: 45% Water, 45% Methanol, 10% glacial acetic acid and 1 g/L Coomassie blue dye

Destaining Solution: 45% Water 45%Methanol and 10% glacial acetic acid

Protein Gel Electrophoresis, Maniatis Ch 6.

1. For concentrated virus (greater than 0.5 mg/ml) prepare 20 μl virus at 0.5-0.25 mg/ml (less than 20 μg/20 μl virus put into gel well). If virus is more dilute precipitate virus first using technique in A.4.3. Add 4 μl 6x loading buffer to 20 μL aliquot of virus.

2. Prepare 1 L H_2O + 20 ml/L TAE buffer solution (1x).

3. Dissolve 0.8 g Agarose (1.0 g for less viscous fingering) in 100 ml of solution prepared above by heating.

4. Tape sides of plastic gel holder so that liquid doesn't leak out, and insert comb.

5. Cool solution and pour into plastic gel holder. When gel is solid remove tape

(accept maybe for a corner to keep gel from sliding) and comb. Put gel, in holder, into electrophoresis machine and fill with the rest of the buffer solution.

6. Pipette 10-20 μl dye+virus solution into each hole in gel. Put If using the thin lane comb, 7 μL per lane is sufficient.

Run electrophoresis for 4-6 hours, or until blue dye ran 2/3 of the length of the gel, at 50 V.

7. To stain virus gel: Stain in 200 ml staining solution for <3 hours. Destain multiple times, for up to 3-5 days using destaining solution for best resolution of the bands.

DNA Gel Electrophoresis (Maniatis p 4.29 and ch 6)

Cautions: Phenol, Chloroform and Ethidium bromide are toxic! Work in the hood, wearing gloves. Dispose of waste in proper bins.

1. Prepare gel as above, only use 1.2 g Agarose (use 1 g when looking at longer virus).

2. Phenol-Cloroform extract DNA from 100 μl of *fd* at 3 mg/ml: Add 50 μl Phenol (very toxic!), vortex for 1 minute. Centrifuge to separate solution. Transfer top (aqueous part containing DNA) to new microcentrifuge tube. Add 100 μl Chloroform. Vortex for 1 minute. Centrifuge to separate solution. Transfer top to new microcentrifuge tube.

You can use this to fill gel, or you can continue to purify the DNA with an ethanol precipitation (see below). Best DNA bands come by using the DNA from 0.06 mg virus per well.

3. Run for 4 h at 70-80 V until loading buffer band has migrated $\sim$ 2/3 of the gel distance.

4. After electrophoresis is complete stain gel with 10 μl (5 μg/ml) Ethidium Bromide (toxic!) in 200 ml H_2O for 30-45 minutes. After staining is complete rinse gel in water for 20 minutes and handle with gloves. DNA can be seen under UV light but is seen best if gel is refrigerated overnight. If the background fluorescence is still high

soak the gel in 1 mM MgSO_4 for 20 minutes.

A.4.3 General Techniques for Precipitation and Purification of Virus and Viral DNA

Solutions:

PEG-NaCl stock solution: 20 g PEG 8K and 2.5 M NaCl (14.6 g) to 100 mL H_2O (p. 4.29 in Maniatis).

Na-Acetate buffer: 3 M at pH 5.2 (adjust pH with Acetic Acid)

Virus Precipitation

Add 200 μl PEG-NaCl solution to 1ml dilute virus solution in microcentrifuge tube. Vortex. Microcentrifuge at 14000 rpm ($\sim$ 14000 g) for 20min. Pipette off liquid. Add 20 μl H_2O to pellet and vortex until dissolved.

Phenol-Choroform Extraction of DNA

Cautions: Phenol, Chloroform and Ethidium bromide are toxic! Work in the hood, wearing gloves. Dispose of waste in proper bins.

For 100 μl of *fd* at 1mg/ml add 50μl Phenol (very toxic!), vortex for 1 minute. Centrifuge (max speed on microcentrifuge $\sim$ 14000 g) to separate solution. Transfer top (aqueous part containing DNA) to new microcentrifuge tube. Add 100 μl Chloroform. Vortex for 1 minute. Centrifuge to separate solution. Transfer top to new microcentrifuge tube.

Ethanol Precipitation of DNA

To DNA solution prepared above add 10% by volume Na-Acetate buffer. Then add 3x this volume ice cold 100% Ethanol. Place the sample in the freezer for 20 min to allow DNA precipitate to form. Centrifuge max power for 10-20 minutes in the table-top centrifuge. Remove the supernate. Dry the sample COMPLETELY in air/vacuum (20 min-overnight). Resuspend in 20 μl H_2O or TE buffer (use 100 μl if purifying for electrophoresis). DNA concentration is measured at 260 nm 1. OD=50 μg/ml. Pure DNA has Absorption^{260}/Absorption^{280} > 1.8.

A.4.4 Coating Virus with Amine-binding PEG

Solutions:

Phosphate buffer: 100 mM NaCl,100 mM Na_2HPO_4(Sodium Phosphate, Di-Basic) at pH 7.8 (adjust pH with HCL)

Procedure:

1. Dialyze virus in Phosphate buffer. Do not use Tris buffer as it contains reactive amines.

2. add Polymer: 5,000 MW, SSA-PEG-5000, or 20,000 MW, SSA-PEG-20000 (stored in freezer, highly reactive with H_2O). Use an amount of PEG equal to approximately 2 polymers/ binding site ($\sim$ 2 mg-peg/mg-fd for 5K PEG and 8 mg-peg/mg-fd for 20K PEG)($\sim$3000 sites/fd). Add polymer quickly to *fd* solution as it will quickly bond with water and NOT with the virus. Let polymer mix with virus for about 1 hour.

3. While virus and PEG are reacting unused PEG should be vacuum dried. Release vacuum by filling chamber with Argon gas. Seal PEG container while it is submerged in the Argon gas, seal container with parafilm and dessicate in freezer.

4. Centrifuge virus+ polymer mixture twice at 55,000 rpm (300,000 g). Beware that resulting pellet will be very soft if polymer is attached because the polymer prevents tight pelleting.

A.4.5 Fluorescent Labelling of Virus Coat Proteins

Solutions:

Boric acid buffer: 100 mM NaCl and 100 mM Boric Acid. Adjust to pH 9.5 with NaOH.

Procedure:

1. Dialize *virus* in Boric acid buffer. If the virus was previously in a Tris buffer dialize for a long time (∼24 h) to ensure complete exchange of Boric Acid buffer for Tris buffer.

2. Dilute virus to ∼1 mg/ml or minimally to the isotropic phase.

3. For each mg of virus mix >0.65 mg FITC (such that there are ∼3-10 FITC molecules per binding site (∼ 3000 binding sites/fd)) with DMSO (Dimethyl sulfoxide). The total volume of DMSO should be 10 percent of final volume of DMSO+ virus solution (ie 0.1 mL DMSO per 0.9 mL virus sol'n).

4. Add FITC-DMSO mixture to virus solution. Reach for approximately 1 hour.

5. After reaction is complete, dialyze virus against Tris buffer until solution outside of dialysis bag is clear and no longer contains any unbound fluorescence polymers (∼ 3-5 days and many buffer exchanges). After this, labeled virus can be centrifuged 2-3 times to remove residual FITC in solution. FITC is not soluble in water alone so dialysis must be done in a buffer.

Bibliography

[1] L. Onsager. The effects of shape on the interaction of colloidal particles. *Ann. NY Acad. Sci.*, 51:627–659, 1949.

[2] M. Hosino, H Nakano, and H. Kimura. Nematic-smectic transitions in an aligned rod system. *J. Phys. Soc. Jpn.*, 46:1709, 1979.

[3] D. Frenkel, H.N.W Lekkerkerker, and A. Stroobants. Thermodynamic stability of smectic phase in a system of hard rods. *Nature*, 332:822, 1988.

[4] J. K. Percus. *The many body problem, proceedings.* Interscience Publisher, New York, 1957.

[5] B. J. Alder and T. E. Wainwright. Phase transitions for a hard sphere system. *J. Chem. Phys.*, 27:1207, 1957.

[6] P. J. Flory and A. Abe. Statistical thermodynamics of mixtures of rodlike particles. 1. theory of polydisperse systems. *Macromolecules*, 11:1119, 1978.

[7] H. N. W. Lekkerkerker, P. Coulon, V. der Haegen, and R. Deblieck. On the isotropic-nematic liquid crystal phase separation in a solution of rodlike particles of different lengths. *J. Chem. Phys.*, 80:3427–3433, 1984.

[8] R. van Roij, B. Mulder, and M. Dijkstra. Phase behavior of binary mixtures of thick and thin rods. *Physica A*, 261:374–390, 1998.

[9] M. Dijkstra and R. van Roij. Entropy driven demixing in binary hard core mixtures: From hard spherocylinders towards hard spheres. *Phys. Rev. E*, 56:5594, 1997.

[10] G. J. Vroege and H. N. W. Lekkerkerker. Theory of the isotropic-nematic-nematic phase separation for a solution of bidisperse rodlike particles. *J. Phys. Chem.*, 97:3601, 1993.

[11] G. J. Vroege and H. N.W. Lekkerkerker. Theory of phase separation for a solution of tridisperse rod-like particles. *Coll. and Surf. A*, 129-130:405–413, 1997.

[12] A. Speranza and P. Sollich. Simplified onsager theory for isotropic-nematic phase equilibria of length polydisperse hard rods. *J. Chem. Phys.*, 117:5421, 2002.

[13] W. C. K. Poon and P. N. Pusey. Phase transitions of spherical colloids. In M. Baus, L. F. Rull, and J. P. Rycaert, editors, *Observation, Prediction, and Simulation of Phase Transitions in Complex Fluids*, pages 3–51. Kluwer Academic, Dordrecht, 1995.

[14] S. Fraden. Phase transitions in colloidal suspensions of virus particles. In M. Baus, L. F. Rull, and J. P. Ryckaert, editors, *Observation, Prediction, and Simulation of Phase Transitions in Complex Fluids*, pages 113–164. Kluwer Academic, Dordrecht, 1995.

[15] J. Herzfeld, A. E. Berger, and J. W. Wingate. A highly convergant algorithm for computing the orientation distribution functions of rodlike particles. *Macromolecules*, 17:1718–1723, 1984.

[16] A. Stroobants, H. N. W. Lekkerkerker, and T. Odijk. Effect of electrostatic interaction on the liquid crystal phase transition in solutions of rodlike polyelectrolytes. *Macromolecules*, 19:2232, 1986.

[17] J. R. Philip and R. A. Wooding. Solution of the poisson-boltzmann equation about a cylindrical particle. *J. Chem. Phys.*, 52:953, 1970.

[18] A. Grosberg and A. Khokhlov. *Giant Molecules: Here, There and Everywhere.* Academic Press, New York, 1997.

[19] A. R. Khokhlov and A. N. Semenov. Liquid-crystalline ordering in the solution of partially flexible macromolecules. *Physica A*, 112:605, 1982.

[20] R. Hentschke. Equation of state for persisteny-flexible liquid crystal polymers. comparison wiht poly(γ-benzyl-l-glutamate) in dimethylformamide. *Macromolecules*, 23:1192–1196, 1990.

[21] T. Odijk. Theory of lyotropic polymer liquid crystals. *Macromolecules*, 19:2313, 1986.

[22] D. P. DuPre and S. Yang. Liquid crystaline properties of solutions of persistent polymer chains. *J. Chem. Phys.*, 94:7466–7477, 1991.

[23] Z. Y. Chen. Nematic ordering in semiflexible polymer chains. *Macromolecules*, 26:3419, 1993.

[24] E. M. Kramer and J. Herzfeld. Distribution function for reversibly self-assembling spherocylinders. *Phys. Rev. E*, 58:5934–5947, 1998.

[25] P. G. Bolhuis and D. Frenkel. Tracing the phase boundaries of hard spherocylinders. *J. Chem. Phys.*, 106:668–687, 1997.

[26] J. P. Straley. Third virial coefficient for the gas of long rods. *Mol. Cryst. Liq. Cryst.*, 24:7, 1973.

[27] M. A. Cotter. Hard particle theories of nematics. In G. R. Luckhurst and G. W. Gray, editors, *The Molecular Physics of Liquid Crystals*, pages 169–189. Academic Press, London, 1979.

[28] Z. Dogic, K. Purdy, E. Grelet, M. Adams, and S. Fraden. Isotropic- cholesteric transitions in suspensions of filamentous virus and the neutral polymer dextran. *Phys. Rev. E*, 69:051702, 2004.

[29] Z. Dogic. *Liquid crystalline phase transitions in virus and virus/polymer suspensions.* PhD thesis, Brandeis University, 2000.

[30] J. Tang and S. Fraden. Isotropic-cholesteric phase transition in colloidal suspensions of filamentous bacteriophage fd. *Liquid Crystals*, 19:459–467, 1995.

[31] E. M. Kramer and J. Herzfeld. Avoidance model for soft particles. I. Charged spheres and rods beyond the dilute limit. *J. Chem. Phys.*, 110:8825–8834, 1999.

[32] E. M. Kramer and J. Herzfeld. Avoidance model for soft particles. II. Positional ordering of charged rods. *Phys. Rev. E*, 61:6872–6878, 2000.

[33] D. A. Marvin, R. D. Hale, C. Nave, and M. Helmer Citterich. Molecular models and structural comparisons of native and mutant class I filamentous bacteriophages Ff(fd, f1, M13),If1 and IKe. *J. Molec. Bio.*, 235:260–286, 1994.

[34] K. Zimmermann, J. Hagedorn, C. C. Heuck, M. Hinrichsen, and J. Ludwig. The ionic properties of the filamentous bacteriophages Pf1 and fd. *J. Biol. Chem.*, 261:1653, 1986.

[35] Z. Dogic and S. Fraden. The smectic phase in a colloidal suspension of semiflexible virus particle. *Phys. Rev. Lett.*, 78:2417, 1997.

[36] J. Sambrook, E. F. Fritsch, and T. Maniatis. Single-stranded, filamentous bacteriophage vectors. In *Molecular Cloning: A Laboratory Manual*, chapter 4. Cold Spring Harbor Laboratory, New York, second edition, 1989.

[37] Z. Dogic and S. Fraden. Phase behavior of rod-like virus and virus/polymer mixture. *Phil. Trans. R. Soc. Lond. A.*, 359:997–1015, 2001.

[38] E. Grelet and S. Fraden. What is the origin of chirality in the cholesteric phase of virus suspensions? *Phys. Rev. Lett*, 90:198302, 2003.

[39] P. G. de Gennes and J. Prost. *The Physics of Liquid Crystals.* Oxford Science, second edition, 1993.

[40] T. Sato and A. Teramoto. Concentrated solutions of liquid-crystalline polymers. *Adv. in Poly. Sci.*, 126:85–161, 1996.

[41] R. F. Kayser, Jr. and H. J. Raveche. Bifurcation in onsager's model of the isotropic-nematic transition. *Phys. Rev. A*, 17:2067, 1978.

[42] K. R. Purdy, Z. Dogic, S. Fraden, A. Rühm, L. Lurio, and S. G. J. Mochrie. Measuring the nematic order of colloidal fd virus by x-ray diffraction. *Phys. Rev. E*, 67:031708, 2003.

[43] J. Lapointe and D. A. Marvin. Filamentous bacterial viruses. VIII. liquid crystals of fd. *Mol. Cryst. Liq. Cryst.*, 19:269, 1973.

[44] K. R. Purdy and S. Fraden. The influence of charge and flexibility on smectic phase formation in rod suspensions. unpublished, 2004.

[45] M. J. Glucksman, S. Bhattacharjee, and L. Makowski. Three-dimensional structure of a cloning vector. *J. Mol. Biol.*, 226:455–470, 1992.

[46] T. Sato and A. Teramoto. Statistical mechanical theory for liquid-crystaline polymer solutions. *Acta. Polymer.*, 45:399–412, 1994.

[47] J. Th. G. Overbeek. Quantitative interpretation of the clevtrophoretic velocity of colloids. In H. Mark and E. J. W. Verwey, editors, *Advances in Colloid Science*, pages 97–135. Interscience Publishers, New York, 1950.

[48] R. Oldenbourg and W. C. Phillips. Small permanent magnet for fields up to 2.6 T. *Rev. Sci. Instrum.*, 57:2362–2365, 1986.

[49] J. Torbet and G. Maret. High-field magnetic birefringence study of the structure of rodlike phages pf1 and fd in solution. *Biopolymers*, 20:2657, 1981.

[50] J. Tang and S. Fraden. Magnetic field induced isotropic-nematic phase transition in a colloidal suspension. *Phys. Rev. Lett.*, 71:3509, 1993.

[51] T. Odijk and A. C. Houwaart. On the theory of the excluded-volume effect of a polyelectrolyte in a 1-1 electryolyte solution. *J. Poly. Sci. Poly. Phys. Ed.*, 16:627–639, 1978.

[52] J. M. Polson. First-order nematic-smectic phase transtion for hard spherocylinders in the limit of infinite aspect ratio. *Phys. Rev. E*, 56:R6260, 1997.

[53] R. B. Meyer. Ordered phases in colloidal suspensions of Tobacco Mosaic Virus. In A. Onuki and K. Kawasaki, editors, *Dynamics and Patterns in Complex Fluids*, page 62. Springer-Verlag, 1990.

[54] H. Maeda and Y. Maeda. Liquid crystal formation in suspensions of hard rodlike colloidal particles: Direct observation of particle arrangement and self-ordering behavior. *Phys. Rev. Lett.*, 90:018303, 2003.

[55] A. V. Tkachenko. Nematic-smectic transition of semiflexible chains. *Phys. Rev. Lett.*, 77:4218–4221, 1996.

[56] K. R. Purdy and S. Fraden. Charge and flexibility dependence of the isotropic-cholesteric phase transition of colloidal rods. cond-mat/0406145, 2004.

[57] A. Stroobants, H. N. W. Lekkerkerker, and D. Frenkel. Evidence for smectic order in a fluid of hard parallel spherocylinders. *Phys. Rev. Lett.*, 57:1452, 1986.

[58] G. S. Manning. *J. Chem. Phys.*, 51:924, 1969.

[59] M. A. Cotter and D. C. Wacker. Van der waals theory of nematogenic solutions. i. derivation of the general equations. *Phys. Rev. A*, 18:2669, 1978.

[60] P. van der Schoot. The nematic-smectic transition in suspensions of slightly flexible hard rods. *J. Phys. II France*, 6:1557, 1996.

[61] M. L. Henle, C. D. Santangelo, D. M. Patel, and P. A. Pincus. Distribution of counterions near discretely charged planes and rods. *Europhys. Lett.*, 66:284, 2004.

[62] H. H. Strey, V. A. Parsegian, and R. Podgornik. Equation of state for DNA liquid crystals: Fluctuation enhanced electrostatic double layer repulsion. *Phys. Rev. Lett.*, 78:895, 1997.

[63] A. B. Harris, R. D. Kamien, and T. C. Lubensky. Molecular chirality and chiral parameters. *Rev. Mod. Phys.*, 71:1745, 1999.

[64] F. Bawden, C., N. W. Pirie, J. D. Bernal, and I. Fankuchen. Liquid crystalline substances from virus infected plants. *Nature*, 138:1051, 1936.

[65] Z. Dogic and S. Fraden. Cholesteric phase in virus suspensions. *Langmuir*, 16:7820–7824, 2000.

[66] L. A. Day, C. J. Marzec, S. A. Reisberg, and A. Casadevall. DNA packing in filamentous bacteriophages. *Ann. Rev. Biophys. Chem.*, 17:509, 1988.

[67] A. Casadevall and L. A. Day. DNA packing in the filamentous viruses fd, Xf, Pf1, and Pf3. *Nucleic Acids Research*, 10(7):2467–2480.

[68] A. Casadevall and L. A. Day. Silver and mercury probing of deoxyribonucleic acid structures in the filamentous viruses fd, If1, Ike, Xf, Pf1, and Pf3. *Biochemistry*, 22:4831–4842.

[69] A.A. Kornyshev, S. Leikin, and S.V. Malinin. *Eur. Phys. J. E*, 7:83, 2002.

[70] A. B. Harris R. D. Kamien and T. C. Lubensky. Microscopic origin of cholesteric pitch. *Phys. Rev. Lett.*, 78:1476, 1997.

[71] D. E. Bradley, J. N. Coetzee, T. Bothma, and R. W. Hedges. Phage X: A plasimid dependent, broad host range, filamentous bacterial virus. 126:389–396, 1981.

[72] J. A. Diverdi and S. J. Opella. Phosphorus-31 nuclear magnetic resonance of fd virus. *Biochemistry*, 20:280–284, 1981.

[73] A. Plückthun, website: http://www.biochem.unizh.ch/plueckthun/teaching/Teaching_slide_shows/filamentous_phages/index.htm.

[74] G. Hunter, D. Rowitch, and R. Perham. Interactions between DNA and coat protien in the structure and assemly of filamentous bacteriophage fd. *Nature*, 327:252, 1987.

[75] Lauren Day in private communication.

[76] S. Bhattacharjee, M. J. Glucksman, and L. Makowski. Structural polymorphism correlated to surface charge in fliamentous bacteriophages. *Biophys. J.*, 61:725–735, 1992.

[77] T. Odijk. Pitch of a polymer cholesteric. *J. Phys. Chem.*, 91:6060–6062, 1987.

[78] R. A. Pelcovits. Cholesteric pitch of rigid and semiflexible chiral liquid crystals. *Liq.Cryst.*, 21:361, 1996.

[79] G. Lasher. *J. Chem. Phys.*, 53:4141, 1970.

[80] S. D. Lee and R. B. Meyer. Computations of the phase equilibrium, elastic constants, and viscosities of a hard-rod nematic liquid crystal. *J. Chem. Phys.*, 84:3443, 1986.

[81] R. Oldenbourg, X. Wen, R. B. Meyer, and D. L. D. Caspar. Orientational distribution function in nematic tobacco mosaic virus liquid crystals measured by X-ray diffraction. *Phys. Rev. Lett.*, 61:1851–1854, 1988.

[82] L. C. A. Groot, M. E. Kuil, J. C. Leyte, and J. R. C. van der Maarel. Neutron scattering experiments on magnetically aligned liquid crystalline DNA fragment solutions. *Liquid Crystals*, 17:263–276, 1994.

[83] K. Kassapidou, R. K Heenan, W. Jesse, M. E. Kuil, and J. R. C. van der Maarel. Effects of ionic strength on the supramolecular structure in liquid crystalline solutions of persistent length DNA fragments. *Macromolecules*, 28:3230–3239, 1995.

[84] P. Davidson, C. Bourgaux, P. Sergot, and L. Livage. A small-angle x-ray scattering study of the lyotropic nematic phase of vanadium pentoxide gels. *J. Appl. Cryst.*, 30:727–732, 1997.

[85] A. Peterlin and H. A. Stuart. *Zeitschrift für Physik*, 112:1, 1939.

[86] X. Ao, X. Wen, and R. B. Meyer. X-ray scattering from plymer nematic liquid crystals. *Physica A*, 176:63–71, 1991.

[87] P. van der Schoot and T. Odijk. Static and dynamic light scattering from liquid crystalline solutions of rodlike macromolecules. *J. Chem. Phys.*, 93:3580, 1990.

[88] P. van der Schoot. Self-assembly of globular particles in a nematic dispersion of colloidal rods. *J. Chem. Phys.*, 117:3537, 2002.

[89] L. Makowski and D. L. D. Caspar. The symmetries of filamentous phage particles. *J. Mol. Bio.*, 145:611–617, 1981.

[90] Layer line data from M13 at PH 2 provided by L. Makowski in private communication.

[91] E. E. Maier, R. Krause, M. Deggelmann, M. Hagenbuchle, R. Weber, and S. Fraden. Liquidlike order of charged rodlike particle solutions. *Macromolecules*, 25:1125–1133, 1992.

[92] A.J. Leadbetter and E.K. Norris. Distribution functions in three liquid crystals from x-ray diffraction measurements. *Mol. Phys.*, 38:669–686, 1979.

[93] P. Davidson, D. Petermann, and A. M. Levelut. The measurement of the nematic order parameter by X-ray scattering reconsidered. *J. Phys II*, 5:113, 1995.

[94] K. C. Holmes and J. Barrington Leigh. The effect of disorientation on the intensity distribution of non-crystalline fibres. I. Theory. *Acta Cryst.*, A 30:635, 1974.

[95] A. Guinier. *X-ray Diffraction in Crystals, Imperfect Crystals, and Amorphous Bodies.* Dover Publications, New York, 1994.

[96] K. C. Holmes and D. M. Blow. *The Use of X-ray Diffraction in the Study of Protein and Nucleic Acid Structure.* Interscience Publishers, 1966.

[97] M. Deutsch. Orientational order determination in liquid crystals by X-ray diffraction. *Phys. Rev. A*, 44:8264–8270, 1991.

[98] D. Schneider and D. L. D. Caspar, 1980. (unpublished).

[99] F. Jurnak and A. McPherson. *Biological Macromolecules and Assemblies.* Wiley, New York, 1984.

[100] R. Asgari, B. Davoudi, and B. Tanatar. *Phys. Rev. E*, 64, 2001.

[101] J. Rino and N. Studart. Static structure factor of hard-sphere yukawa systems. *Mod. Phys. Lett. B*, 10:1507–1515, 1996.

[102] I. W. Hamley. Scattering from uniform, cylindrically symmetric particles in liquid crystal phases. *J. Chem. Phys.*, 95:9376, 1991.

[103] X. Ao. Length distribution of TMV by signal-averaging transient electric birefringence. unpublished.

[104] P.C.Hemmer. Phase transitions in a solution of rodlike macromolecules of two different sizes. *Molecular Physics*, 96(8):1153–1157, 1999.

[105] S. Varga, A. Galindo, and G. Jackson. New types of phase behaviour in binary mixtures of hard rod-like particles. *Molecular Physics*, 101:817–825, 2003.

[106] H. N. W. Lekkerkerker, P. Buining, J. Buitenhuis, G. J. Vroege, and A. Stroobants. Liquid crystal phase transitions in dispersions of rodlike colloidal particles. In M. Baus, L. F. Rull, and J. P. Ryckaert, editors, *Observation, Prediction and Simulation of Phase Transitions in Complex Fluids*, pages 53–112. Kluwer Academic, Dordrecht, 1995.

[107] T. Itou and A. Teramoto. Multi-phase equilibrium in aqueous solutions of the triple-helical polysaccharide, schizophyllan. *Polymer Journal*, 16(10):779–790, 1984.

[108] K. Kajiwara, N. Donkai, Y. Hiragi, and H. Inagaki. *Makromol. Chem.*, 187, 1986.

[109] R. van Roij and B. Mulder. Absence of a high-density consulute point in nematic hard rod mixtures. *J. Chem. Phys.*, 105(24):11237, 1996.

[110] S. Varga and I. Szalai. Phase diagrams of binary mixture of hard rods in an external orientational field. *Phys. Chem. Chem. Phys.*, 2:1955, 2000.

[111] H. N. W. Lekkerkerker and A. Stroobants. Phase behavior of rod-like colloid plus flexible polymer mixtures. *Nuovo Cimento D*, 16:949–962, 1994.

[112] G. J. Vroege and H. N. W. Lekkerkerker. Phase transitions in lyotropic colloidal and polymer liquid crystals. *Rep. Prog. Phys.*, 55:1241, 1992.

[113] J. D. Parsons. Nematic ordering in a system of rods. *Phys. Rev. A*, 19:1225, 1979.

[114] S. Lee. A numerical investigation of nematic ordering based on a simple hard-rod model. *J. Chem. Phys.*, 87:4972, 1987.

[115] S. Varga, A. Galindo, and G. Jackson. Global fluid phase behavior in binary mixtures of rodlike and platelike molecules. *J. Chem. Phys.*, 117:7207, 2002.

[116] J. Sambrook, E. F. Fritsch, and T. Maniatis. *Molecular Cloning: A Laboratory Manual.* Cold Spring Harbor Laboratory, New York, second edition, 1989.

[117] V. A. Baulin and A. R. Khokhlov. Nematic ordering of rigid rods in a graviational field. *Phys. Rev. E*, 60:2973, 1999.

[118] R. van Roij and B. Mulder. Demixing versus ordering in hard-rod mixtures. *Phys. Rev. E*, 54(6):6430, 1996.

[119] H. Fynewever and A. Yethiraj. Phase behavior of semiflexible tangent hard sphere chains. 108:1637, 1998.

[120] Z. Dogic, D. Frenkel, and S. Fraden. Enhanced stability of the layered phases in parallel spherocylinders due to addition of hard spheres. *Phys. Rev. E*, 62:3925–3934, 2000.

[121] M. Reenders and G. ten Brinke. Compositional and orientational orering in rod-coil diblock copolymer melts. *Macromolecules*, 35:3266–3280, 2002.

[122] R. P. Sear and G. Jackson. Stability of the nematic phase of a mixture of aligned cylinders with respect to the smectic and columnar phases. *J. Chem. Phys.*, 102:2622, 1995.

[123] T. Koda, M. Numajiri, and S. Ikeda. Smectic-A phase of bidisperse system of parallel rods and hard spheres. *J. Phys. Soc. Jpn.*, 65:3551, 1996.

[124] T. Koda and H. Kimura. Phase diagram of the nematic-smectic A transition of the binary mixture of parallel hard cylinders of different lengths. *J. Phys. Soc. Jpn.*, 63:984, 1994.

[125] K. Devanand and J. C. Selser. Asymptotic behavior and long-range interactions in aqueous solutions of poly(ethylene oxide). *Macromolecules*, 24:5943, 1991.

[126] A. N. Semenov. Smectic ordering in block-copolymer melts. *Mol. Cryst. Liq. Cryst*, 209:191–199, 1991.

[127] A. Halperin. Roc-coil copolymers: Their aggregation behavior. *Macromolecules*, 23:2724–2731, 1990.

[128] M. W. Matsen and C. Barett. Liquid-crystalline behavior of rod-coil diblock copolymers. *J. Chem. Phys.*, 109:4108, 1998.

[129] M. Mazars, D Levesque, and j. J. Weis. Monte carlo study of a semiflexible liquid crystal model: the smectic phase. *J. Chem. Phys.*, 106:6107, 1997.

[130] Z. Zhang, M. A. Horsch, M. H. Lamm, and S. C. Glotzer. Tethered nano building blocks: Toward a conceptual framework for nanoparticle self-assembly. *Nano Letters*, 3:1341–1346, 2003.